Research Trends in Mechanical Engineering 2016

Conference Proceedings

First International Conference and Workshop on

Mechanical Engineering Research

11-13 July 2016

universidade de aveiro
theoria poiesis praxis

“The essence of life is to assure its continuity. The timelessness of being is the mainstay of the existence. The bona fide test of a life is to dig the tunnel of the existence in continuity. This is why the Research Trends in Mechanical Engineering Conference is in memory of Professor José Joaquim de Almeida Grácio. He crossed this trial watering a field of roses with torrents of smiles that overflowed into fruitful scientific research initiatives, technological innovations and lasting emotional bonds with younger generations in academic and humanitarian frameworks. As a sterling producer, seeds germinated in his hands, becoming friendly networks that crossed universities, enterprises and other governmental and nongovernmental organizations. When transforming grain defects in metal alloys into useful properties, the youth memories of meadowlands contemplation and of the surprise facing the transforming power of the blast furnace returned to his face. The wind silence and the crackling fire streamed from the blood to the guitar strings with the force of the river Tagus that witnessed his birth. The Tagus’s strength and the strength of materials were imprinted in his character. The cross-border Tagus with alluvium soils flows into the ocean and the stress-strain curves of ductile life deviate into a rewarding circle of friends and colleagues around manifold activities of Research and Technological Development. The Conference Book of the International Conference and Workshop on Mechanical Research in memory of Professor José Joaquim de Almeida Grácio compiles valuable scientific contributes of those who crossed with José underlined Aveiro in the map of their scientific and personal lives.”

Paula Gonçalves

Research Trends in Mechanical Engineering 2016

Conference Proceedings

First International Conference and Workshop on

Mechanical Engineering Research

11-13 July 2016

Title
Research Trends in Mechanical Engineering 2016 - Conference Proceedings

Editors
A. B. Pereira, A. C. M. Sousa, F. Barlat, G. Vincze

Committees:

Design
G. Vincze

Publisher
UA Editora
Universidade de Aveiro

1st edition – July 2016

ISBN
978-972-789-483-3

Conference Proceedings

Research Trends in Mechanical Engineering (RTME)

First International Conference and Workshop on Mechanical Engineering Research

In memory of Professor José Joaquim de Almeida Grácio

Table of Contents

Preface

Professor José Joaquim de Almeida Grácio was a man of many talents. His contribution to the development of physical models to predict the mechanical behaviour of materials for long-term applications in the areas of nanotechnology and forming processes was outstanding and of major international significance. He was a leader not only in his research but also at university administration level. Soon after he received his Ph.D. from the University of Coimbra (Portugal) in 1992, he joined the University of Aveiro with the mission of creating the Department of Mechanical Engineering (DEM). He headed DEM for more than a dozen years and today DEM is one of the top departments of mechanical engineering in Portugal. This fact fully attests Professor José Grácio's singular commitment, vision, energy and intelligence. He also established the R&D Unit Centre for Mechanical Technology and Automation (TEMA); during his tenure as scientific coordinator, TEMA received twice, after research assessment exercises at the end of four-year periods, the highest classification (Excellent). His activity kept him at a constant gruelling pace – finding him at DEM well past midnight was a nearly normal event. He maintained an intense schedule of national and international collaborations but, thanks to his prodigious memory, he used to take only a few notes to keep the schedule on track. His effort was recognized by many sectors, just to name a few, in 2000 he received from the Municipality of the City of Abrantes the Honourable Award for Science and Technology, in 2002 he was the winner of the Bunshah Prize award for the best paper presented at the ICMCTF 2002, in 2004 he was the winner of APDF Prize award for the project Multiscale Approach of Materials for Automotive and Aircraft Industries, in 2005 with a paper published in IJP he was awarded with the SigmaXI Prize, in 2006 the team that he led was finalist of Nanochallenge2006 with the project NanotecSolutions, and in January 2007 he received the award for high level professional research on plastic deformation and fracture mechanics from the Alcoa Technical Centre, USA. Beyond these extraordinary accomplishments, Professor José Grácio should be also remembered for his extraordinary generosity to his students and colleagues. His mentoring had no bounds or hours, his availability became legendary in his own lifetime. He remains an amazing source of inspiration for all those that had the privilege of knowing him.

Research Trends in Mechanical Engineering (RTME) - First International Conference and Workshop on Mechanical Engineering Research was organized aiming to pay homage to that exceptional man that Professor José Grácio was. The scope of the conference is focussed on the science and practice of mechanical engineering very much in line with the example provided by Professor José Grácio's academic and professional activity.

This Proceedings booklet, which collects the papers accepted for presentation at RTME, reflects the multidisciplinary of the themes covered.

We are pleased to have a distinguished group of authors, We use this opportunity to thank the keynote speakers, Professors Said Ahzi, Paulo A. F. Martins, Catalin Picu, Edgar Rauch and Jean-Hubert Schmitt, and all the participants, who have come from many parts of the world, for sharing their research experience.

Aveiro, 4th of July, 2016

The Organizing Committee

Frédéric G. Barlat

António M.B. Pereira

António C.M. Sousa

Gabriela Vincze

Organizing Committee

Chairperson

Barlat, F.
Pereira, A.M.B.
Sousa, A.C.M.
Vincze, G.

Honorary Committee

Ahzi, S.	France
Cesar de Sá, J.	Portugal
Gonçalves, M.P.P.	Portugal
LeDuc, Philip	USA
Martins, P.A.F.	Portugal
Menezes, L.F.	Portugal
Picu, C.R.	USA
Rauch, E.F.	France
Schmitt, Jean-Hubert	France
Tome, C.N.	USA
Yoon, J.W.	Australia

Local Organizing Committee

Butuc, M.C.
Lopes, A.
Marques, P.A.A.M.
Neto, V.F.S.
Pereira, A.M.B.
Vincze, G. (Chair)

Scientific Committee

Ahzi, S.	France	Menezes, L.F.	Portugal
Andrade-Campos, G.	Portugal	Neto da Silva, F.J.	Portugal
Banabic, D.	Romania	Neto, V.F.S.	Portugal
Barlat, F.	South Korea	Oliveira, M.C.	Portugal
Butuc, M.C.	Portugal	Pereira, A.M.B.	Portugal
Cabral, G.	Portugal	Picu, R.C.	USA
Cardoso, R.P.R.	UK	Ramos, A.	Portugal
Cesar de SA, J.	Portugal	Rauch, E.F.	France
Coelho, M.C.	Portugal	Santos, A.	Portugal
Completo, A.M.G.	Portugal	Schmitt, J.-H.	France
LeDuc, Philip	USA	Simões, F.	Portugal
Lee, M.G.	South Korea	Tome, C.N.	USA
Lopes, A.B.	Portugal	Valente, R.A.F.	Portugal
Marques, P.	Portugal	Vincze, G.	Portugal
Martins, P.A.F.	Portugal	Yoon, J.W.	Australia

Mini-symposia organizers

MS1: Formability of metallic materials - Carmen Butuc and Dorel Banabic

MS2: Microestructure and properties of materials – Augusto Lopes and Edgar Rauch

MS3: Multiscale and Constitutive modelling – Marta Oliveira and Luis Alves

MS4: Sheet Metal Forming Processes - Ricardo Sousa and Fábio Simões

MS5: Computational Mechanics – Gil Campos and Robertt Valente

MS6: Nanoengineering – Paula Marques, Duncan Fagg, Aliaksandr Shaula, Igor Bdkin, Manoj Singh

MS7: Challenges in Intelligent Transportation Systems – Margarida Coelho

MS8: Energias – Fernando Neto

MS9: Biomechanics – António Completo

MS10: Experimental techniques in structural mechanics – Francisco Queirós de Melo

Plenary sessions

ON THE MICROMECHANICAL MODELIN OF THE THERMOMECHANICAL BEHAVIOR OF POLYMERS AND POLYMER COMPOSITE/NANOCOMPOSITES

Saïd Ahzi*

Qatar Environment & Energy Research Institute - QEERI, Hamad Bin Khalifa University, Qatar Foundation, PO Box 5825, Doha, Qatar

ABSTRACT: In this presentation, we will address some of the new developments in the micromechanical modeling of the thermomechanical behavior of polymers and polymer composites as well as the effects of recycling of these materials. Different polymer matrices, unfilled or filled with different micro-fillers ornano-fillers, are considered. For this, we developed an approach that is valid for a wide range of loading rates, from quasi-static to dynamic loadings, as well as for a wide range of temperatures, from well below to above the glass transition

In a first part, we will address the thermomechanical behavior of recycled Polypropylene (PP) filled with ethylene octene copolymer (EOC) and talc. Because PP-based composites are usually used in the manufacturing of bumpers where high loading rates and wide range of temperatures are involved, a detailed study of high strain rate and temperature sensitivities of recycled PP-based composites is achieved. The dynamical properties are correlated with the morphology of the studied composites by using microscopy. The micromechanical modeling is used to predict the yield and the elastic behaviors of non-recycled and recycled materials with temperature and strain rate dependencies.

In the second part of this presentation, we will address the micromechanical modeling of polymer nanocomposites where microstructural and interfacial effects are accounted for. For the semi-crystalline matrices and for the composites, different homogenization techniques are used to compute the effective elastic and yield properties. In this, microstructural and interfacial effects are accounted for. These techniques are also used, as inverse methods, to predict the microstructure for a given macroscopic response. Our predicted results are compared to our experimentally measured ones.

References

1- K. Wang, F. Addiego, N. Bahlouli, S. Ahzi, Y. Rémond, V. Toniazzo. “Impact response of recycled polypropylene-based composites under a wide range of temperature: Effect of filler content and recycling”. Composites Science and Technology 95, 89-99, 2014

2- K. Wang, N. Bahlouli, F. Addiego, S. Ahzi, Y. Rémond, D. Ruch, R. Muller; “Effect of talc content on the degradation of re-extruded polypropylene/talc composites»; Polymer Degradation and Stability, Vol. 98, pp. 1275-1286, 2013.

3- K. Wang, Ahzi, R. MatadiBoumbimba, N. Bahlouli, F. Addiego, Y. Rémond; “Micromechanical modeling of elastic behavior of a polypropylene based organoclay nanocomposites under a wide range of temperatures and strain rates/frequencies”; Mechanics of Materials, Vol 64,56-68, 2013.

4- Wang K., MatadiBoumbimba R.M, Bahlouli N, Ahzi S., Muller R., Bouquey M “Dynamic compressive behavior of a melt mixed Polypropylene/organoclay nanocomposites ” Journal of Engineering Material and Technology, January 2012, Vol 134, Issue 1, pp. 010905-1/11

5- R. Matadi-Boumbimba, S. Ahzi, N. Bahloui, D. Ruch and and J. Gracio, “Dynamic Mechanical Properties of PMMA/Organoclay Nanocomposite: Experiments and Modeling”; Journal of Engineering Materials and Technology, 2011, Vol. 133, No. 3, 030908-1-030908-6

6- R. Matadi, O. Gueguen, S. Ahzi, J. Gracio, R. Muller, D. Ruch, “Investigation of the stiffness and yield behaviour of melt-intercalated Poly (methyl methacrylate)/organoclay nanocomposites: characterisation and modelling” Journal of Nanoscience and Nanotechnology , , Vol. 10, Issue 4, pages 2956–2961 (2010)

* Corresponding author: sahzi@qf.org.qa

MECHANICAL CHARACTERIZATION OF MATERIALS FORSHEET-BULK METAL FORMING PROCESSES

P. Sieczkarek[1], Silva C.M.A[2],S. Wernicke[1], A.E. Tekkaya[1]and P.A.F. Martins[2*]

[1]Affiliation (author1) Institute of Forming Technology and Lightweight Construction, TU Dortmund University, BaroperStr. 303, D-44227 Dortmund, Germany

[2]IDMEC, Instituto Superior Técnico, Universidade de Lisboa, Av. RoviscoPais, 1049-001 Lisboa, Portugal

ABSTRACT: This paper presents a new experimental methodology for determining the stress-strain curve, the fracture toughness and the critical instability strength of plates and sheets to be used in sheet-bulk metal forming (SBMF) applications. The stress-strain curve and fracture toughness are obtained from double-notched test specimens loaded in shear and the material flow behaviour is compared against that obtained from conventional tensile tests. The critical instability strengthis obtained from rectangular test specimens loaded in compression by means of a combined experimental and theoretical procedure that makes use of the analytical solution for the elasto-plastic stability of plates subjected to equal uniform compression on two opposite edges. The work is performed in aluminium EN AW 1050 and steel DC04 sheets with 3 mm thickness and the proposed experimental methodology proves adequate to the mechanical characterization of materials under the high levels of strain that are commonly found in SBMF processes.

Keywords: Sheet-bulk metal forming, Stress-strain curve, Fracture toughness, Critical instability strength

[*]Corresponding author: Fax: +351-21-8419058, E-mail: pmartins@ist.utl.pt

PHYSICAL BASIS OF STRAIN RATE SENSITIVITY IN METALLIC SOLID SOLUTION ALLOYS

R.C. Picu*

Department of Mechanical, Aerospace and Nuclear Engineering
Rensselaer Polytechnic Institute, Troy, NY 12180, USA

ABSTRACT: Plastic deformation of metallic alloys is described on continuum scales by constitutive laws that depend, at a minimum, on strain, strain rate and temperature. The dependence on the last two parameters emerges from an essential feature of plastic deformation which is the fact that the evolution of dislocation structures under stress is thermally activated. In solid solutions, the interaction of dislocations and solute atoms produces additional effects that influence both the flow stress and the strain rate sensitivity. Solute may have low or high mobility and may form transient clusters that evolve with the plastic strain. The importance of a proper understanding of these physical phenomena as well as the need to account for them when developing constitutive equations for plasticity emerge from the observation that the stability of plastic deformation and hence formability are controlled by the strain hardening rate and the strain rate sensitivity of the material.

In this talk I will review several mechanisms controlling the instantaneous and transient components of the strain rate sensitivity in metallic alloys with mobile solute (e.g. Al alloys of the 5000 class) and with precipitates (e.g. Al alloys of the 6000 class). Special attention will be devoted to solute clusters as they play an important role in rendering negative the strain rate sensitivity of alloys with mobile solute and no precipitates. Ways to capture these mechanisms in constitutive equations will be outlined. The effectiveness of using severe plastic deformation to increase the strain rate sensitivity of sheet metal for improved formability will be discussed in closure.

*Corresponding author: picuc@rpi.edu

INTRAGRANULAR STRUCTURE EVOLUTION AND MECHANICAL BEHAVIOR OF METALS IN COLD FORMING

E.F. RAUCH*

University Grenoble Alpes, CNRS, SIMAP, F-38000 Grenoble, France

ABSTRACT: The formability of materials being intimately related to the physical processes involved during their deformation, it is essential to understand and describe properly these basic mechanisms if it is attempted to optimize the forming conditions. In particular, when numerical simulations are used to predict the mechanical behavior of the worked piece, only physically based flow laws are inherently able to extend the predictions beyond the range of thermo-mechanical parameters used to characterize the material.

For metals and alloys, cold work mainly involves dislocation movements that lead to lattice rotations and to strong interactions with obstacles. Therefore, not only the textural but also the structural evolutions must be considered to retrieve stress levels, strain hardening and flow localization. Apart from the Taylor factor and the dislocation density, refined features like the substructure size, the dislocation pattern shape and cell misorientations are frequently involved in the plastic flow laws to account for the mechanical properties. The abilities of the resulting constitutive equations to replicate reality is balanced by their time consuming complexities. With such limitation in mind, it appears essential to ascertain through dedicated structural characterization, mainly TEM observations, that the selected features are meaningful.

To probe the importance of structural features, complex loading conditions, that are frequent in forming processes like deep drawing, are importance source of information. They constitute natural validation tests for theoretical formulations of the mechanical behavior. In particular the transient hardening related to an abrupt change of strain path is a direct signal related to re-adaptation of the intragranularcell structure.

Besides, crystallographic rotations increases with strains and eventually transforms cells in grains. These rotation may now be inferred with a dedicated TEM tool that automatically analyses the electron diffraction patterns.

In this presentation, it is proposed to review these structural observations and their mechanical counterparts for largely deformed steels.

*Corresponding author: edgar.rauch@simap.grenoble-inp.fr

PLASTIC BEHAVIOR AND FRACTURE OF HEAVILY DRAWN PEARLITIC WIRES

Jean-Hubert Schmitt*

CentraleSupélec

ABSTRACT: Pearlitic wires are heavily drawn to increase their mechanical resistance. It induces an important crystalline and morphological anisotropy. This strongly influences the material behavior during subsequent loadings. Usually subsequent mechanical properties of drawn wires are studied by tension differing not so much from drawing. The maximum tensile stress increases with the amount of prestrain, and it results mainly from the internal stresses after wiring. Complementarily, torsion tests after drawing show that specific damage mechanisms develop linked to the microstructure morphological texture.

In a first step, the microstructure and mechanical state are studied and quantified after drawing. SEM and TEM observations are performed in the wire section and along the drawing axis. Crystallographic textures are measured by XRD at the wire surface and at different radius to investigate their evolutions through the wire section. In a similar way, internal stresses are also evaluated by X-ray diffraction. These results are used to validate the Finite Element calculations which allow estimating the stress and strain states within the wire section after drawing.

Sequential stress loadings are then applied to drawn wires. They are mainly combinations of torsion and tension after high drawing reductions. Critical crack length leading to delamination fracture is experimentally determined. The respective role of internal stresses, crystallographic orientation, and crack propagation on the wire fracture are deduced from experiments and numerical simulations.

It leads to quantitative prediction of the rupture mechanisms as a function of the drawing amount and of the mechanical behavior of the wires.

*Corresponding author: jean-hubert.schmitt@centralesupelec.fr

Formability of metallic materials

CHARACTERIZATION OF HARDENING BEHAVIOR OF METALS USING CRYSTAL / DISLOCATION PLASTICITY VIRTUAL EXPERIMENTS†

F. Barlat[1,2*], Y. Jeong[3], C. Tomé[4]

[1]Pohang University of Science and Technology, Republic of Korea
[2]University of Aveiro, Portugal
[3]Clemson University, SC, USA
[4]Los Alamos National Laboratory, NM, USA

ABSTRACT: A viscoplastic self-consistent crystal plasticity (VPSC) framework with a dislocation-based hardening model, so-called RGVB, was developed to describe the strain path-dependent flow behavior of polycrystalline aggregates. In this model, the dislocation density pertaining to each slip system is a function of the accumulated strain, slip shear reversal and interactions with other slip systems. The model can describe the typical features of a flow curve observed upon load-reversal and cross-loading such as lower yield stress, transient plateau and permanent softening/hardening after reloading. Since a direct application of this framework in metal forming simulations is a computationally expensive task, an alternative method is suggested. The VPSC-RGVB model predictions are used to characterize the yield surface evolution under a selected set of proportional and non-proportional loading path scenarios. The results of these virtual experiments can be used to fine-tune the continuum HAH distortional plasticity approach, which is more suitable for forming process simulations.

† In memory of professor José Grácio (1959-2014), without whom this work would not have been possible

*Corresponding author: GIFT/POSTECH, 77 Cheongam-ro, Nam-gu, Pohang, Gyeongbuk 37673, Republic of Korea, phone +82 54 279 9022, fax +82 54 279 9299, e-mail f.barlat@postech.ac.kr

NON-LOCAL MODELS AND PHASE FIELD METHODS IN THE DESCRIPTION OF DUCTILE FAILURE

Jose M. A. Cesar de Sa[1*], Erfan Azinpour[1], Abel D. Santos[1]

[1]INEGI, Faculty of Engineering, University of Porto, Porto, Portugal

ABSTRACT: Classical continuous descriptions of material is adequate to most of the deformation stages. However in the presence of fracture, involving crack initiation and propagation they are no longer sufficient and it is possible to adopt continuous-discontinuous approaches using different numerical techniques like element erosion, remeshing or X-FEM techniques. Some key aspects, often left unsolved in the different models, are energetic requirements to promote the necessary transition of energy release associated with material damage and fracture energy associated to a crack creation and evolution. A continuous model based on the phase-field theory is proposed to ductile failure. In classical phase field models an order parameter represents different phases within a system. The free energy is a function of the phase field variable and its gradient, similarly to non-local thermodynamical description of continuous damage mechanics. Here the phase-field variable describes the damaged zone and its evolution is associated with standard damage models.

Acknowledgement

Authors gratefully acknowledge the funding of Project NORTE-01-0145-FEDER-000022 - SciTech - Science and Technology for Competitive and Sustainable Industries, co-financed by ProgramaOperacional Regional do Norte (NORTE2020), through Fundo Europeu de Desenvolvimento Regional (FEDER)

[*]Corresponding author: INEGI, Faculty of Engineering, University of Porto, Rua Dr. Roberto Frias, s/n, 4200-465, Porto, Portugal; phone: +351 220413465; fax +351 225081445; e-mail: cesarsa@fe.up.pt

MODELLING TEXTURES AND *R*-VALUES IN ALUMINIUM ALLOYS FOR DEEP DRAWING

Paul Van Houtte[1*], Diarmuid Shore[1], Tuan Nguyen Minh[2],Leo Kestens[2], Albert Van Bael[1]
[1]Department of Materials Engineering, KULeuven, Leuven, Belgium
[2]Department of Materials Science and Engineering, Ghent University, Gent, Belgium

ABSTRACT: Aluminium sheets for deep drawing of car body parts have a poorer formability than corresponding steels sheets. This is ascribed to the typical textures developed in both materials: {111} fibre texture in steel, leading to high r-values, and a texture dominated by the {001} <100> component in aluminium, with the opposite effect. Asymmetric rolling as part of the production process is believed to be a way to obtain better r-values in the latter materials. It features a shear component which reduces the cube texture. A research project was set up to fine-tune the process parameters by modelling. Both a FEM model and a polycrystal deformation model to predict the texture (ALAMEL) are used. Part of this work will be presented here, namely the predicted textures including experimental validation, and of course, a discussion of the associated r-values.

[*] Corresponding author: Department of Materials Engineering, KULeuven, Leuven, Belgium, +32 16 321264, +32 16 321990, Paul.Vanhoutte@kuleuven.be

PREDICTION OF FORMING LIMIT DIAGRAMS USING THE PHI-MODEL AND THE MARCINIAK-KUCZYNSKI MODEL

S. Touchal-Mguil[1*], M. Mianroodi[1], G. Altmeyer[1,2], S. Ahzi[1,3]

[1]ICube laboratory, University of Strasbourg, CNRS, 2 Rue Boussingault, 67000 Strasbourg, France
[2] ECAM-Strasbourg Europe, ICube laboratory, University of Strasbourg, CNRS, 2 Rue Boussingault, 67000 Strasbourg, France
[3] Qatar Environments and Energy Research Institute, Hamad Bin Khalifa University, Qatar Foundation, PB BOX 5825, Doha, Qatar

ABSTRACT: Without taking into account the evolution of the material microstructure such as texture development during simulation of sheet metal forming processes, it is impossible to accurately predict the plastic deformation, the anisotropy and the Forming Limit Diagrams (FLD) of metals. Crystal plasticity based models are often used and are required in simulations. One of them is the viscoplastic phi-model which predicts results that span from the upper bound (Taylor model) to the lower bound (Static model) approaches [1-2].
Many localization criteria have been developed and are used for the construction of FLD [3-4]. Here, we propose the prediction of localized necking using consideration of texture development. The construction of advanced FLD will be performed by the coupling of the phi-model and the Marciniak-Kuczynski model [5]. FLD for fcc metals under many assumptions and for various values of phi, which controls the strength of the interactions in the polycrystal, are presented.

Keywords: crystal plasticity, phi-model, texture transition, localized necking, plastic instability, Forming Limit Diagram

References

[1] M'Guil, S., Ahzi, S., Barlat, F. and Gracio, J. (2011)
Simulation of microstructural effects and yield surface evolution in cubic metals using the viscoplasticphi-model. I.J.P. 27, 102-120.
[2] M'Guil, S., Wen, W., Ahzi, S. and Gracio, J. (2011)
Modeling of large plastic deformation behavior and anisotropy evolution in cold rolled bcc steels using the phi-model-based grain-interaction, MSEA. 528, 5840-5853.
[3] Altmeyer, G., Abed-Meraim, F. and Balan, T. (2008)
Comparison of forming limit diagrams predicted with different localization criteria. Steel Research International, 79, 24–31.
[4] Altmeyer, G., Abed-Meraim, F. and Balan, T. (2010)
Investigation of some localization criteria and their relevance to the prediction of forming limit diagrams. Proceedings of 13th International Conference on Metal Forming.
[5] Marciniak, Z. and Kuczyński, K. (1967)
Limit Strains in the Processes of Stretch-Forming Sheet Metal. International Journal of Mechanical Sciences, 9(9), 613-620.

* Corresponding author: ICube laboratory, University of Strasbourg, CNRS, 2 Rue Boussingault, 67000 Strasbourg, France, touchal@unistra.fr

REGULARIZED FACETED YIELD SURFACES

Bjørn Holmedal[1*]

[1]Norwegian University of Science and Technology (NTNU)

ABSTRACT: Faceted yield-surface formulations exist, both for poly-crystal and single-crystal metal plasticity descriptions. Their corners introduce mathematical singularities that can be avoided by regularizations, i.e. by rounding the corners in the five-dimensional stress space. However, higher dimensional corners are very sharp. It is discussed how different regularizations can make a significant difference in the magnitude of the stress tensor as compared to the corner or facet of the faceted surface. It is shown how the regularization has a similar effect as including strain-rate sensitivity of single crystals and a rate dependent formulation is proposed. The application of regularized faceted surfaces as approximations of complex polycrystal yield surfaces or to distort portions of them, are briefly discussed.

[*]Corresponding author: NTNU, Alfred Getz veg 2, 7491 Trondheim, Norway, +47 90084946, Bjorn.Holmedal@ntnu.no

CONTROL STRATEGY OF TWIST SPRINGBACK FOR AN ASYMMETRIC THIN-WALLED TUBE SUBJECTED TO ROTARY DRAW BENDING

Xin Xue*, Juan Liao, Gabriela Vincze, António B. Pereira

Centre for Mechanical Technology and Automation, Department of Mechanical Engineering, University of Aveiro, 3810-193, Aveiro, Portugal

ABSTRACT: This paper aims to investigate the control strategy of twist springback of an asymmetric thin-walled tube after mandrel rotary draw bending, which is a complex nonlinear physical process with coupling multi-factor interactive effects. By using the improved finite element model [1], two process control strategies related to the mandrel nose placement and the axial push assistant loading are proposed for the efficient reduction of twist springback. The simulation results indicate that the mandrel nose placement mainly affect the springback but not twist deformation. The springback angle is firstly increased and then decreased after several forward tests. The other control strategy, additional axial push assistant loading, is possible to reduce twist deformation, but the risk of springback of bending angle and wrinkle in the intrados sidewall also rises.

REFERENCE:

[1] Xue, X., Liao, J., Vincze, G., Gracio, J. 2015. Modelling of mandrel rotary draw bending for accurate twist springback prediction of an asymmetric thin-walled tube. Journal of Materials Processing Technology 216, pp405-417.

* Corresponding author: Email address: xin@ua.pt, Tel: (+351) 923232366, Fax: (+351) 234 370 953

CORRELATION MICROSTRUCTURES AND LOCAL MECHANICAL PARAMETERS IN THE FE-MN-AL-C TWIP STEELS

Igor Bdikin[1*], Budhendra Singh[1], Maxim Silibin[2], Marina Borodachenkova[1], Gabriela Vincze[1]

[1]TEMA-NRD, Mechanical Engineering Department and Aveiro Institute of Nanotechnology (AIN), University of Aveiro, 3810-193 Aveiro, Portugal
[2]National Research University of Electronic Technology "MIET", 124498 Moscow, Russia

ABSTRACT: Recent advancements in the process technology of nano- and micro-structures enable to extend the various functions in mechanical characteristics of steels. It is well known that the properties of different steels are determined by their crystal lattice structures, that is the spatial arrangement of their atoms and grain structures. The iron-manganese Twinning Induced Plasticity (TWIP) steels derive their exceptional properties from an additional specific strengthening mechanism: twinning. In this case for effective reinforcement the critical strain for strong load transfer knowledge of TWIP local mechanical properties are important, which can also be enhanced or decreased through the formation of special twinning and dislocation structures. In our work the structure of the TWIP steels: stress, texture, twin density and dislocations were been determined from X-ray diffraction analysis. Micro grain structure parameters of the TWIP steels were been analyzed by atomic force microscopy. Hardness and elastic modulus from the load-displacement data were obtained by nanoindentation for different level of deformations of the TWIP steels.

[*] Corresponding author: postal address: Department of Mechanical Engineering, Centre for Mechanical Technology and Automation, University of Aveiro, 3810-193 Aveiro, Portugal, phone: +351 923257029, fax: +351 234370953, email address: bdikin@ua.pt

ASSESSMENT OF DIFFERENT DUCTILE DAMAGE MODELS AND EXPERIMENTAL VALIDATION

Rui Amaral[1*], Pedro Teixeira[2], Abel D. Santos[1,2], J. Cesár de Sá[1,2]

[1]INEGI, Institute of Science and Innovation in Mechanical and Industrial Engineering, R. Dr. Roberto Frias, 400, 4200-465, Porto, Portugal
[2]FEUP, Faculty of Engineering, University of Porto, R. Dr. Roberto Frias, 4200-465, Porto, Portugal

ABSTRACT: The constant goal in automotive industry to achieve a better fuel economy, lower costs and better properties, a new generation of materials are seeing their usage and implementation increase. However, this usage leads to difficulties in the prediction of material behaviour during the sheet metal forming processes, thus challenging the numerical simulation. This paper seeks to contribute in the prediction of fracture on sheet metal alloys. Three constitutive damage models are used, Lemaitre's, GTN and Johnson-Cook, to simulate, as realistically as possible, the mechanical behaviour of the sheet metal material. The corresponding parameters of damage models are identified using an inverse analysis procedure, based on the experimental test data. Finally, to validate and verify the applicability to predict the fracture of the studied damage models, experiments are compared with FE simulations.

[*]Correspondingauthor: R. Dr. Roberto Frias, 400, 4200-465, Porto, Portugal, +351 229578710, ramaral@inegi.up.pt

TWIST SPRINGBACK ANALYSIS IN CURVED CHANNEL FORMING BASED ON A DISTORTIONAL HARDENING MODEL

Juan Liao[1*], Xin Xue[1], Frederic Barlat[2], Myoung-Gyu Lee[3],Gabriela Vincze[1], Antonio, B. Pereira[1]

[1]Centre for Mechanical Technology and Automation, Dep. Mechanical Engineering, University of Aveiro, 3810-193, Aveiro, Portugal
[2]Materials Mechanics Laboratory, Graduate Institute of Ferrous Technology, Pohang University of Science and Technology, San31, Hyoja-Dong, Nam-Ku, Pohang, 790-784, South Korea.
[3]Department of Materials Science and Engineering, Korea University, Anam-dong, Seongbuk-gu, Seoul, South Korea.

ABSTRACT: A recent distortional hardening model [1], which takes into account the evolution of plastic anisotropy of materials under various strain path change, is applied in the curved channel forming process. A series of mechanical tests including uniaxial/ biaxial tension, bulge, forward-reverse shear, tension-tension tests were conducted for parameter identification of the material models. The degradation of elastic modulus under different loading conditions was also tested and modeled. The elastic-plastic constitutive model is implemented in the finite element model for the twist springback prediction of the complex channel forming process. The strain path change during the deformation and the occurrence of twist is analyzed. The influence of the hardening model and variation of elastic modulus on twist springback prediction is discussed.

KEYWORDS: Twist, Springback, Anisotropic hardening, Simulation

REFERENCE:

[1] Barlat F., Vincze G., Gracio J.J., Lee M.G., Rauch E.F., Tome C.N., (2014) Enhancements of homogeneous anisotropic hardening model and application to mild and dual-phase steels, International Journal of Plasticity, 58, 201–218.

* Corresponding author: postal address: Department of Mechanical Engineering, Centre for Mechanical Technology and Automation, University of Aveiro, 3810-193 Aveiro, Portugal, phone: +351 923000422, fax: +351 234370953, email address: jliao@ua.pt

Microstructure and properties of materials

RESIDUAL STRESSES IN TEXTURED HCP TITANIUM; COMPARISON OF EXPERIMENTAL AND PREDICTED DATA

S. Dufrenoy[1], T. Chauveau[1], R. Brenner[2], B. Bacroix[1*]

[1]LSPM – CNRS, Université Paris 13, 99 av. J.B. Clément, 93430 Villetaneuse, France
[2] Institut Jean Le Rond d'Alembert, CNRS - Université Pierre et Marie Curie, UMR 7190,4 place Jussieu, Paris, France

ABSTRACT: For polycrystalline materials, the experimental determination of residual stresses usually neglects the 2nd order fluctuations arising from plastic or thermal incompatibilities from grain to grain. This constitutes a serious limitation, since these stresses are known to have a major influence on the mechanical behavior of textured metallic alloys.
In this paper, a new measurement methodology is first compared to classical ones. Then, the simulation of a tensile test is performed using a self-consistent model, to constitute a virtual experimental data set. The 1st and 2nd order stresses are extracted from the simulation. Two approaches (the classical $\sin^2\psi$ method and a newly developed method) are used to quantify the 1st order stresses from these data. It is shown that the newly developed method allows to minimize the error made by neglecting the so-called 2nd order stresses and leads to a better quantitative estimation of the 1st order stresses.

* Corresponding author: LSPM – CNRS, Université Paris 13, 99 av. J.B. Clément, 93430 Villetaneuse, France, 01 49 40 34 66, brigitte.bacroix@univ-paris13.fr

INVESTIGATION OF PLASTIC DEFORMATION OF HALITE SINGLE CRYSTALS : EXPERIMENTS AND IN-SITU OBSERVATIONS CONFRONTED TO CP-FEM SIMULATIONS

J. L. Raphanel*, A. Dimanov and D. Picard

LMS, CNRS, Ecolepoly technique, Université Paris Saclay, 91128 Palaiseau, France

ABSTRACT: In order to study and model the plasticity of NaClpolycrystals, we have performed a multi-scale investigation of the plastic behavior of NaCl single crystals at room and elevated temperature. Several crystals with chosen orientations have been deformed by uniaxial compression in macroscopic experiments and inside a Scanning Electron Microscope. Observations and Digital Image Correlation computations have allowed the identification of active systems and the mechanical testing has also allowed the evaluation of the initial critical shear stresses associated with each family of potential slip system. CP-FEM computations seem to agree with experiments but in general predict more active systems than the observations. Furthermore, on high symmetry orientations, EBSD measures show local rotations that cannot be explained in a straightforward way by the model. These discrepancies and their consequence for polycrystal behavior will be discussed.

*Corresponding author: LMS, CNRS, Ecolepolytechnique, Université Paris Saclay, 91128 Palaiseau, France, raphanel@lms.polytechnique.fr

BRIDGING MACROPLASTICITY TO MICROPLASTICITY IN STRENGTHENING CERAMIC MATRIX COMPOSITES WITH DUCTILE NETWORKS

J. M. Vieira[1*], B. A. Almeida[2], A. B. Lopes[1], M. X. Gao[3]; Y. Pan[3] and F. J. Oliveira[1]

[1]Department of Ceramics and Glass Engineering/ CICECO, University of Aveiro, Aveiro 3810-193, Portugal, jvieira@ua.pt , augusto@ua.pt , filipe@ua.pt
[2]Monocomp Instrumentacion SA Portugal, 3830-620 Gafanha da Nazaré, Portugal, bruno@monocomp-instrumentacion.com
[3]Department of Materials Science and Engineering, Zhejiang University, Hangzhou, 310027, P. R. China, e-mail, gaomx@zju.edu.cn , yipan@zju.edu.cn

ABSTRACT: Toughening hard but brittle ceramic matrixes with ductile networks forming composites is effective in creating more reliable hard materials whenever refractoriness in use is not at stake. Hardmetal and cermets are well established ceramic-metal composites of today. By combining ductility of metallic alloys and intermetallics with high hardness of TiC, SiC, B4C and other carbides in a smart way, composite materials with Weibull modulus in excess of 20 besides being tough and extremely hard were created. Direct bonding of structure elements of the ceramic is not necessarily expected in hard metals but it may exist in given cermets from limited wettability of the ceramic by the metals. For high volume fraction of the ceramic in the later composites the ductile network turns into a wire-frame like structure filling spaces along edges of the ceramic grains and at their corners, or it may become just a dispersion of isolated ductile inclusions mostly at ceramic grain corners if the metal fraction decreases below 5 % by volume. When the dimensional scale for dimple rupture of ductile phase compares to cross dimensions of the intergranular spaces of the ceramic coupling of instability in ductile fracture to notch sensitivity in Griffith brittle fracture is intensified and help in explaining the tear modulus and parameters of the R-curve of fracture toughness of the composites with inter-penetrating microstructures. High rupture strengths of composites with fine grain sizes and limited volume fractions of ductile ligaments can be found in composites with high values of the strain hardening coefficient and large debond lengths of the ductile phase.

* Corresponding author: Department of Ceramics and Glass Engineering/ CICECO, University of Aveiro, Aveiro 3810-193, Portugal, jvieira@ua.pt

THE ROLE OF CHROMIUM CARBIDES DISTRIBUTION ON THE CRACK PROPAGATION MECHANISM UNDER THREE-POINT BENDING TEST IN MARTENSITIC STAINLESS STEEL

Alvise Miotti Bettanini[a*], Laurent Delannay[a], Pascal J. Jacques[a], Thomas Pardoen[a], Guillaume Badinier[b], Jean-Denis Mithieux[b]

[a]Institute of Mechanics, Materials and Civil Engineering, Universite catholique de Louvain, B-1348 Louvain-la-Neuve, Belgium
[b]Aperam Research Center, BP 15, 62230 Isbergues, France

ABSTRACT: Martensitic stainless steels (MSS) are valid candidates for automotive applications as they present a good combination of mechanical and functional properties which improves the safety and efficiency of new vehicles. However, these steels show limited fracture strain under three-point bending conditions. The fracture strain is controlled by the evolution of ductile damage as the material is plastically deformed, which in turn is influenced by microstructural features such phase ratio and carbides distribution. In this work, a modified AISI 410 MSS is heat treated in order to change the carbides distribution by dissolving part of the Cr-rich carbides while keeping the same phase ratio of ferrite and martensite. Each sample is tested under three-point bending and the crack tip is reconstructed by serial sectioning. The importance of the carbides distribution parameters (volume fraction, interparticle distance and size) on the crack propagation mechanism is assessed in order to link the material ductility to the critical microstructure constituents.

[*]Corresponding author: Institute of Mechanics, Materials and Civil Engineering, Universitecatholique de Louvain, B-1348 Louvain-la-Neuve, Belgium, alvise.miotti@uclouvain.be

Multiscale and Constitutive modelling

ON THE INFLUENCE OF BOUNDARY CONDITITONS ON SHEET METAL FORMING DEFECTS PREDICTION

D.M. Neto[1], M.C. Oliveira[1], J.L. Alves[2], A.D. Santos[3]and L.F. Menezes[1*]

[1]CEMUC, Mechanical Engineering Department, University of Coimbra
[2]CMEMS, Microelectromechanical Systems Research Unit, University of Minho
[3]FEUP, Faculty of Engineering, University of Porto

ABSTRACT: The integration of numerical simulation in the design and development of sheet metal forming processes is a key factor for the fulfilment of the increasing requirements for time and cost efficiency. However, this demands for accurate numerical models, namely constitutive models, finite elements and accurate treatment of the frictional contact conditions. Despite the many advances in the numerical simulation tools development, the accurate prediction of geometrical defects still represents a challenge for the numerical simulation. For instance, it is known that wrinkling prediction is strongly affected by the finite element discretization and springback prediction by the model selected to describe the material kinematic hardening behavior.
This study presents the experimental and numerical analysis of a rail with a high tendency to develop both wrinkling (top surface of geometry) and springback (at the flange), thus representing an additional challenge to simulation, due to a possible interaction of effects. Globally, the numerical results show good agreement with the experimental measurements, but the shape of the wrinkle is significantly influenced by the symmetry conditions considered in the model.

[*]Corresponding author: Polo II, Rua Luís Reis Santos, Pinhal de Marrocos, Coimbra, 3030-788, Portugal, +351239790700, +351239790701, luis.menezes@dem.uc.pt

MODELLING THE SELECTIVE LASER MELTING PROCESS AT THE SCALES OF THE POWDER AND THE PART

Pierre-Yves DURAND[1, 2*], Marion GIRARD[1], Baptiste GIRAULT[1] , Bruno COURANT[1]

[1]Institut de Recherche en Génie Civil et Mécanique (UMR CNRS 6183), Université de Nantes, Saint Nazaire, France
[2]CERO, Parc d'activités des Ecobuts, Challans, France

ABSTRACT: Additive manufacturing processes have a great industrial potential through the production of high added value parts. Selective Laser Melting (SLM) is one of them in which the part is built layer by layer thanks to the melting of metallic powder beds with a laser source. A key point to control the process is a better insight of the related physical phenomena that can be achieved through modelling and simulation.
This work presents a two scales modelling. The first scale is the powder that is used to model the melting of powder bed and its resulting track. Numerical results and optical observations will be compared. The second scale is the part one. The part building is modeled to predict the temperature field or/and residual stress.

KEYWORDS: additive manufacturing, selective laser melting, modelling, simulation

*Corresponding author: Pierre-Yves DURAND, CERO / Institut de Recherche en Génie Civil et Mécanique (UMR CNRS 6183), Université de Nantes. Email : pierre-yves.durand.durand@univ-nantes.fr . Phone : +33 (0)6.45.16.47.46

PARAMETER IDENTIFICATION OF THE CHABOCHE NONLINEAR KINEMATIC HARDENING USING THE VIRTUAL FIELDS METHOD

Jiawei Fu[1*], Frédéric Barlat[1], Jin-Hwan Kim[1], Fabrice Pierron[2]

[1]Graduate Institute of Ferrous Technology, Pohang University of Science and Technology, Pohang, Gyeongbuk 790-784, Republic of Korea,
[2]Faculty of Engineering and the Environment, University of Southampton, Southampton SO17 1BJ, UK

ABSTRACT: In this work, the virtual fields method is applied to identify the constitutive parameters of the Chaboche nonlinear kinematic hardening model for selected advanced high strength steel sheets subjected to a few forward-reverse loading cycles. First, for validation purpose, the proposed identification methodology is applied to a finite element model to check its feasibility in retrieving the target constitutive parameters. The identification results show that the input parameters can be successfully retrieved from the simulated forward-reverse simple shear tests. Then, the proposed methodology is applied to the experimental data of the forward-reverse simple shear test for the selected advanced high strength steels, from which the Chaboche kinematic hardening parameters are obtained. Finally, the shear stress/strain curves predicted by the identified parameters are compared to their experimental counterparts, showing good agreement.

[*]Corresponding author: Jiawei Fu, GIFT-POSTECH, Pohang, Gyeongbuk 790-784, Republic of Korea, Tel: +82 (0)542799052, jiaweifu@postech.ac.kr

MODELLING OF TENSION-COMPRESSION ASYMMETRY AND ORTHOTROPIC BEHAVIOUR OF METALLIC MATERIALS: PARAMETERS IDENTIFICATION PROCEDURE

P.D. Barros[1*], M.C. Oliveira[1], J.L. Alves[2] and L.F. Menezes[1]

[1]CEMUC, Mechanical Engineering Department, University of Coimbra
[2]CMEMS, Microelectromechanical Systems Research Unit, University of Minho

ABSTRACT: This work mainly focuses on the sensitivity analysis of the constitutive parameters of the yield criterion developed by Cazacu et al. (2006) [1], which accounts for both tension–compression asymmetry and orthotropic anisotropy in plastic flow. Based on this analysis, a parameters identification procedure is proposed and employed for materials with both hexagonal closed packed and cubic structures. The procedure takes into account the uniaxial tension and compression results as well the *r*-values, in several directions from the rolling direction. However, due to the experimental difficulties on uniaxial compression tests in case of thin metallic sheets, an identification procedure that takes into account only uniaxial tensile data and the biaxial stress value is also proposed, based on the equivalence between the equibiaxial and the through-thickness uniaxial compression stress states. The results show that it is possible to characterize the orthotropic behavior and the strength differential effects, even if uniaxial compression data is not available, using the proposed procedure.

[1] O. Cazacu, B. Plunkett, F. Barlat, Orthotropic yield criterion for hexagonal closed packed metals, International Journal of Plasticity, 22, 1171–1194, 2006.

[*]Corresponding author: Polo II, Rua Luís Reis Santos, Pinhal de Marrocos, Coimbra, 3030-788, Portugal, +351239790700, +351239790701, marta.oliveira@dem.uc.pt

Manufacturing processes

LARGE SCALE ADDITIVE MANUFACTURING USING ECO-COMPOSITES

J. F. Horta[1*], F. J. P. Simões[1], A. Mateus[1]

[1]CDRsp – Center for RapidandSustainableProductDevelopment, Centro Empresarial da Marinha Grande, Rua de Portugal – Zona Industrial, 2430-028 – Marinha Grande, Portugal

ABSTRACT: The evolution of additive manufacturing processes is enabling the production of parts with improved dimensional accuracy, mechanical, physical and chemical properties. New materials also contribute to this trend, and in this scope, eco-composites, materials with environmental and ecological advantages, which include natural polymers, have been acquiring increased relevance. The purpose of this study is to develop composite material parts manufactured from recycled thermoplastics and natural fibers, such as wood residues. Additive manufacturing will be employed, through the use of a robotic arm and an extruder head. The objective is to access the influence of the main manufacturing parameters, such as temperature, distance between layers or deposition speed, on the final part obtained. Reverse engineering and several material analysis techniques will be employed to achieve this goal.

[*]Corresponding author: Centro Empresarial da Marinha Grande, Rua de Portugal – Zona Industrial, 2430-028 – Marinha Grande, Portugal +351244 569441, joao.f.horta@ipleiria.pt

DEVELOPING LOW COST TIME SAVING MOLDS FOR THERMOFORMING OPERATIONS

Daniel Afonso[1,2*], Ricardo Alves de Sousa[1], Ricardo Torcato[2,3]

[1]TEMA: Centre for Mechanical Technology and Automation,
Department of Mechanical Engineering, University of Aveiro,
Campus de Santiago 3810-183 Aveiro – Portugal
[2]Schoolof Design, Management and Production Technologies Northern Aveiro,
University of Aveiro, Estrada do Cercal, 449 3720-509 Santiago de Riba-Ul - Oliveira de Azeméis - Portugal
[3]Centre for Research in Ceramic and Composite Materials, CICECO,
University of Aveiro, Campus de Santiago 3810-183 Aveiro – Portugal

ABSTRACT: Low pressure polymer processing processes as vacuum thermoforming use much simpler molds then high pressure processes like injection. However, despite the low forces involved with the process, molds manufacturing for this operations is still a very material, energy and time consuming operation.
The goal of the research is to develop and validate a method for manufacturing plastically formed sheets metal molds by single point incremental forming (SPIF) operation for thermoforming operation. Stewart platform based SPIF machines allow the forming of thick metal sheets, granting the required structural stiffness for the mold surface, and keeping the short lead time and low cost manufacture, also allowing a low thermal inertia that benefits mold operation.

*Corresponding author: +351968750179, Dan@ua.pt

PRELIMINARY STUDIES OF THE SPIF PROCESS IN OF BRASS ALLOYS

Daniel Fritzen[1*], Gustavo S. De Lucca[1], Anderson Daleffe[1], Jovani Castelan[1], Ricardo J. Alves de Sousa[2] and Lirio Schaeffer[3]

[1]SATC University, Rua Pascoal Meller, 73 - Bairro Universitário - CEP 88805-380 - CP 232, Criciúma/SC – Brazil(daniel.fritzen@satc.edu.br)
[2]Department of Mechanical Engineering, University of Aveiro, 3810-193 Campus Santiago, Aveiro, Portugal(rsousa@ua.pt)
[3]Metal Forming Laboratory –LdTM, of Federal University of Rio Grande do Sul – UFRGS, Av. Bento Gonçalves 9500, CP 15021, Centro de Tecnologia – Campus da Agronomia, CEP 91501-970 Porto Alegre/RS – Brazil

ABSTRACT: This article discusses the preliminary studies of the Single Point Incremental Forming (SPIF) process applied brass alloy Cu-35Zn, with different sheet thicknesses and formed geometries. Despite being a material widely used in industry, with excellent cold formability, there is still no relevant research on this material concerning SPIF. As a result of these preliminary studies, the necessary forces (F) during the process, the true strain (ε_1, ε_2) and maximum wall angle (ψ) supported by materials are presented and discussed.

*Corresponding author: SATC University, Rua Pascoal Meller, 73 - Bairro Universitário - CEP 88805-380 - CP 232, Criciúma/SC – Brazil, daniel.fritzen@satc.edu.br

LASER WELDING OF STEEL DUAL-PHASE 1000

José Pedro Paiva de Sá Amorim* **and António B. Pereira**

Centre for Mechanical Technology and Automation, Department of Mechanical Engineering, University of Aveiro, 3810-193, Aveiro, Portugal

ABSTRACT: Humanity is facing one of the worst environmental crisis in its history – the global warming. This phenomenon, caused mainly by the burning of fossil fuels has led to considerable increase in Earth's average temperature resulting in changes in the ecosystems endangering the existence of life.

It has been developed less polluting solutions but these are often costly and difficult to implement. The easiest and most affordable way to reduce vehicle emissions has been the development of new materials that tend to be less heavy and resistant so reduce the weight of the cars and hence fuel consumption and therefore reduce the emissions of dioxide carbon.

This work aims to show the influence of laser parameters on penetration welding of the steel dual-phase 1000 and determine the laser parameters needed to obtain a good welding of this steel. For this, an experimental study was carried out. This study consisted in the following main tasks: machining of samples, laser welding, cutting, polishing, chemical etching, grinding, tensile testing, nano-indentation and, through optical and electron microscopy, the examination of the penetration, microstructure and heat affected zone.

*Corresponding author: josepamorim@ua.pt, (+351) 919 193 400

Virtual Design and Simulation: the Role of Computational Mechanics

DESIGN STRATEGIES FOR THE DEVELOPMENT OF MECHANICAL TESTS TO CHARACTERIZE SHEET METALS

A. Andrade-Campos[1*], Nelson Souto[1], Sandrine Thuillier[2]

[1]Grids Research Group, Department of Mechanical Engineering, Centre for Mechanical Technology and Automation (TEMA), University of Aveiro
[2]Université de Bretagne-Sud, FRE CNRS 3744, IRDL,
F-56100 Lorient, France

ABSTRACT: Full-field measurement methods are mainly used to acquire the strain field developed by heterogeneous mechanical tests. Recent material parameters identification strategies based on a single heterogeneous test have been presented considering that a non-homogeneous strain field can lead to a full complete mechanical characterization of the sheet metals. The purpose of this work is to present and discuss different strategies for the design of a heterogeneous test that promotes an enhanced mechanical behavior characterization of thin metallic sheets, under several strain paths and strain amplitudes. Specifically, and to achieve this goal, a design optimization strategy finding the appropriate specimen shape of the heterogeneous test can be used. However, different boundary descriptions and the definition of the objective function, that lead the design optimization process, change the final results. Interesting design results are presented, compared and discussed as well as prospects for future developments are outlined.

*Corresponding author: Campus Universitário de Santiago, 3810-193 Aveiro, Portugal, gilac@ua.pt

NUMERICAL SIMULATION OF FRICTION STIR WELDING OPERATIONS WITH A SOFTENING-BASED CONSTITUTIVE MODEL

R.A.F. Valente[1*], R.M.F. Paulo[1], P. Carlone[2], G.S. Palazzo[2], F. Teixeira-Dias[3]

[1]GRIDS Research Group, Center of Mechanical Technology and Automation, Department of Mechanical Engineering, University of Aveiro, Portugal
[2] Department of Industrial Engineering, University of Salerno, Italy
[3] Institute for Infrastructure and Environment, School of Engineering, University of Edinburgh, United Kingdom

ABSTRACT: In this work a numerical model is proposed to simulate Friction Stir Welding (FSW) joining processes in AA2024-T3 plates. The computational framework includes a softening model that accounts for the temperature history as well as the hardness distribution on a welded plate, in order residual stress levels and geometric deviations of the joined part can be predicted. The validation of the model is carried out using experimental measurements of the hardness in the plate cross-section, with a retrofitting of residual stress components experimentally obtained with the contour method, that are then used as calibration variables for the computational model. The proposed computational toolkit and fundamental procedures are proven to provide a reliable way for the prediction of material softening effects in the Heat Affected Zone (HAZ), as well as of the overall structural behavior of the joined final component.

[*]Corresponding author: Campus Universitário de Santiago, 3810-193 Aveiro, Portugal, robertt@ua.pt

NUMERICAL INVESTIGATION OF AN ARC INLET STRUCTURE EXTRUSION DIE FOR LARGE HOLLOW SECTION

Pan Jian-Yi*

School of Mechanical and Automotive Engineering, Guangzhou College of South China University of Technology, Guangzhou, China, 510800

…

ABSTRACT: The structure design of extrusion dies plays an important role on their service life in the mass production of the extrusion forming process, especially for the profiles of large hollow section. This paper aims to improve the working life of extrusion die by optimal structure design. First, an arc shape inlet die structure for an aluminum large hollow section profile was developed. Second, three-dimensional finite element model of porthole extrusion process was established by using an Arbitrary Lagrangian-Eulerian method. Third, the comparison of the formability including the diversity of extrusion force and uniformity properties between the proposed design and two traditional design schemes under the same forming process configuration was discussed. The results indicate that the novel structure design of the arc inlet die has a longer work life than the others.

*Corresponding author: Pan Jian-Yi.Postal address:No.1, Xuefu Road, Huadu District, Guangzhou, China , Phone: +86-13602416724, Fax:020-36903401, Email address:jianyi52@sohu.com

Nanoengineering

ELECTRICAL CONDUCTIVITY AND STRUCTURAL PROPERTIES OF REDUCED GRAPHENE OXIDE BASED SAMPLES

Olena Okhay[1*], Catarina Dias[2], Joao Ventura[2], António Manuel de Bastos Pereira[1], Elby Titus[1], Alexander Tkach[3]

[1]TEMA - Center for Mechanical Technology and Automation, Department of Mechanical Engineering, University of Aveiro, 3810-093 Aveiro,Portugal
[2]IFIMUP- Institute of Physics of Materials of the University of Porto, 4169-007 Porto, Portugal
[3] CICECO – Aveiro Institute of Materials, Department of Materials and Ceramic Engineering, University of Aveiro, 3810-093 Aveiro, Portugal

ABSTRACT: Graphene (reduced graphene oxide, rGO), a two-dimensional nanocarbon material, has attracted significant attention in recent years due to its extraordinary physical and chemical properties. Thanks to the combination of its excellent mechanical properties and compositional tunability, rGO films as well as free-standing rGO paper-like materials are exciting systems for their potential applications. In the current work structural properties and current-voltage (I-V) characteristics of rGO film-, paper- and membrane-form samples are studied. Variation of the electrical conductivity with the graphene-based samples forms is analyzed.

*Corresponding author: olena@ua.pt

DIAMOND COATINGS FOR MECHANICAL APPLICATIONS

Victor Neto*

TEMA - Centre for Mechanical Technology and Automation, Department of Mechanical Engineering, University of Aveiro, 3810-193 Aveiro, Portugal

ABSTRACT:CVD produced diamond coatings gathers a collection of attractive properties for different mechanical applications, including dental burs, tool inserts, molding tools and dies, mechanical seals and even bio-implants. It presents a hardness above most of the PVD ceramic coatings, displaying good wear and tribological characteristics. Furthermore, it presents high thermal conductivity and a good bio-inertness. With surface modification or the aid of other coatings, it can be deposited with a good adhesion in almost any substrate, in the form of poly (micro)-crystalline, submicron or nanocrystalline morphology. In this presentation, a review of the different diamond-related research paths conducted at TEMA in the past 15 years will be done, focusing both fundamental and applied application developments, with special insight on the developed time-modulated diamond CVD process.

*Corresponding author: vneto@ua.pt

GRAPHENE OXIDE: A UNIQUE NANO-PLATFORM TO BUILD ADVANCED MULTIFUNCTIONAL COMPOSITES

Paula A. A. P. Marques*

NRD-TEMA, Mechanical Engineering Department, University of Aveiro, 3810-193 Aveiro, Portugal

ABSTRACT: Graphene oxide (GO) has received the attention of a considerable number of researchers as it retains much of the properties of the highly valued super material pure graphene, but it is much easier, and cheaper, to make in bulk quantities; easier to process. From the chemical point of view, the presence of oxygen functionalities at GO surface– oxygenated graphene sheets covered with epoxy, hydroxyl and carboxyl groups – is very interesting since they provide reactive sites for chemical modification using known carbon surface chemistry. In this frame GO, because of its easier production and dispersion as well as simple chemical functionalization if compared to graphene, is emerging as a versatile material for applications in nanoscience and nanotechnology.
This presentation addresses the preparation, characterization and potential applications of graphene-based nanocomposites, which have been particularly relevant in our research group at TEMA.

* Corresponding author: Mechanical Engineering Department, University of Aveiro, 3810-193 Aveiro, Portugal, paulam@ua.pt

Challenges in Intelligent Transportation Systems

INTEGRATION OF ROAD TRAFFIC IMPACTS IN INTELLIGENT TRANSPORTATION SYSTEMS (ITS): IMPLICATIONS FOR MECHANICAL ENGINEERING

Margarida C. Coelho*

Dept. Mechanical Engineering / Centre for Mechanical Technology and Automation (TEMA), University of Aveiro, Aveiro, Portugal

ABSTRACT: Road transport will remain a strategic sector in climate change, air pollution and noise. In this context, a more efficient use of existing infrastructures has been identified by the European Union as a key strategy to reduce transport externalities. In line with this strategic orientation, various authors have demonstrated that a smart traffic allocation across multiple routes may result in significant energy savings. The fundamental goal of the FCT @CRUiSE project is to integrate road traffic impacts into a single analytical framework for use in advanced traffic management systems (ATMS). The work plan is founded on 3 main pillars: a) Designing a conceptual methodology for assigning a link-based indicator that can evaluate different traffic-related externalities, adjusted to local contexts of vulnerability; b) Improving the interoperability between traffic-related models and new sources of traffic data; c) Optimizing the network operations by means of a decision support system.

* Corresponding author: University of Aveiro, Dept. Mechanical Engineering, Campus Universitário de Santiago, +351 234 378 172, +351 234 370 953, margarida.coelho@ua.pt

INTERPRETED MODELING FOR SAFETY AND EMISSIONS AT ROUNDABOUTS OR TRAFFIC SIGNALS IN CORRIDORS

Paulo Fernandes[1*], Margarida C. Coelho[1], Nagui M. Rouphail[2]

[1]Dept. Mechanical Engineering / Centre for Mechanical Technology and Automation (TEMA), University of Aveiro, Aveiro, Portugal
[2]Institute of Transportation Research and Education (ITRE), North Carolina State University, Raleigh, USA

ABSTRACT: Roundabouts have been gained increased popularity. The operational performance of roundabouts depends on its geometry, and traffic and pedestrian demand levels, which leads to a trade-off among capacity, safety and emissions. This research is mostly focused on assessing the effects of corridors with different intersections forms in terms of capacity, emissions and pedestrian safety. Vehicle dynamics as well traffic and pedestrian demand data were collected in roundabout corridors in Portugal, Spain, Netherlands and United States. First, traffic performance and environmental impacts of innovative roundabout designs as turbo-roundabouts are analyzed. Second, locations along the corridors where emissions tend to be consistently high are identified followed by a comparison among roundabouts, traffic lights and stop-controlled junctions. Finally, a multi-objective approach is conducted to design optimal crosswalk locations in urban roundabout corridors and to assess the impact of spacing in closely spaced intersection on capacity and emissions.

[*]Corresponding author: University of Aveiro, Dept. Mechanical Engineering, Campus Universitário de Santiago, +351 234 370 830, +351 234 370 953, paulo.fernandes@ua.pt

Energy and Fluid Mechanics

ON THE MAIN SIMILARITIES AND DIFFERENCES BETWEEN NUMERICAL HEAT TRANSFER AND FLUID FLOW, AND THE GOOGLE PAGE RANK FORMULATION

V. A. F. Costa*

TEMA - Centro de Tecnologia Mecânica e Automação, Departamento de Engenharia Mecânica, Universidade de Aveiro, Campus Universitário de Santiago, 3810 - 193 Aveiro, Portugal

ABSTRACT: Interesting similarities and subtle differences exist between numerical heat transfer and fluid flow and the Google Page Rank formulation. Similarities and subtle differences exist on the continuum and discrete nature of the base problems, on the main principles behind the governing equations, on the main principles and steps leading to the *discretization* equations, on the relationships between coefficients of the *discretization* equations, on the matrices of the systems of *discretization* equations, on the relaxation of the *discretization* equations, and on the used methods to solve the *discretization* equations. A parallel analysis of both situations is a challenging exercise, thrice from the physical, algebraic and numerical viewpoints. It is also a motivating exercise for students of algebra and of numerical methods, as so different situations are based on similar analysis, and on similar scientific basis and knowledge.

*Corresponding author: Centro de Tecnologia Mecânica e Automação, Departamento de Engenharia Mecânica, Universidade de Aveiro, Campus Universitário de Santiago, 3810 - 193 Aveiro, Portugal, tel. +351.234.370829, fax: +351.234.370953, email: v.costa@ua.pt

HOUSEHOLD WATER HEATING USING SMALL SCALE WIND TURBINES

M. A. Russo* **and N. Martins**

Department of Mechanical Department, University of Aveiro, Campus de Santiago, Portugal

ABSTRACT: In this paper we study the effectiveness of a small wind turbine for the purpose of household water heating. The aim is to eventually replace the market leading solar collectors in urban areas where solar resources are less than favorable. To achieve these results, climate data for various regions in Portugal were reviewed and, ultimately, based on their wind and solar resource behavior, Aveiro, Nazaré and Angra do Heroísmo were chosen for this study. First, the daily power output of wind turbines and solar collectors in the three areas was simulated during an entire year using two different modeling softwares. A wind profile such as presented in Aveiro is not recommended for wind applications as the wind power is too low to be considered satisfactory. The other locations, Nazaré and Angra do Heroísmo, show optimistic results and are good locations for the implementation of currently commercialized small wind turbines. The results show that wind power can achieve a renewable fraction of 40-70%, in wind profiles similar to Angra do Heroísmo.Second, operational and maintenance costs, including grid purchases, were calculated and compared between wind and solar power. In Continental Portugal, solar power proves to be the most financially viable option. Wind applications should be considered only in Angra do Heroísmo, or locations with a similar wind profile, with a payback period of 5 to 7 years under current technology and costs. Finally, a combination of wind and solar power was considered. A hybrid wind and solar system proves to not be a viable option due to the incompatibility between the available resources. In summary, for a cost-effective deployment in Aveiro and similar regions, the cost of the turbine would have to be lower than what is available under current technology. Nonetheless, with some improvements to the wind turbines, such as cut-in speeds of 1 to 2 m s^{-1} and a decrease in cost of 30-40%, locations with lower wind speeds, such as Nazaré, can be considered as viable options in the future.

*Corresponding author: michaelarusso@ua.pt

DEVELOPMENT OF A LOW-ENERGY GAS SOLENOID VALVE FOR USE IN DOMESTIC WATER HEATERS

Hélder Giesteira[1*], Jorge Ferreira[1,2], Vítor Costa[1,2], Ricardo Carranca[3]

[1] Department of Mechanical Engineering, University of Aveiro
[2] Centre for Mechanical Technology & Automation, TEMA, University of Aveiro
[3] Departamento de Investigação e Desenvolvimento, BoschTermotecnologia S.A.

ABSTRACT: Currently, the actuators of the valves responsible for the gas flow assay in domestic water heating appliances have security measures, usually ensured by a spring. Given the nature of the actuation, high energy consumption is a characteristic of these actuators. In this sense, the present work aims to develop an alternative actuator with greater energy efficiency and a lower response time in order to regulate the gas flow more accurately.
The developed solution consists of a conventional solenoid with a permanent magnet plunger, thus it is possible to obtain a bi-stable actuator with bi-directional movement. The developed concept is modeled and simulated using Matlab – Simulink software. In order to prove the validity of the simulation results, experimental tests with a prototype are also developed.

[*]Corresponding author: Department of Mechanical Engineering, University of Aveiro, gaspargiesteira@ua.pt

DEVELOPMENT OF A LOW ENERGY CONSUMPTION PROPORTIONAL VALVE FOR WATER FLOW REGULATION

Paulo Soares[1*], Jorge Ferreira[1,2], Vítor Costa[1,2],Raquel Vaz[3]

[1] Department of Mechanical Engineering, University of Aveiro
[2] Centre for Mechanical Technology & Automation, TEMA, University of Aveiro
[3] Departamento de Investigação e Desenvolvimento, BoschTermotecnologia S.A.

ABSTRACT: The water flow regulation is a key factor in domestic water heating processes. In this regard, components like the water valves are crucial so that, the correct amount of water is delivered to the heater. This article presents the development of a proportional water valve. The main objectives were to develop and test a prototype of a high performance proportional valve for water flow regulation while presenting a low energy consumption. The development was made using modelling and simulation tools such as MatLab/Simulink™. Besides the conceptual model, a prototype was built to test and validate the simulation results.

[*]Corresponding author: paulomarcelinosoares@ua.pt

Biomechanics

ELASTO-PLASTIC ANALYSIS OF THE FEMUR/ FEMORAL STEM INTERACTION USING MESHLESS METHODS

Marco Marques [1], Jorge Belinha[1,2*], Vinga, S.[3], L.M.J.S. Dinis[1,2], Renato Jorge[1,2]

[1]Institute of Mechanical Engineering and Industrial Management (INEGI), University of Porto, Portugal
[2] Faculty of Engineering of the University of Porto (FEUP), Portugal
[3] Institute of Mechanical Engineering (IDMEC), IST, Portugal

ABSTRACT: Total hip arthroplasty (THA) is a surgical procedure in which the hip joint is totally replaced by an artificial acetabular cup, fixed in the iliac bone; by a femoral stem, fixed in the femoral shaft; and by a femoral head linking both components. In this work, an elasto-plastic analysis of a femur with and without a stem was performed. Three stem designs were used during the analysis. Using the Natural Neighbour Radial Point Interpolation Meshless Method, considering the two-dimensional plane strain approach, this study allows to evaluate the nonlinear behaviour of the bone in the presence of a prosthesis. The numerical model of the bone structure was created using medical images, through the segmentation of the bone in the cortical and trabecular types.

Acknowledgments: The authors truly acknowledge the funding provided by Ministério da Educação e Ciência – Fundação para a Ciência e a Tecnologia (Portugal), under grants, SFRH/BD/110047/2015, SFRH/BPD/75072/2010 and SFRH/BPD/111020/2015, and by project funding UID/EMS/50022/2013 "BONESYS" (LAETA inter-institutional projects)

*Corresponding author: jbelinha@fe.up.pt

PRINCIPAL STRAINS BEFORE AND AFTER SHOULDER PROSTHETIC REPLACEMENT. A FINITE ELEMENT ANALYSIS.

Margarida Bola[1*], António Ramos[1], José António Simões[2]

[1]Department of Mechanical Engineering and TEMA, University of Aveiro, Portugal
[2]Arts and Design School, ESAD, Portugal

ABSTRACT: Total shoulder arthroplasty is a well-established procedure. However, failure rate is still high, and glenoid loosening is pointed as main reason. Principal strains before and after surgery were analyzed.
Total shoulder prosthesis was modeled. The humerus and scapula models were obtained through 3D geometry acquisition of composite bone. Cartilage and the inferior glenohumeral ligament were also modeled. The intact shoulder was constructed and the virtual arthroplasty performed, which was observed experimentally. The shoulder models simulates a 90º abduction.
Principal strains at the glenoid were determined, being the highest at the intact model. The major differences between the intact and implanted models is observed at the posterior region.
The fact that strain distribution observed is smaller in the implanted model indicates that bone closer to an implant is more affected by the implant concerning bone remodeling due to the strain-shielding effects. This is thought to be related with glenoid loosening.

[*]Corresponding author: Departamento de Engenharia Mecânica, Universidade de Aveiro, Campo Universitário de Santiago, 3810-193 Aveiro, phone 234 370 830, fax 234 370 953, margarida.bola@ua.pt

Experimental techniques in structural mechanics

STRESS INTENSITY FACTORS IN CENTRAL CRACKED PLATES USING DEAD ZONE STRESS CONCEPT

Bhalekar Bhalchandra.D.[1], Francisco Q. Melo[2*], Bastos Pereira, A. M[2], Carla V. Lopes[2], R.B Patil[3]

[1]Post Graduate student, MGM's Jawaharlal Nehru Engineering college, MGM campus,Aurangabad-431003,MH,India)
[2]Department of Mechanical Engineering,University of Aveiro, 3810-193 Aveiro Portugal
[3]Associate professor,Department of Mechanical engineering,MGM's Jawaharlal Nehru Engineering college, Aurangabad-431003,MH,India

ABSTRACT: This work proposes an alternative tool in the evaluation of stress intensity factors in a plate having a central through crack subjected to uniform remote tensile stress. Though this is a classical problem where the simple and effective solution for the SIF exists, this case study is very useful in the verification of the accuracy of large number of solutions, either bearing the analytical methods or with finite element techniques.
Here we analyzed the stress distribution in the central cracked plate having realized the existence of welldefined geometry zone where stresses are much smaller than other values close to the crack tip or the remote stress edge, practically could be neglected. This could suggest the suppression of material with the so mentioned small stress values giving rise to an equivalent compliance associated with the so mentioned dead zone for stress distribution.
Practical expressions dealing with simple structural mechanics could lead to the calculation of the compliance and the stress intensity factor. Cases analyzed have showed a good agreement with available research literatures.

Keywords: Stress intensity factor, compliance method, dead stress zone

[*]Corresponding author: Department of Mechanical Engineering,University of Aveiro, 3810-193 Aveiro Portugal, +351 234 378 168, +351 234 370 953, francisco@ua.pt

TORQUE MEASUREMENT SYSTEMS EMPLOYING SURFACE ACOUSTIC WAVE DEVICES: CONCEPTION AND CALIBRATION PROCEDURES

André Barata[1*], Joana C. Mendes[1,2*], Luis N. Alves[2,3], Antonio Pereira[2]

[1]Instituto de Telecomunicações, Campus Universitário de Santiago, 3810-193 Aveiro, Portugal
[2]Centre for Mechanical Technology and Automation, University of Aveiro, 3810-193 Aveiro, Portugal
[3]Department of Electronics, Telecommunications and Informatics, University of Aveiro, 3810-193 Aveiro, Portugal

ABASTRACT: Surface Acoustic Wave (SAW) devices are used for remote sensing applications, such as measurement of temperature and strain on inaccessible or moving parts. SAW sensors are fabricated on piezoelectric materials whose properties react to these physical variables. When the sensor is interrogated, an electromagnetic wave reaches the sensor antenna and is converted into a SAW which eventually reflects back to the receiver as an electromagnetic wave. The resonance frequency embeds information about the physical parameter under interest and is measured by the receiver. This paper focuses on the measurement of torque on a rotating shaft with SAW strain sensors using a two sensor bridge. The sensors measure strains in two different directions and the torque is then related to the strains sensed by these two devices. The paper presents the system overview and modeling and describes interrogation and detection algorithms. It also describes calibration procedures under static and dynamic regimes.

[*]Corresponding author: Instituto de Telecomunicações, Campus Universitário de Santiago, 3810-193 Aveiro, Portugal, joanacatarina.mendes@av.it.pt

Long Abstract

PARAMETER IDENTIFICATION OF THE CHABOCHE NONLINEAR KINEMATIC HARDENING USING THE VIRTUAL FIELDS METHOD

Jiawei Fu[1*], Frédéric Barlat[1], Jin-Hwan Kim[1], Fabrice Pierron[2]

[1]Graduate Institute of Ferrous Technology, Pohang University of Science and Technology, Pohang, Gyeongbuk 790-784, Republic of Korea,
[2]Faculty of Engineering and the Environment, University of Southampton, Southampton SO17 1BJ, UK

ABSTRACT: In this work, the virtual fields method is applied to identify the constitutive parameters of the Chaboche nonlinear kinematic hardening model for selected advanced high strength steel sheets subjected to a few forward-reverse loading cycles. First, for validation purpose, the proposed identification methodology is applied to finite element models to check its feasibility in retrieving the target constitutive parameters. The identification results show that the input parameters can be successfully retrieved from the simulated forward-reverse simple shear. Then, the proposed methodology is applied to the experimental data of the forward-reverse simple shear tests for the selected advanced high strength steels, from which the Chaboche kinematic hardening parameters are obtained. Finally, the shear stress-shear strain curves calculated by the identified parameters are compared to their experimental counterparts, showing good agreement.

INTRODUCTION: The Chaboche nonlinear kinematic hardeningrule as proposed by Chaboche[1] is an effective hardening model to capture the Bauschinger effect and permanent softening in reverse loadings during metal forming. The study of these effects is useful to predict the springback phenomenon, commonly seen in sheet metal forming, which results in undesired shape change of a specimen after release of load. To develop Chaboche-based finite element (FE) models, the constitutive parameters of the material must be determined. This is usually implemented by updating a FE model to fit the FEM predicted, e.g. load-displacement curve to the experimental counterpart[2]. The virtual fields method(VFM) [3], on the other hand, does not involve iterative FE calculation and, thus, is computationally efficient in nature. Thus, the objective of the present work is toapply the VFM to calibrate the Chaboche nonlinear kinematic hardening coefficients. First, FE models were developed to simulate the forward-reverse loading in simple shear and to provide strain fields for the proposed VFM scheme in order to check its feasibility of retrieving the target Chaboche constitutive parameters. Then, this method was implemented through forward-reverse simple shear tests of advanced high strength steel (AHSS) sheet specimens.

PROCEDURES, RESULTS AND DISCUSSION: The Chaboche nonlinear kinematic hardening model considered in this study is based on the von Mises yield criterion and a kinematic hardening rule. For a yield condition:

Corresponding author: jiaweifu@postech.ac.kr

$$\mathcal{F} = f(\boldsymbol{\sigma} - \boldsymbol{\alpha}) - \sigma_s(\varepsilon_p) = 0 \quad (1)$$

where:

$$\mathrm{f}(\boldsymbol{\sigma} - \boldsymbol{\alpha}) = \sqrt{\frac{3}{2}(\boldsymbol{s} - \boldsymbol{\alpha}^{dev}) : (\boldsymbol{s} - \boldsymbol{\alpha}^{dev})} \quad (2)$$

The nonlinear kinematic hardening was initially proposed by Armstrong and Frederick[4]:

$$\mathrm{d}\alpha = \frac{C}{\sigma_s}(\boldsymbol{\sigma} - \boldsymbol{\alpha}) d\varepsilon_p - \gamma \boldsymbol{\alpha} d\varepsilon_p \quad (3)$$

where$C$ and $\gamma$are material parameters. It was widened by Chaboche[1]as:

$$\mathrm{d}\alpha_i = \frac{C_i}{\sigma_s}(\boldsymbol{\sigma} - \boldsymbol{\alpha}) d\varepsilon_p - \gamma_i \boldsymbol{\alpha_i} d\varepsilon_p \quad (4)$$

and the overall backstress

$$\boldsymbol{\alpha} = \sum_{i=1}^{N} \boldsymbol{\alpha_i} \quad (5)$$

Voce hardening is considered for the isotropic evolution of the yield surface, thus,

$$\sigma_s(\varepsilon_p) = Y_0 + R_{sat}(1 - e^{-n\varepsilon_p}) \quad (6)$$

The VFM is applied to solve the inverse problem. For a solid of volume V, subjected to a quasi-static loading vector $\boldsymbol{T}$ on the boundary ∂V, an equilibrium can be written as:

$$\underbrace{-\int_V \boldsymbol{\sigma} : \boldsymbol{\varepsilon}^* \, dV}_{Internal\ virtual\ work} + \underbrace{\int_{\partial V} \boldsymbol{T} . \boldsymbol{u}^* dS}_{External\ virtual\ work} = 0 \quad (7)$$

where$\boldsymbol{u}^*$is the virtual displacement vector and $\boldsymbol{\varepsilon}^*$is the corresponding virtual strain tensor.A cost function can be formed as:

$$\mathcal{C}(\boldsymbol{X}) = \sum_{j=1}^{N_j} \left(-b \int_A \left(\int_0^t \dot{\boldsymbol{\sigma}} \, dt \right) : \boldsymbol{\varepsilon}^* \, dS + \int_{\partial V} \boldsymbol{T} . \boldsymbol{u}^* dS \right)^2 \quad (8)$$

The proposed identification procedure has been implemented using MATLAB® program. The identified parameters based on different initial estimates are listed in Tables 1 and 2 for one backstress component and two backstress components, respectively. The FEM calculated stress-strain curves using the identified parameters are compared with the experimental counterpart in Fig. 1, showing good agreement. From these results, it can be concluded that the Chaboche parameters can be identified simultaneously from a forward-reverse simple shear test using the proposed VFM algorithm.

TABLE1 Identification results for the DP600 for the case of one backstress component

	C (MPa)	γ	Y_0(MPa)	R_{sat}(MPa)	n
Initial estimate 1	10000	100	100	10	10
Identified 1	28895	121	281	70.5	34.1
Initial estimate 2	50000	500	500	100	100
Identified 2	28896	121	281	70.5	34.1

TABLE2 Identification results for the DP600 for the case of two backstress components

	C_1(MPa)	γ_1	C_2(MPa)	γ_2	Y_0(MPa)	R_{sat}(MPa)	n
Initial estimate 1	20000	200	2000	20	200	50	10
Identified 1	48874	283	6221	49.3	246	79.7	33.7
Initial estimate 2	80000	500	8000	100	500	100	50
Identified 2	48701	282	6142	48.9	246	79.8	33.7

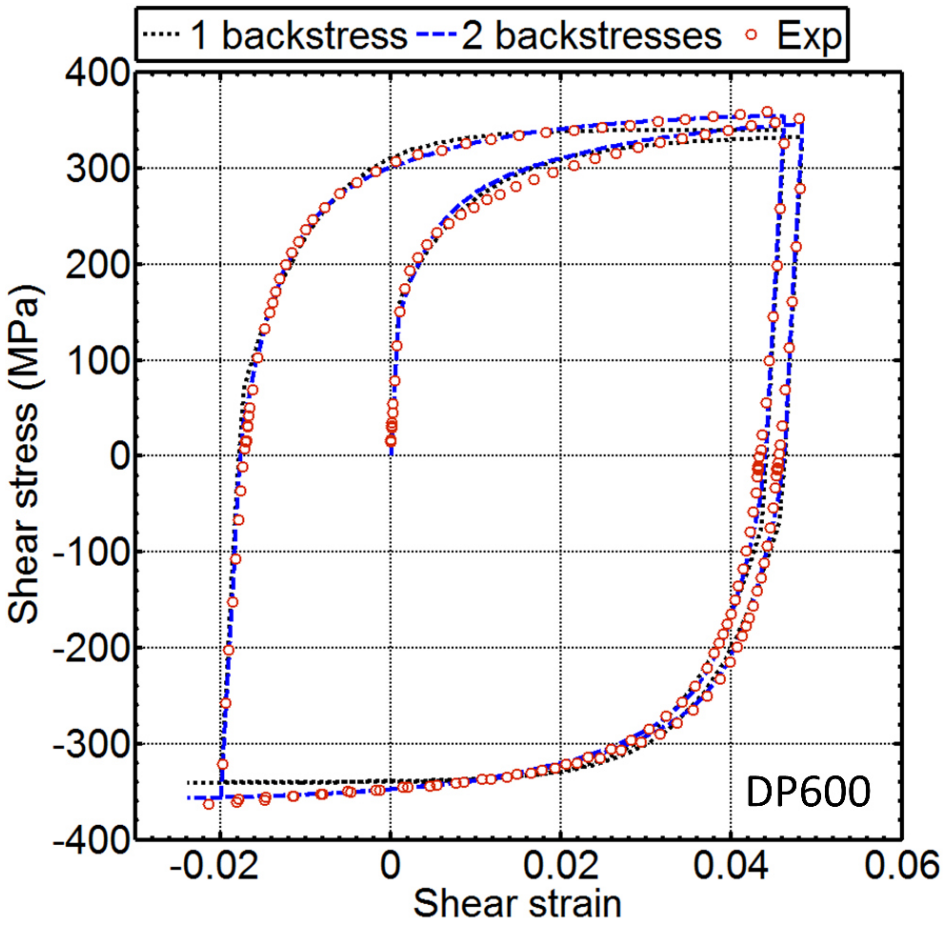

FIGURE 1. Shear stress-shear strain curves for the DP600 in two cycles of forward-reverse simple shear.

Acknowledgement: The authors (Dr. Jiawei Fu, Prof. Frédéric Barlat and Dr. Jin-Hwan Kim) are grateful to POSCO for financial support.Prof. F. Pierron is thankful to the Royal Society and the Wolfson Foundation for providing him support through a Royal Society Wolfson Research Merit Award.

REFERENCES

[1] Chaboche JL. Time-independent constitutive theories for cyclic plasticity. International Journal of Plasticity 1986;2:149-88.
[2] Broggiato G, Campana F, Cortese L. The Chaboche nonlinear kinematic hardening model: calibration methodology and validation. Meccanica 2008;43:115-24.
[3] Grédiac M, Pierron F. Applying the Virtual Fields Method to the identification of elasto-plastic constitutive parameters. International Journal of Plasticity 2006;22:602-27.
[4] Armstrong PJ, Frederick CO. A mathematical representation of the multiaxial Bauschinger effect: Central Electricity Generating Board [and] Berkeley Nuclear Laboratories, Research & Development Dept.; 1966.

ELASTO-PLASTIC ANALYSIS OF THE FEMUR/ FEMORAL STEM INTERACTION USING MESHLESS METHODS

Marco Marques [1], Jorge Belinha[1,2*], Vinga, S.[3], L.M.J.S. Dinis[1,2], Renato Jorge[1,2]

[1]Institute of Mechanical Engineering and Industrial Management (INEGI), University of Porto, Portugal
[2]Faculty of Engineering of the University of Porto (FEUP), Portugal
[3]Institute of Mechanical Engineering (IDMEC), IST, Portugal

ABSTRACT: Total hip arthroplasty (THA) is a surgical procedure in which the hip joint is totally replaced by an artificial acetabular cup, fixed in the iliac bone; by a femoral stem, fixed in the femoral shaft; and by a femoral head linking both components. In this work, an elasto-plastic analysis of a femur with and without a stem was performed. Three stem designs were used during the analysis. Using the Natural Neighbour Radial Point Interpolation Meshless Method, considering the two-dimensional plane strain approach, this study allows to evaluate the nonlinear behaviour of the bone in the presence of a prosthesis. The numerical model of the bone structure was created using medical images, through the segmentation of the bone in the cortical and trabecular types.

INTRODUCTION: In 2012, nearly a half million hip replacement surgeries were performed within the United States, and by 2015, it is expected that costs for primary and revision of THA rise to $21.2 billion. [1]In this work, the femur bone structure was analyzed using an advanced discretization meshless techniques. The Natural Neighbour Radial Point Interpolation Method (NNRPIM), an advanced discretization meshless techniques, is considered a truly meshless method, since it uses the Natural Neighbour concept in order to enforce the nodal connectivity, and the Voronoï diagrams to construct the background integration mesh from an unstructured set of nodes. [2]–[4]

PROCEDURES, RESTULTS AND DISCUSSION: In this study, an elasto-plastic analysis was performed in order to evaluate the behavior of different prosthesis stems. The mechanical proprieties applied to the materials are described in **Table 1**. In all the four models, the bone was fixed as represented in **Figure 1**. The force was applied, in the case of the normal bone, in the femur head, and for the other cases, in the superior partof the stem, as shown in **Figure 1.**For all the cases, a force of 2317 N was applied.

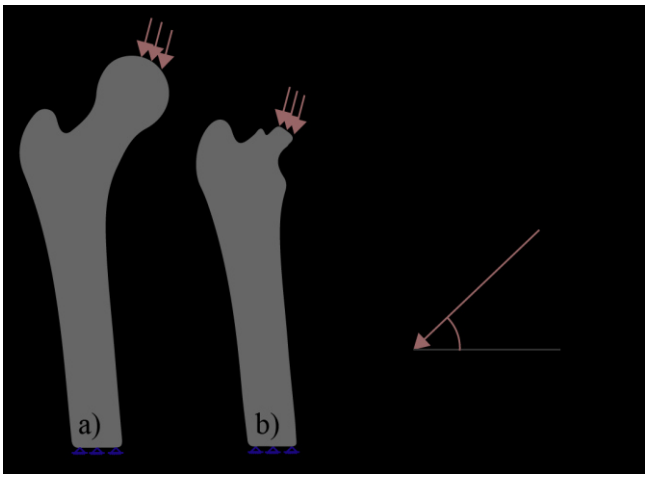

FIGURE 1. Appliedboundary conditions. a) Models with no stem. b) Model with stem.

Table 1 Mechanical properties

	Cortical Bone	**Trabecular Bone**	**Titanium**
E [MPa]	18500	350,5	110000
E_t [MPa]	2200	18,6	880
σ_y [Mpa]	128,9	13,4	550
ν	0,36	0,36	0,3

TABLE 2 Von Mises Effective Stress Field

	FEM	**NNRPIM**
Original Model	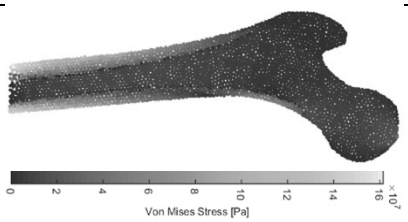	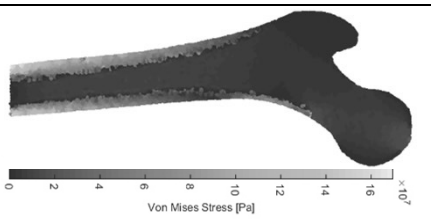
Short Stem Model	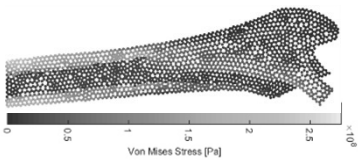	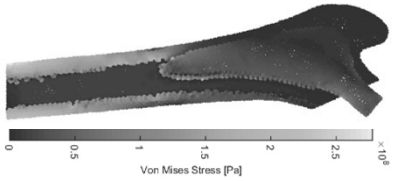
Long and Thin Stem Model	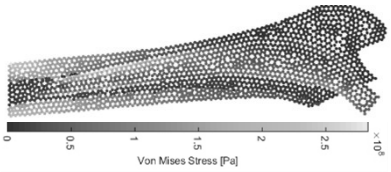	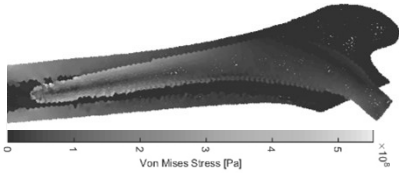
Long Stem Model	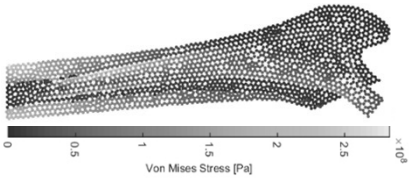	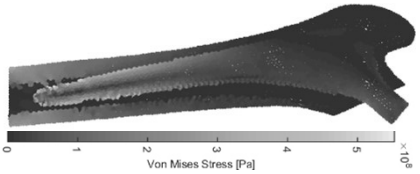

The results shown in **TABLE 2** suggest, firstly, that the presence of the stem lead to a higher value in the von Mises effective stress. Comparing the long stem, they have a very similar behavior. Analyzing the short stem can be said that it leads to a similar vonMises effective stress field when compared to the stemless model. Long bones lead to higher values of stress in the diaphysis bone. Comparing the meshless and fem

analysis, for the stemless bone model and for the short stem model, the results demonstrate that both methodologies lead to the same results. These results corroborate previous works[2]. Thus, once again, from this work it is possible to understand that meshless method (due to its high convergence rate), require a low discretization level to achieve a stable and accurate result.

Acknowledgement: Acknowledgments: The authors truly acknowledge the funding provided by Ministério da Educação e Ciência – Fundação para a Ciência e a Tecnologia (Portugal), under grants, SFRH/BD/110047/2015, SFRH/BPD/75072/2010 and SFRH/BPD/111020/2015, and by project funding UID/EMS/50022/2013 "BONESYS" (LAETA inter-institutional projects)

REFERENCES

[1]C. J. Lavernia, D. A. Iacobelli, L. Brooks, and J. M. Villa, "The Cost-Utility of Total Hip Arthroplasty: Earlier Intervention, Improved Economics.," *J. Arthroplasty*, vol. 30, no. 6, pp. 945–9, Jun. 2015.

[2] L. M. J. S. Dinis, R. M. Natal Jorge, and J. Belinha, "Analysis of 3D solids using the natural neighbour radial point interpolation method," *Comput. Methods Appl. Mech. Eng.*, vol. 196, no. 13–16, pp. 2009–2028, Mar. 2007.

[3] L. M. J. S. Dinis, R. M. Natal Jorge, and J. Belinha, "Analysis of plates and laminates using the natural neighbour radial point interpolation method," *Eng. Anal. Bound. Elem.*, vol. 32, no. 3, pp. 267–279, 2008.

[4] J. Belinha, *Meshless Methods in Biomechanics*, vol. 16. Cham: Springer International Publishing, 2014.

Full paper

MECHANICAL CHARACTERIZATION OF MATERIALS FOR SHEET-BULK METAL FORMING PROCESSES

P. Sieczkarek[1], C.M.A. Silva[2],S. Wernicke[1], A.E. Tekkaya[1]and P.A.F. Martins[2*]

[1]Institute of Forming Technology and Lightweight Construction, TU Dortmund University, BaroperStr. 303, D-44227 Dortmund, Germany

[2]IDMEC, Instituto Superior Técnico, Universidade de Lisboa, Av. Rovisco Pais, 1049-001 Lisboa, Portugal

ABSTRACT: This paper presents a new experimental methodology for determining the stress-strain curve, the fracture toughness and the critical instability strength of plates and sheets to be used in sheet-bulk metal forming (SBMF) applications. The stress-strain curve and fracture toughness are obtained from double-notched test specimens loaded in shear and the material flow behaviour is compared against that obtained from conventional tensile tests. The critical instability streng this obtained from rectangular test specimens loaded in compression by means of a combined experimental and theoretical procedure that makes use of the analytical solution for the elasto-plastic stability of plates subjected to equal uniform compression on two opposite edges. The work is performed in aluminium EN AW-1050 and steel DC04 sheets with 3 mm thickness and the proposed experimental methodology reveals appropriate to the mechanical characterization of materials under the high levels of strain that are commonly found in SBMF processes.

Keywords: Sheet-bulk metal forming, Stress-strain curve, Fracture toughness, Critical instability strength

1. INTRODUCTION

The differences in plastic flow resulting from the plane-stress conditions of sheet metal forming and the three-dimensional stress conditions of bulk metal forming have long been utilized to classify metal forming processes into two different groups. However, recent developments in the production of sheet metal parts with local functional features such as teeth, ribs and solid bosses positioned outside the plane of the sheets from which they are shaped, gave rise to the identification of sheet-bulk metal forming (SBMF) as a new group of metal forming processes that deforms sheets and plates with intended three dimensional plastic flow [1].

From a product development and manufacturing design point of view, typical applications of SBMF require application of loading across (refer to direction ‘S’ in Figure 1) and/or perpendicular (refer to transverse ‘T’ and/or longitudinal ‘L’ directions in Figure 1) to the sheet thickness.

*Corresponding author: Phone: +351-21-8419006, E-mail: pmartins@ist.utl.pt

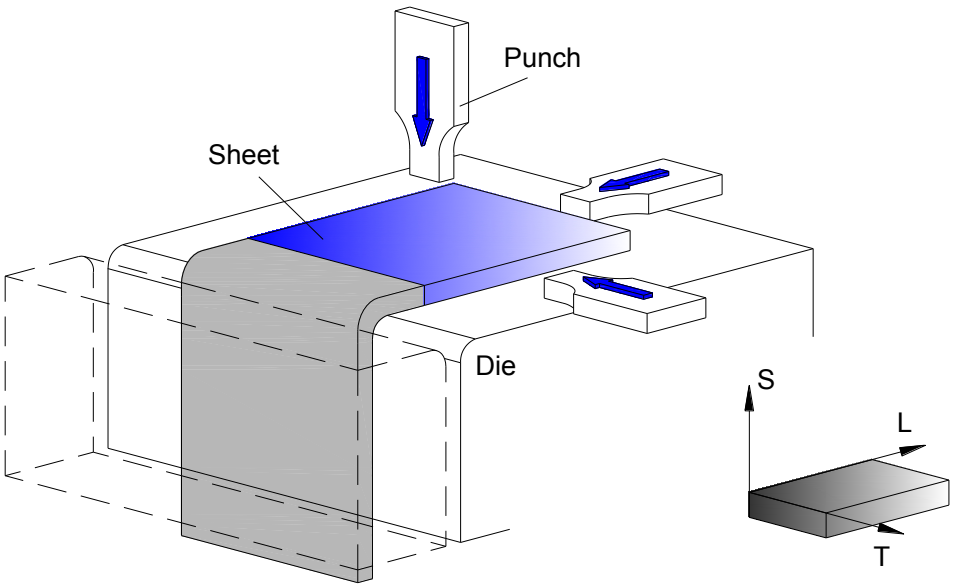

Figure 1 Loading directions in sheet-bulk metal forming (SBMF) processes.

The loading conditions of SBMFare known to raise challenges in the design of tools and in the utilisation of appropriate methods and procedures to determine the stress-strain response, the fracture toughness and the critical instability strength of materials supplied in the form of sheets. The first type of difficulties is attributed to the high forces that are typical of SBMF processes [2] whereas the second type is related to the attainment of high levels of strain.

This paper is focused on the mechanical characterization of materials for SBMF processes with application of loading perpendicular to the sheet thickness. Itsmain objective is to present an overall testing methodology that takes into account the directionality of the mechanical and physical properties of the materials. The determination of the stress-strain curve and fracture toughness is based on the utilization of double-notched test specimens loaded in shear that was proposed by Silva et al. [3] as an alternative to conventional tensile and shear tests [4, 5]. Conventional tensile and shear tests are known to experience difficulties in large plastic strains that are caused bylocalized necking and/orrotation of the plastic shear zone during the application of load. The determination of the critical instability strength is based on the compression of rectangular test specimens with support conditions in both width and height directions that replicate loading conditions that may be found in SBMF processes. A new combined experimental and theoretical procedure that makes use of the analytical solution for the elasto-plastic stability of rectangular plates under equal uniform compression on two opposite edges is employed.

The work is performed in aluminium EN AW-1050 and steel DC04 sheets with 3 mm thickness and the stress-strain curves obtained by means of the double-notched shear test are compared against those obtained from conventional tensile tests.

2. THEORETICAL BACKGROUND

The double-notched shear test utilized in the mechanical and fracture characterization of materials for SBMF applications is schematically illustrated in Figure 2. As seen, the geometry of the tool utilized in the experiments is such that the width w of the specimens does not undergo any change. The test is performed under plane stress conditions and the compression force F applied by the punch on the central part of the

specimens gives rise to shearing along the two symmetric ligaments l that connect each pair of opposite notches. The two dark blue regions of the specimens that are illustrated in the detail (refer to the right picture in Figure 2) represent the material undergoing shear deformation along the ligaments. Both regions with volume V_p are assumed to be confined by rectangular patches (parallelogram patches, after deformation) with a geometry approximately equal to $l \times d$, where the width $d = \alpha l$ of the notches is assumed to be a fraction α of the ligament l.
To conclude, it is worth mentioning that the geometry of the double-notched sheartest specimens was inspired in the double-notched bars loaded in shear that were employed by Atkins [6] to determine fracture toughness under plane strain deformation conditions.

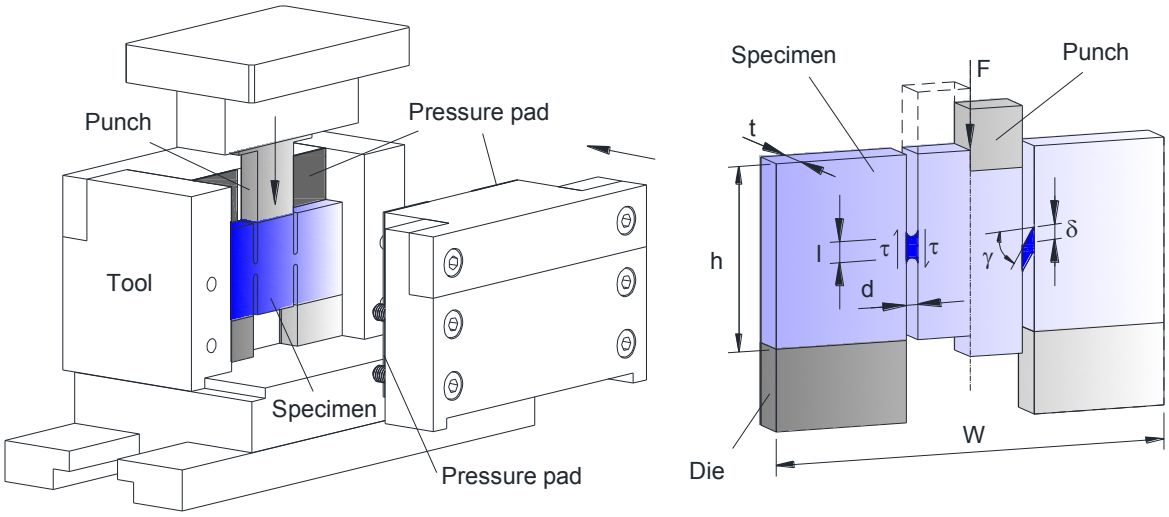

Figure2 Schematic illustration of the tooling apparatus and of the double-notched shear test specimen that were utilised in the mechanical and fracture characterization of sheets.

2.1 Stress-strain curve

The methodology for determining the stress-strain curve by means of double-notched shear tests involves calculation of the shear stresses and strains along the two symmetric plastic shear deformation zones of the specimens up to the instant of time when cracks start to propagate along the ligaments that connect each pair of opposite notches.
The calculation procedure is based in two major assumptions. Firstly, plastic work is considered to be totally consumed by shear deformation inside the two rectangular patches of the test specimens (refer to the detail included in the right side of Figure2). The remaining parts of the specimens are assumed to be rigid because the contribution of elastic deformation is negligible. Secondly, the shear stresses and strains are considered to be uniformly distributed inside the two shear deformation regions.
Under these circumstances, the shear strain γ inside the shear deformation region for a punch displacement equal to δ is given by (Figure 2),

$$\gamma \cong \tan\gamma = \frac{\delta}{d} \tag{1}$$

The corresponding shear stress τ is calculated from,

$$\tau = \frac{F}{2lt} \tag{2}$$

where the punch compression force F is divided by two due to the existence of two symmetric shear deformation regions.
The overall procedure to determine the stress-strain curve is schematically outlined in Figure 3 and the shear stress τ derived from equation (2) may be seen as an average value of the shear stresses acting in both shear deformation zones because it is impossible to separate the exact value of force acting on each zone alone from the experimental evolution of force with displacement (Figure 3a).
From the curve $\tau(\gamma)$ derived from equations (1) and (2) it is possible to determine the flow stress using the von Mises's expressions for the effective stress $\bar{\sigma}$ and effective strain $\bar{\varepsilon}$ (Figure 3b),

$$\bar{\sigma} = \sqrt{3}\,\tau \quad \bar{\varepsilon} = \frac{\gamma}{\sqrt{3}} \tag{3}$$

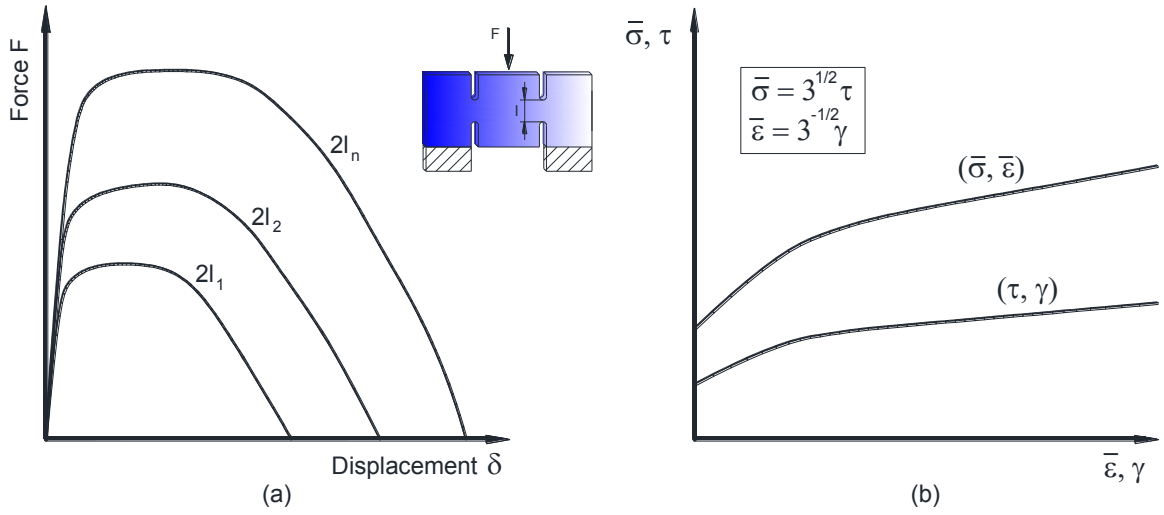

Figure 3 – Determination of the stress-strain curve by means of the double-notched shear test.
a) Schematic representation of the force-displacement evolution for different pairs of ligaments $2l_i$;
b) Schematic representation of the procedure to determine the stress-straincurve $\bar{\sigma}(\bar{\varepsilon})$ from the $\tau(\gamma)$ curve up to the instant of time when cracks are triggered.

2.2Fracture toughness

The determination of fracture toughness involves characterization of the evolution of load with displacement for a number of test cases performed with specimens having different ligaments between the two symmetric opposite notches. The methodology is based on the original work of Cotterell and Reddel [7] for double-notched test specimens loaded in tension (mode I of fracture mechanics), and on the extension for double-notched circular test specimens loaded in plane torsion(mode II of fracture mechanics) that was recently proposed by Isik et al. [8].
The overall calculation procedure assumes that crack propagation in double-notched test specimens loaded in shear is generally preceded by extensive plastic deformation in the two symmetric shear deformation regions. The total work W_T consumed by the end of the test (assuming material as rigid-plastic) is given by,

$$W_T = Fd\delta = 2w_p dV_p + 2RdA \tag{4}$$

where w_p is the plastic work per unit of volume and R is the fracture toughness, defined as the specific essential work of fracture w_f that is necessary to open a crack of area A in each shear deformation region.
From the definition of plastic work per unit of volume, equation (4) can be rewritten as,

$$W_T = 2\left(\int_0^{\bar{\varepsilon}} \bar{\sigma} d\bar{\varepsilon}\right) ld\, t + 2Rtl \tag{5}$$

where $ld = \alpha l^2$ is the area of each shear deformation region of the specimen and α is a constant that allows expressing the width d of the notches as a function of the length l of the ligaments. Dividing the above equation by $2tl$, we obtain the following relation for the total specific work w_T,

$$w_T = \left(\int_0^{\bar{\varepsilon}} \bar{\sigma} d\bar{\varepsilon}\right) \alpha\, l + R \tag{6}$$

By taking into consideration that shear stresses and strains are uniformly distributed inside the shear deformation region it is possible to approximate the integral in equation (6) by the product between the mean flow stress $\bar{\sigma}_{mean}$ and the final average value of the plastic strain $\bar{\varepsilon}_{av}$ for the entire deformation of the specimen. This allows rewriting equation (6) as follows,

$$w_T = \frac{1}{2} \bar{\sigma}_{mean} \bar{\varepsilon}_{av} \alpha\, 2l + R \tag{7}$$

where the mean flow stress $\bar{\sigma}_{mean}$ is calculated by integration of the stress-strain curve between the initial and final average experimental values of plastic strain $\bar{\varepsilon}_{av}$,

$$\bar{\sigma}_{mean} = (1/\bar{\varepsilon}_{av}) \int_0^{\bar{\varepsilon}_{av}} \bar{\sigma} d\bar{\varepsilon} \tag{8}$$

From equation (7) it is possible to conclude that the total specific work w_T can be split into two different terms; (i) the specific non-essential plastic work $w_p = \bar{\sigma}_{mean} \bar{\varepsilon}_{av} \alpha l$ and (ii) the specific essential work of fracture $w_f = R$ (fracture toughness).

Figure 4 outlines the procedure to determine fracture toughness from the experimental evolution of force with displacement for different test specimens with different ligaments. As seen, the evolution of the force F with displacement δ is first registered for a number of test cases performed with specimens having different starting lengths $2l$ of the two symmetric ligaments (Figure 4a). The total energy W_T required by each test case is calculated by integrating the evolution of the force with displacement until separation of the specimen into two parts and subsequently normalized by $2tl$ .The resulting value is plotted as a function of the starting length $2l$ of the two symmetric ligaments by means of a straight line (Figure 4b) in close accordance to equation (7). Fracture toughness R is the y-intercept of this line.

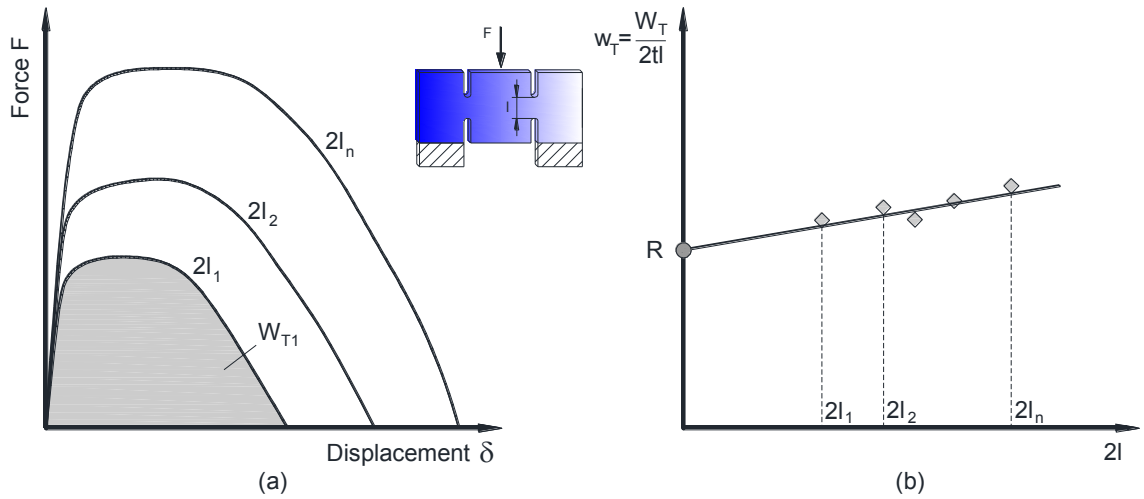

Figure 4 Determination of fracture toughness by means of the double-notchedshear test.

a) Schematic representation of the force-displacement evolution for different pairs of ligaments $2l_i$;

b) Schematic representation of the procedure to determine fracture toughness R from the total specificwork w_T .

2.3Critical instability strength

The application of compression loading perpendicular to the sheet thickness may also give rise to instability in the form of buckling out of the sheet plane. The critical instability strength σ_{cr} to trigger buckling in a sheet is obtained from Timoshenko [9] and is similar to the Euler strength for columns except for the fact that it is a function of the thickness to width ratio t/w , because the shorter the width w the larger the resistance to buckling will be,

$$\sigma_{cr} = K \frac{E}{(1-\nu^2)} \left(\frac{t}{w} \right)^2 \tag{9}$$

In the above equation, the symbol E is the elastic modulus of the material, ν is the Poisson coefficient and K is a parameter related to the support conditions along the width w and height h directions.
By replacing the elastic modulus E in equation (9) by the tangent modulus E_t of the material defined as the slope $d\sigma/d\varepsilon$ of the stress-strain curve and calculating the actual values of width and thickness as follows (where, $\varepsilon_h = \ln(h/h_0)$),

$$t = t_0 \exp^{-0.5\varepsilon_h} \quad w = w_0 \exp^{-0.5\varepsilon_h} \tag{10}$$

it is possible to determine the critical instability strength σ_{cr} by intersecting the material stress-strain curve $\sigma(\varepsilon)$ and the modified form of the instability strength $\sigma_{cr}(\varepsilon)$ given by equation (10) to cope with buckling under plastic deformation conditions. The value of the parameter K related to the support conditions along the width w and height h directions in equation (10) is chosen in order to best match the experimental values of force at the onset of buckling. Figure 5 outlines the overall procedure for determining thecritical instability strength σ_{cr}.

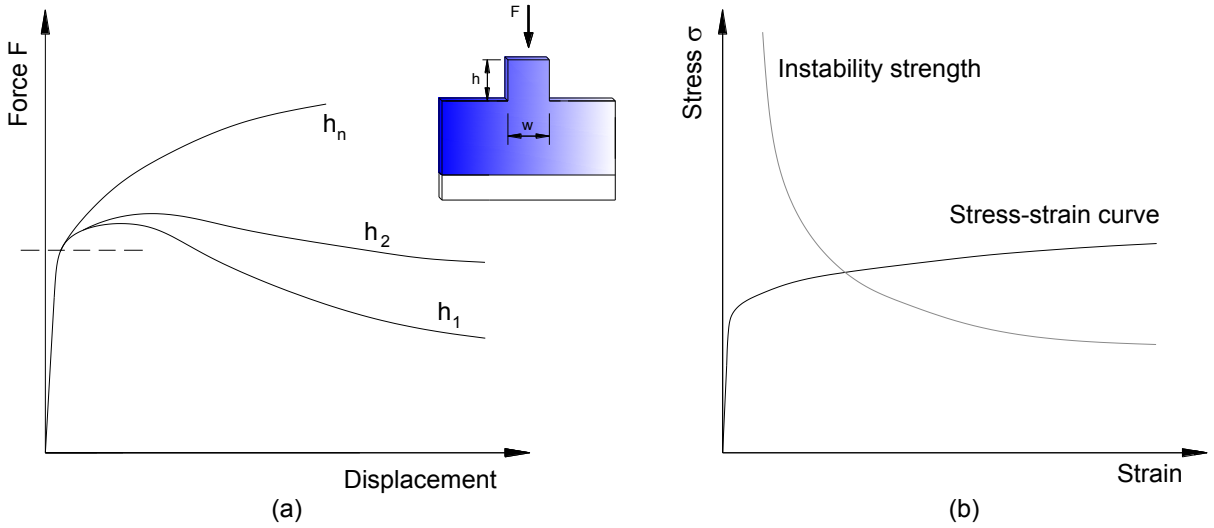

Figure 5 -Determination of the critical instability strength by compressing rectangular test specimens.

a) Schematic representation of the force-displacement evolution for different heights h_i;
b) Schematic representation of the procedure to determine the critical instabilitystrength σ_{cr} under plastic deformation conditions.

3. EXPERIMENTATION

3.1Conventional tensile tests

The experimental work was carried out in aluminium EN AW-1050 and steel DC04 sheets with 3 mm thickness. The sheets were characterized at room temperature by

means of conventional tensile tests for reference purposes. The specimens were cut out from the sheets by laser at 0º, 45º and 90º degrees with respect to the rolling direction and the results are summarized in Table 1. Figure 6 presents the corresponding stress-strain curves up to the maximum value of strain corresponding to the occurrence of necking. As seen, the stress response of the material is not significantly influenced by anisotropy, which will not be taken into consideration in the following sections of the paper.

	Modulus of elasticity (GPa)	**Yield strength (MPa)**	**Ultimate tensile strength (MPa)**	**Elongation at break (%)**	**Anisotropy coefficient**
Aluminium EN AW 1050					
0º RD	64.3	33.6	70.7	31.1	0.74
45º RD	67.2	33.9	72.5	36.4	0.51
90º RD	70.4	34	69.9	32.6	0.62
Average	67.3	33.9	71.4	34.1	$\bar{r} = 0.60$ $\Delta r = 0.17$
Steel DC04					
0º RD	218	205.4	327.2	20.8	1.53
45º RD	238	216.6	338.6	19.3	1.07
90º RD	224	208.2	327.0	20.8	1.66
Average	229.5	211.7	332.9	20.0	$\bar{r} = 1.33$ $\Delta r = 0.53$

Table 1. Summary of the mechanical properties of aluminum EN AW-1050 and steel DC04 sheets with 3 mm thickness.

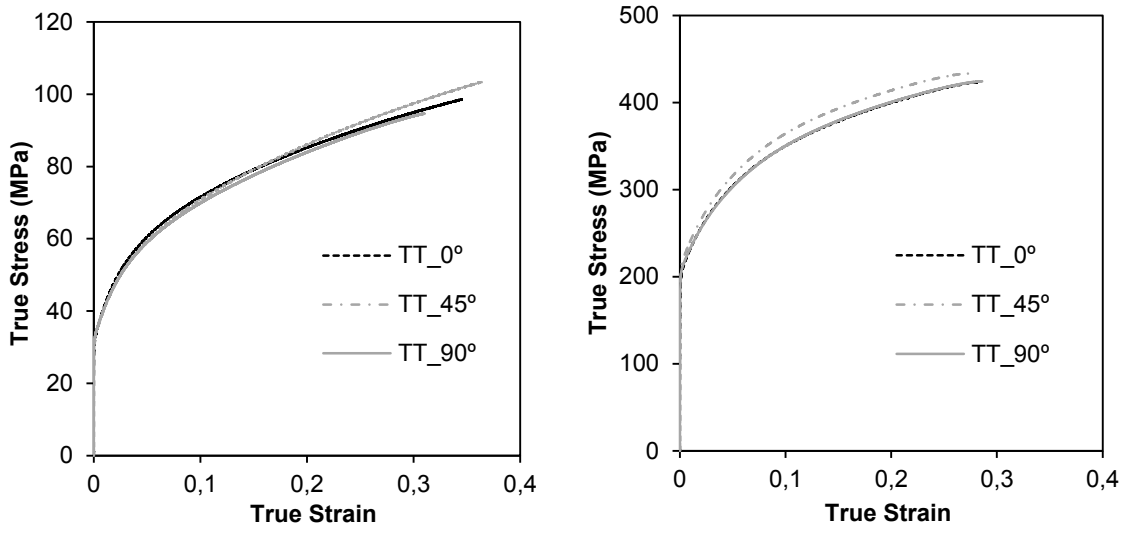

Figure 6 Stress-strain curves obtained from conventional tensile tests performed in specimens cut out from aluminium EN AW-1050 and steel DC04 sheets with 3 mm thickness.

3.2 Experimental work plan

The double-notched shear test specimens and the instability test specimens were cut out of the supplied sheets of aluminium EN AW-1050 and steel DC04 by laser. Both tests were performed at room temperature in the tooling apparatus that is schematically shown in Figure 2.

The influence of the loading direction within the plane of the sheets (transverse ‘T’ and longitudinal ‘L’) was not taken into consideration due to the absence of significant planar anisotropic Δr effects (Table 1). Table 2 presents a summary of the main geometrical features of the specimens and of their testing conditions.

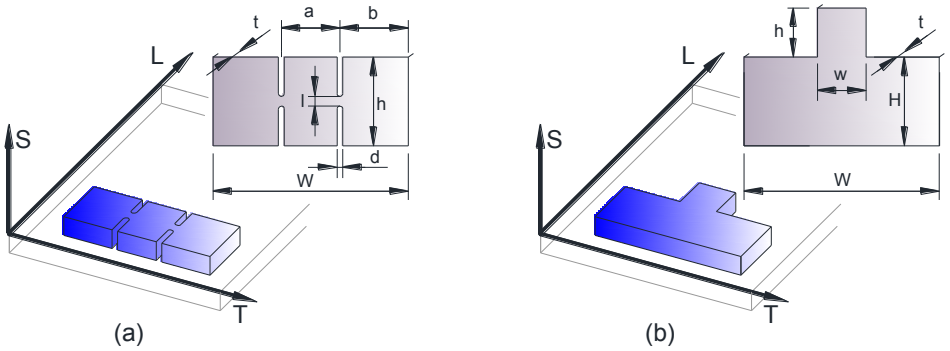

Double-notched shear test specimen							Instability test specimen			
l	d	a	b	h	w		h	H	w	W
2	2.5	27.5	33.75	50	100		10	120	10	75
4							15			
6							20			
8							25			
10							30			
All the tests were performed with a velocity equal to 60 mm/min										

Table 2 Summary of the geometry of the double-notched shear and instability test specimens. All dimensions in (mm).

4. RESULTS AND DISCUSSION

4.1 Stress-strain curve

The methodology for determining the stress-strain curve from double-notched shear tests is described in Section 2.1 and schematically outlined in Figure 3.

Figure 7 compares the stress strain curves of aluminum EN AW-1050 and steel DC04 obtained from double-notched shear tests with those took from conventional tensile tests (designated as ‘TT’). As seen in case of the aluminum EN AW-1050 (Figure7a) the results obtained from conventional tensile tests (TT) and from double-notched shear tests (DNST) are similar up to an effective strain value $\bar{\varepsilon} \cong 0.3$. This value is close to the maximum testing range of the conventional tensile test ($\bar{\varepsilon} \cong 0.35$, refer to the vertical dashed line) due to subsequent development of necking. Beyond this value of effective strain the stress response derived from the conventional tensile tests is extrapolated and, because of this, the solid black line is changed into a dashed black line. In contrast, the double-notched shear test is capable of determining the stress-strain curves of the materials up to values of effective strain $\bar{\varepsilon} \cong 1.5$, which corresponds to the amount of displacement when cracks are triggered. Besides the adequacy of the double-notched shear test to determine the stress-strain curve in the loading directions (‘T’ and ‘L’) perpendicular to the sheet thickness, it can also be concluded that the extrapolation of the stress response from tensile tests to values of effective strain above their maximum testing range may lead to deviations from the actual stress response of the material. In view of the above, it may be concluded that tensile tests are not recommended to determine the stress-strain curves of materials for SBMF applications because they are limited to small values of strain.

The poor agreement of the results obtained in the tests that were performed with the largest ligaments ($l = 10$ mm) is attributed to plastic work being also consumed outside

the two rectangular patches of the test specimens (refer to the detail in Figure 2). This causes the stress-state to deviate from pure plastic shearing conditions.

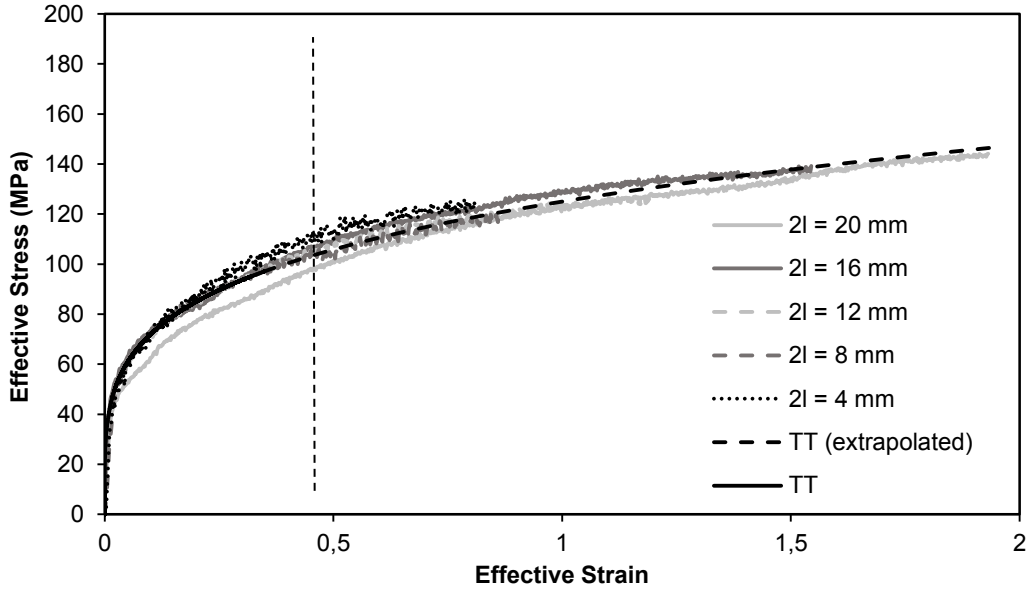

(a)

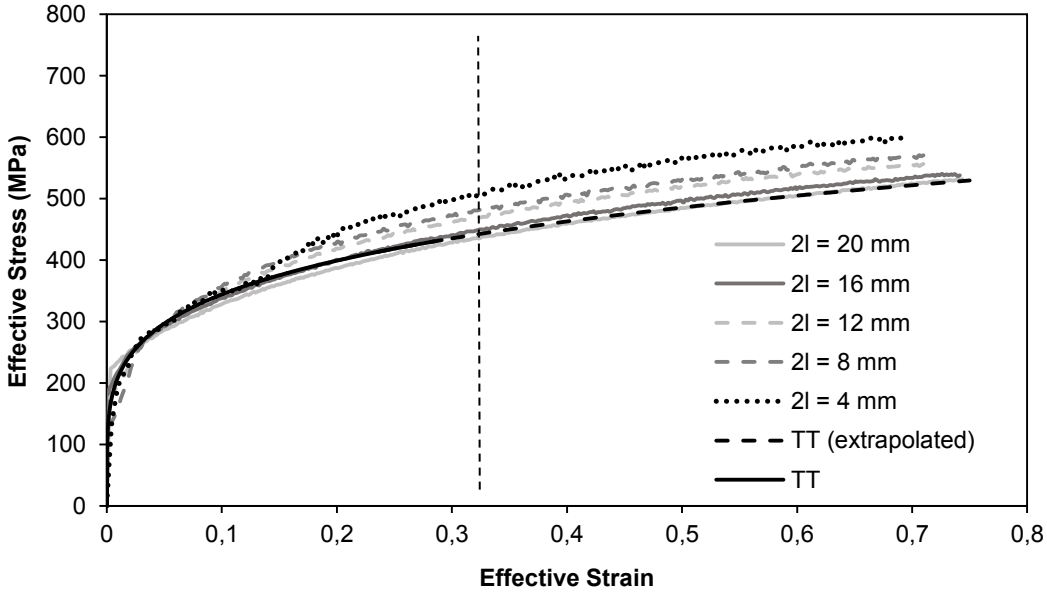

(b)

Figure 7 Stress-strain curves obtained from tensile tests (TT) and from double-notched shear tests with different ligament sizes $2l_i$ for (a) aluminium EN AW-1050 and (b) steel DC04 sheets with 3 mm thickness. The stress-strain curves obtained from tensile tests are extrapolated for values of effective strain placed to the right of the vertical dashed lines.

The results obtained for steel DC04 (Figure 7b) lead to similar conclusions and prove the feasibility of the double-notched shear test to be utilized with different types of engineering metals. In this case, the poor agreement of the results obtained in the tests performed with the smallest ligaments ($l = 2$ mm) is attributed to rotational effects of the inner part of the specimens that also causes the stress-state to deviate from pure plastic shearing conditions.

4.2 Fracture toughness

Figure 8 shows the experimental evolution of the force with displacement for the different double-notched shear test specimens that are listed in Table 2. As seen, the force-displacement evolution exhibits a gradual increase to a maximum peak value (where cracks are triggered) and a steep decrease from this peak value, which may change as a function of the size l of the ligaments.

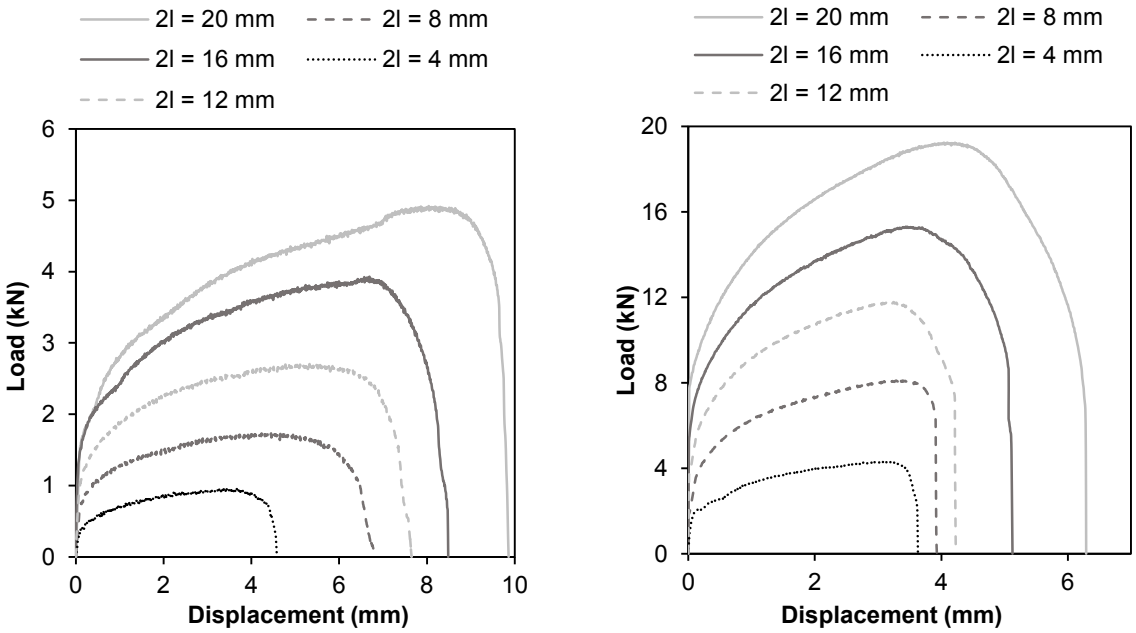

Figure 8 Experimental evolution of the force with displacement for double-notched shear test specimens with different ligaments $2l_i$ cut from (a) aluminium EN AW-1050 and (b) steel DC04 sheets with 3 mm thickness.

The methodology for determining fracture toughness R is comprehensively described in Section 2.2 and is schematically outlined in Figure 4. In general terms, the experimental results allow concluding that the variation of the normalized total work $w_T = W_T / 2tl$, obtained from the area under each curve of Figure 8, as a function of the two ligament lengths $2l$ of the specimens is adequately interpolated by means of a straight line, is in good agreement with equation (7) (refer to Figure 9). From the analysis of Figures 9a and 9b it is concluded that the fracture toughness of aluminum EN AW-1050 and steel DC04 are respectively equal to $R \cong 174$ kJ/m^2 $R \cong 557$ kJ/m^2.
To conclude, it is worth noticing that the results obtained for the smaller ligaments ($l = 2$ mm) were not utilized in the determination of fracture toughness of DC04 due to the previously mentioned rotational effects of the inner part of the specimens that cause the stress-state to deviate from pure plastic shearing conditions.

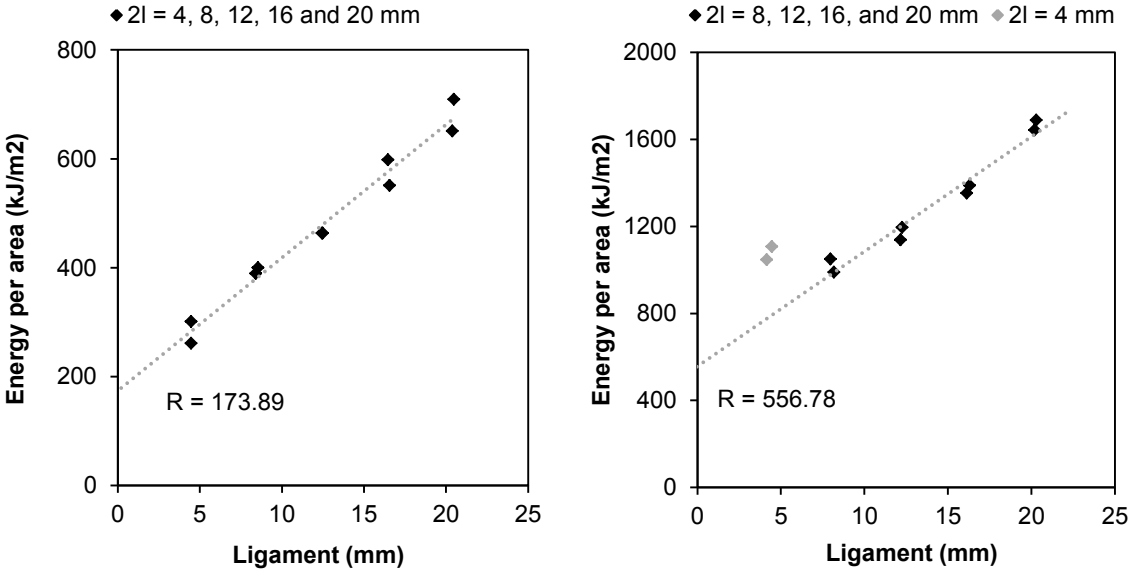

(a) (b)

Figure 9 Evolution of the normalized total work w_T with ligament length $2l_i$ for double-notched shear test specimens with different ligaments cut from (a) aluminium EN AW-1050 and (b) steel DC04 sheets with 3 mm thickness. Fracture toughness R is obtained from the y-intercepts of the straight lines.

4.3 Critical instability strength

Figure 10 shows the experimental evolution of the force with displacement for the rectangular test specimens loaded in compression that are included in Table 2. As seen, the evolution is characterized by two different patterns. The specimens with smaller heights ($h = 10$ mm) show a steep increase of the force-displacement evolution without occurrence of plastic instability and subsequent formation of out of plane buckling. In contrast, the remaining test specimens show an initial steep increase of the force with displacement up to the onset of plastic instability followed by a bifurcation into a secondary loading path during which the force increases at a lower rate.

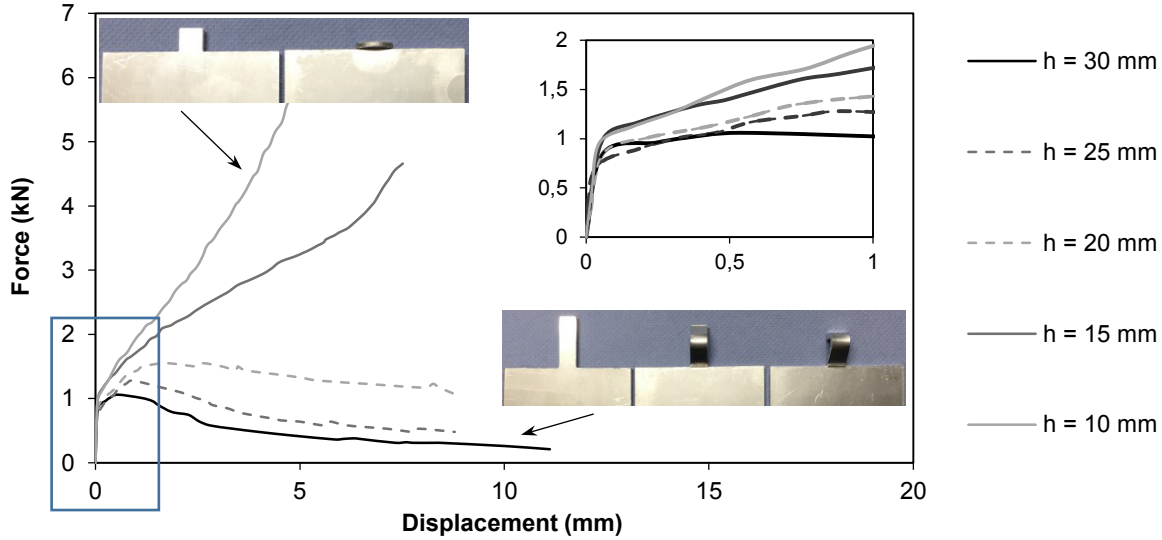

(a)

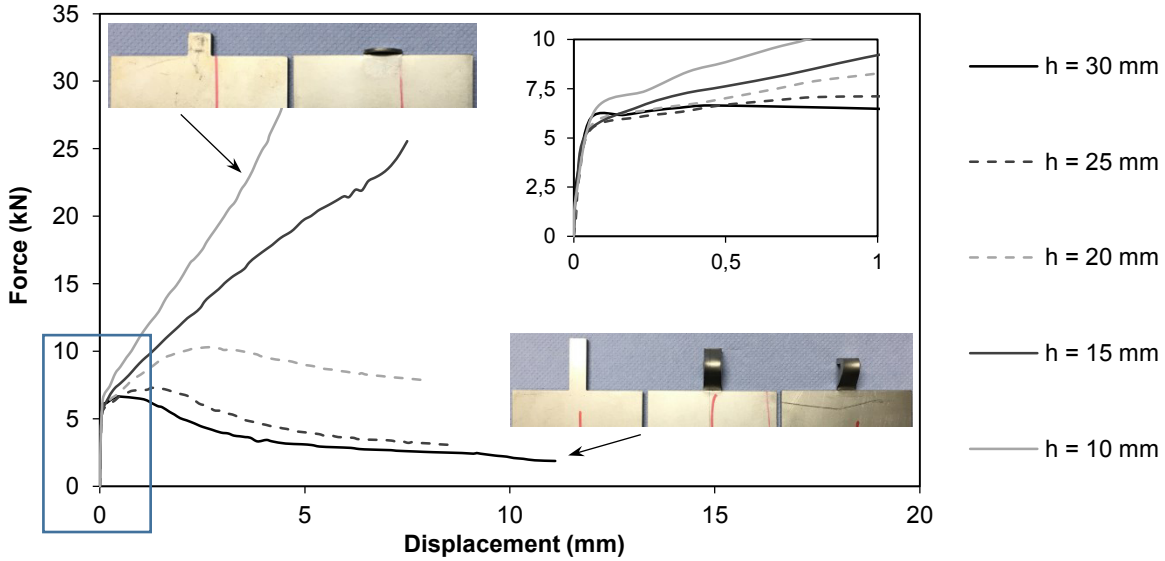

(b)

Figure 10 Experimental evolution of the force with displacement for rectangular test specimens loaded in compression with different heights h_i cut from (a) aluminium EN AW-1050 and (b) steel DC04 sheets with 3 mm thickness.

The deformation mode observed in the rectangular test specimens with smaller heights ($h = 10$ mm) is typical of SBMF because it gives rise to three-dimensional material flow outside the plane of the sheets (refer to the upward leftmost test specimens of the enclosed photographs).
The deformation modes corresponding to the remaining rectangular test specimens are typical of plastic instability and, therefore, are unsuitable for SBMF applications. However, it is worth noticing that rectangular test specimens, unlike columns that collapse after buckling, are able to carry loads beyond the instability point in a stable manner. In practical terms this means that the post-buckling strength of sheets can be substantially greater than their buckling strength.

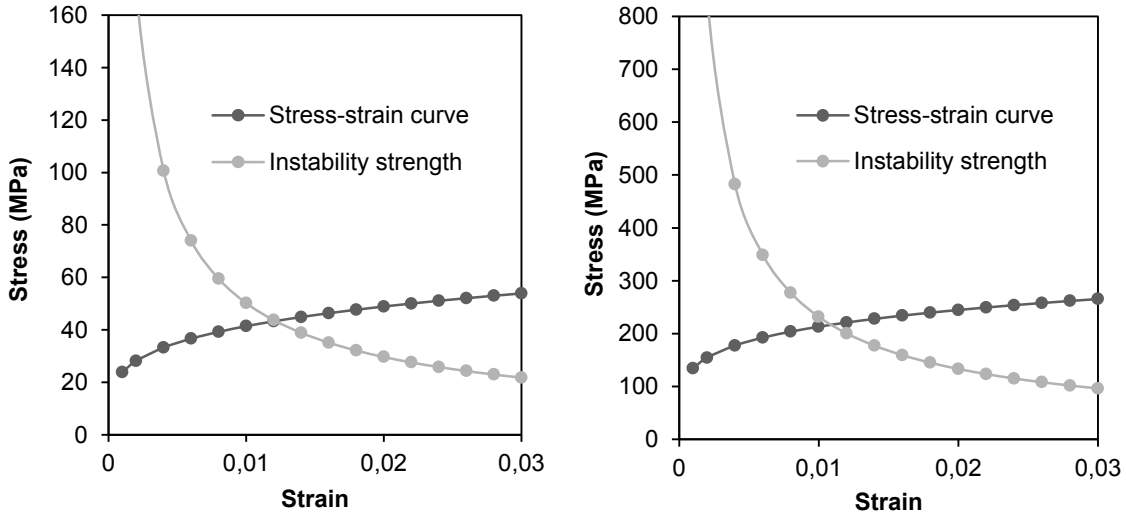

(a) (b)

Figure 11 Determination of the critical instability strength σ_{cr} for the rectangular test specimens loaded in compression cut from (a) aluminium EN AW-1050 and (b) steel DC04 sheets with a thickness to width ratio $t/w = 0.3$.

The application of the methodology for determining the critical instability strength that was described in Section 2.3 to the rectangular test specimens of EN AW-1050 and steel DC04 sheets with a thickness to width ratio $t/w = 0.3$ is disclosed in Figure 11.

As seen in the figure, the critical instability strengths σ_{cr} is obtained from the intersection of the material stress-strain curves $\sigma(\varepsilon)$ and the instability strengths $\sigma_{cr}(\varepsilon)$ given by equation (9) and provides values $\sigma_{cr} = 43$ MPa for the aluminium EN AW-1050 and $\sigma_{cr} = 217$ MPa for the steel DC04. The parameter K in equation (9) was taken as $K = 0.5$ in order to match the experimental values of force at the onset of plastic instability.

The above mentioned values of the critical instability strength σ_{cr} are valid for a thickness to width ratio $t/w = 0.3$ but the occurrence of plastic instability in the form of buckling out of the sheet plane depends on the slenderness ratio h/w of the specimens. In the tests performed by the authors it was observed that safe deformation modes without buckling require $h/w \leq 1$. This ratio is of great interest to the design of sheet metal parts produced by SBMF.

5. CONCLUSIONS

This paper introduces a methodology to determine the stress-strain curve, the fracture toughness and the critical instability strength of materials supplied in the form of sheets to be used in sheet-bulk metal forming (SBMF) processes. The stress-strain curve and fracture toughness are determined by means of a double-notched shear test whereas the critical instability strength is determined by means of the axial compression of rectangular sheet specimens with different support conditions along the height and width directions.

Experiments performed in aluminum EN AW-1050 and steel DC04 sheets with 3 mm thickness demonstrate that the double-notched shear test can be effectively utilized to determine the stress-strain curve up to higher strain levels than those attained in conventional tensile tests. The work performed in the axial compression of rectangular test specimens allows concluding that the critical instability strength is a function of the thickness to width ratio t/w of the specimens and can be obtained by combining experimental data with the analytical solution for the elasto-plastic stability of plates subjected to equal uniform compression on two opposite edges. However, the development of buckling out of the sheet plane is mainly influenced by the slenderness ratio h/w and it was concluded that it is necessary to ensure $h/w \leq 1$ to obtain a sound three-dimensional material flow without buckling.

ACKNOWLEDGMENTS

This work was supported by the German Research Foundation (DFG) within the scope of the Transregional Collaborative Research Centre on sheet-bulk metal forming (SFB/TR73) in the subproject A4 ‘Fundamental research and process development for the manufacturing of load-optimized parts by incremental forming of metal sheets’.

Carlos Silva and Paulo Martins would like to acknowledge the support provided by Fundação para a Ciência e a Tecnologia of Portugal and IDMEC under LAETA – UID/EMS/50022/2013 and PDTC/EMS-TEC/0626/2014.

REFERENCES

1. Merklein M, Allwood JM, Behrens BA, Brosius A, Hagenah H, Kuzman K, Mori K, Tekkaya AE, Weckenmann A. Bulk forming of sheet metal. *CIRP Annals Manufacturing Technology* 2012; 61: 725–745.
2. Salfeld V, Matthias T, Krimm R, Behrens BA. Analysis of machine influence on process stability in sheet bulk metal forming. *45th CIRP Conference on Manufacturing Systems, Athens, Greece, Procedia CIRP* 2012; 3: 32–36.
3. Silva CMA, Silva MB, Alves LM, Martins PAF. A new test for determining the mechanical and fracture behavior of materials in sheet-bulk metal forming. *Journal of Materials: Design and Applications* 2015 (on line first).
4. DOI: 10.1177/1464420715616140.
5. ASTM E8/E8M. *Standard Test Methods for Tension Testing of Metallic Materials*. ASTM International, West Conshohocken, USA, 2013.
6. ASTM B831. *Standard Test Method for Shear Testing of Thin Aluminum Alloy Products*, ASTM International, West Conshohocken, USA, 2014.
7. Atkins AG. Ductile shear fracture mechanics. *Key Engineering Materials* 2000; 177-180: 59-68.
8. Cotterell B, Reddel JK. The essential work of plane stress fracture. *International Journal of Fracture* 1977; 13: 267–277.
9. Isik K, Silva MB, Atkins AG, Tekkaya AE and Martins PAF. A new test for determining fracture toughness in plane stress in mode II. *Journal of Strain Analysis for Engineering Design* 2015; 50: 221-231.
10. Timoshenko SP, Gere JM. *Theory of Elastic Stability*. McGraw Hill, New York, 1961.

CONTROL STRATEGY OF TWIST SPRINGBACK FOR AN ASYMMETRIC THIN-WALLED TUBE SUBJECTED TO ROTARY DRAW BENDING

Xin Xue*, Juan Liao, Gabriela Vincze, António B. Pereira

Centre for Mechanical Technology and Automation, Department of Mechanical Engineering, University of Aveiro, 3810-193, Aveiro, Portugal

ABSTRACT: This paper aims to investigate the control strategy of twist springback of an asymmetric thin-walled tube after mandrel rotary draw bending, which is a complex nonlinear physical process with coupling multi-factor interactive effects. By using the improved finite element model [1], two process control strategies related to the mandrel nose placement and the axial push assistant loading are proposed for the efficient reduction of twist springback. The simulation results indicate that the mandrel nose placement mainly affect the springback but not twist deformation. The springback angle is firstly increased and then decreased after several forward tests. The other control strategy, additional axial push assistant loading, is possible to reduce twist deformation, but the risk of springback of bending angle and wrinkle in the intrados sidewall also rises.

INTRODUCTION

Aluminum alloy thin-walled tubes have the advantages of lightweight and a high bending rigidity, which make them suitable both for automotive structures with complex cross-sectional shape. As shown in Figure 1, the whole process of mandrel rotary draw bending (MRDB) comprises three steps: bending tube, retracting mandrel and springback. The mandrel with flexible cores is positioned inside the tube to provide the rigid support. Booster force improves material flow in the forming zone and leads to less thinning of the wall on the outside of the bend and less cross section distortion.

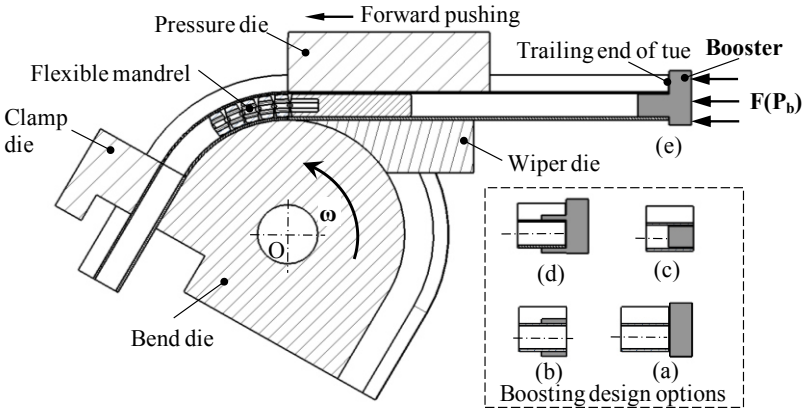

FIGURE 1. Sketch of mandrel rotary draw bending and its boosting design options for push assistant loading condition.

* Corresponding author: PhD candidate, contact email: xin@ua.pt

The undesirable twist springback phenomenon of asymmetric cross-sectional structures is inevitable due to unbalanced elastic-plastic deformation and residual stress release after the dies are removed, as shown in Figure 2. In practice, the efficient control of the twist springback is still treated by the know-how experience and "try and error" experiments [2]. Recently, the finite element method has become the principal tool for deep analysis of tube bending deformations. Many previous efforts have been conducted to improve the springback prediction [1, 3]. However, these works have paid less attention on control strategy of twist springback, which is vital in precision manufacturing. In this paper, by using the improved numerical model, two process control strategies related to the mandrel nose placement and the push assistant loading are assessed for the efficient reduction of twist springback.

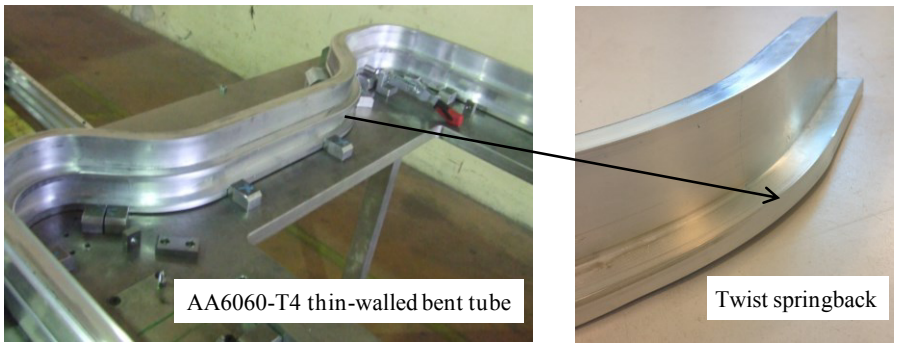

FIGURE 2. Twist springback characteristics of an asymmetric thin-walled tube after mandrel rotary draw bending

MODELING PROCEDURES

The studied material is AA6060-T4, which is widely used for the production of extruded thin-walled tubes in real applications. For an accurate numerical modeling, Yld2000-2d anisotropic yield criterion [4] integrated with combined isotropic and kinematic hardening model (IHKH) was used to describe the strain-stress behavior including anisotropy and Bauschinger effects [5]. The corresponding mechanical experiments, namely uniaxial tension and forward-reverse simple shear tests were performed to determine the material parameters. The basic mechanical behaviors and the corresponding material parameters are listed in Table 1.

TABLE 1 The basic mechanical behaviors and material parameters for AA6060-T4.

Basic mechanical behaviors	E (GPa)	ρ (kg/m^3)	υ	$\sigma_{0.2}$	σ_b				
	64	2700	0.33	99.6	243				
Yld2000-2d	α_1	α_2	α_3	α_4	α_5	α_6	α_7	α_8	α
	0.766	1.266	0.751	0.975	1.052	1.070	0.871	1.592	8
IHKH	σ_0 *(MPa)*	*Q (MPa)*	*b*	*C (MPa)*	γ				
	86.4	137.5	6.74	3221.2	59.6				

An improved FE model with surface-based coupling constraint for flexible mandrel using HINGE connector element has been developed and validated in the previous work [3], as illustrated in Figure 3a. The twist springback of the asymmetric thin-walled tube includes two

main codes of deformation behaviors. In the longitudinal direction, the amount of springback can be expressed as the value of springback angle

$$\Delta\theta = \theta - \theta' \quad (1)$$

where θ and θ' are the bending angles along the longitudinal direction before and after springback, respectively, as shown in Figure 3b.In the circumferential direction, the main twist springback angle of open section part can be given by

$$\varphi_f = \arctan\frac{\Delta(U_2)}{L_f} \quad (2)$$

where $\Delta(U_2)$ is the maximum displacement of open section part in the vertical direction (U_2), and L_f is the length of the fin.

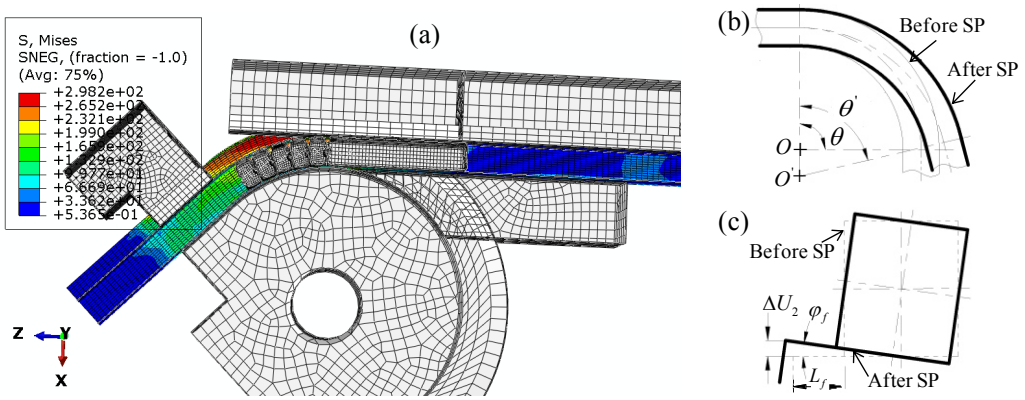

FIGURE 3. (a) Finite element model of mandrel rotary draw bending (b) longitudinal springback angle (b) twist angle.

RESULTS AND DISCUSSION

In MRDB, the tube wall will thicken along the inside radius (intrados) and will thin along the outside radius (extrados) as the clamps draw the tube around the bend die. The purpose of the mandrel nose is to cover this region of flowing material and ensure a consistently round crosssection by mitigating the simultaneous compression and stretching of the tube wall.As one solution, the mandrel in a too far forward position stretches the material on the outside of thebend more than necessary. This increases the length of material on the outside beyond what is required to make abend. Figure 4a is an exaggerated example. Bumps appear on the extrados of the bend and are most evident at the end of bend. Astep may begin to appear on the intrados at the start of the bend. On the other hand, the mandrel in a too far back forward does not adequately stretch the material on theoutside of the bend and generate enough pressure on the inside of thebend to compress the material. This may lead to form a wrinkle or wave on the intrados of the tube, as shown in Figure 4b. Therefore, the mandrel nose placement (MNP) relative to the point of bend or the line of tangency, as shown in Figure 4c,not only affects the stress and deformation state of the bent tube but also the degree of springback.

Several forward MNP were introduced into the FE model and tested the feasibility for the control of twist springback. The range of the MNP change is from 0 to 10mm. Figure 5 shows the comparison of the predicted twist springback by using different

MNP in the case of 45º bending thin-walled tube. It can observed that the springback angle is firstly slight increased and then decreased. This might be because the first increase of MNP aggravates the large deformations on the extrados side including the rate of elastic deformation, which leads to the larger springback. The further increase of MNP may mitigate the intrados compression deformation and then cause the decrease of springback. The MNP also makes an important effect on the ovalization or distortion of the close section. For the twist deformation in the flange, no remarkable difference was observed between the situations.

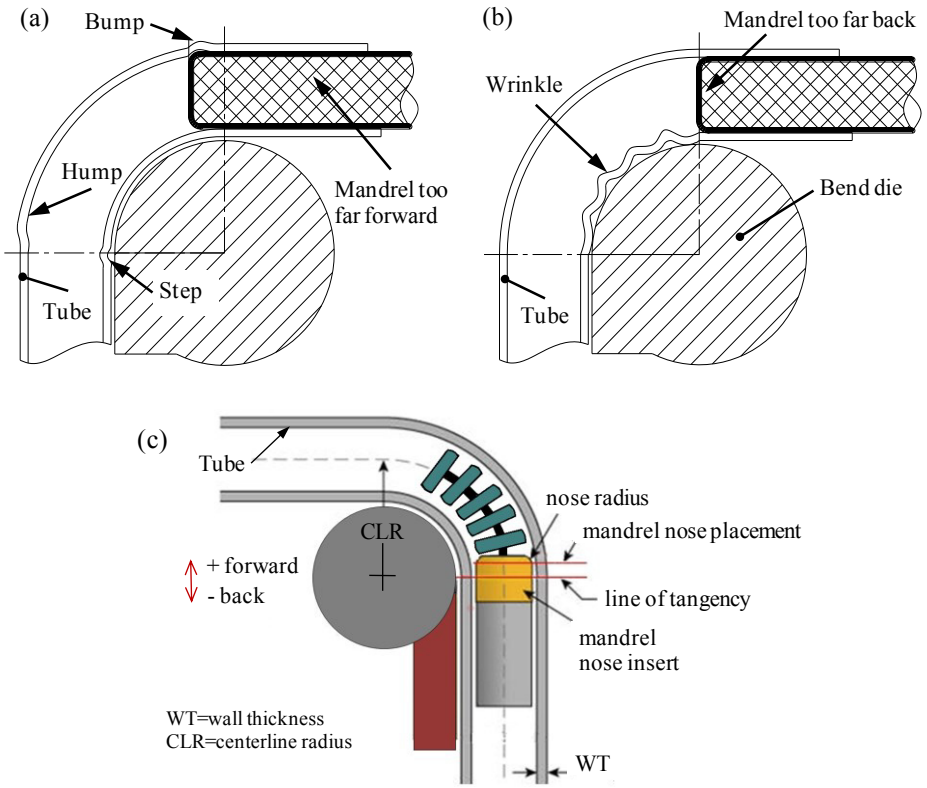

FIGURE 4. (a) The mandrel in a too far forward position (b) the mandrel in a too far back position (c) illustration of mandrel nose placement.

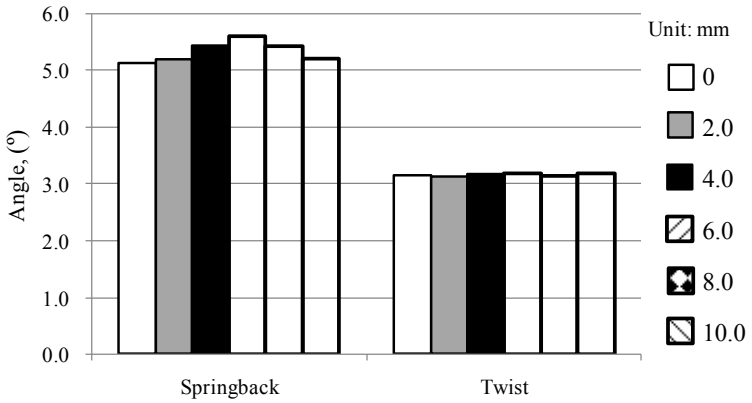

FIGURE 5. Comparison of twist springback calculated by using different MNP.

The booster, one of the movable pushing tools, can be used to apply the axial boosting force or push assistant loading (PAL) to thetrailing end of the tube to control the flow

state of tube materials. Figure 1 shows that there are five possible methods toapply the axial boosting force via booster:

1) To provide the push assistant force directly at the trailing end of tube;
2) To provide the push assistant force by the friction between booster and outer surface of tube;
3) To combine the above two boosting methods to exert the boosting force;
4) To provide the push assistant force by the friction between booster and inner surface of tube;
5) To combine the first method and the fourth one to boost the tube. To evaluate the efficiency of the boosting method on springback control of thin-walled tube, the last boosting method with respect to different boosting force conditions was adopted based on the developed FE model.

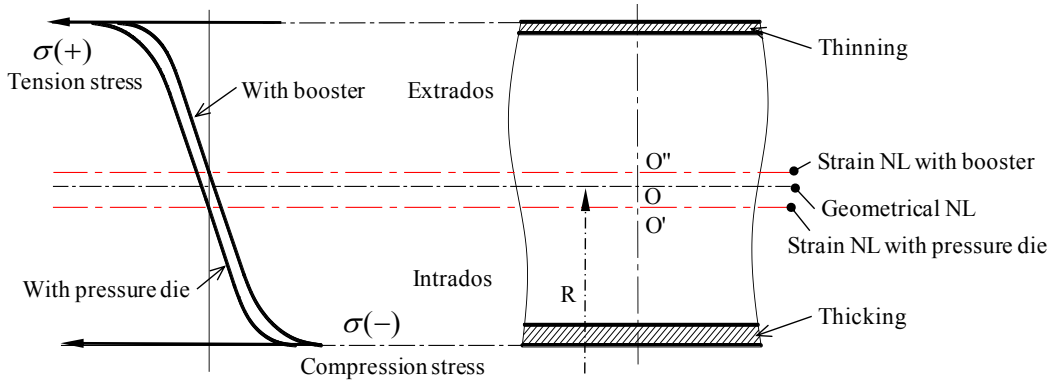

FIGURE 6. Stress distribution and strain neutral line change of the cross-section of bending tube under PAL conditions.

The PAL helps push the materials past the tangent point and intothe bending regions, which decreases the tensile stress and makesthe strain neutral line (NL) shift outwards, as shown in Figure 6. However, it might induce or aggravate thelocal wrinkling due to simultaneously induced excessive compressive stress at the intrados of tube. Thus it is necessary to study theinteractive effects of PAL conditions on different defects such aswrinkling, wall thinning and twist springback.

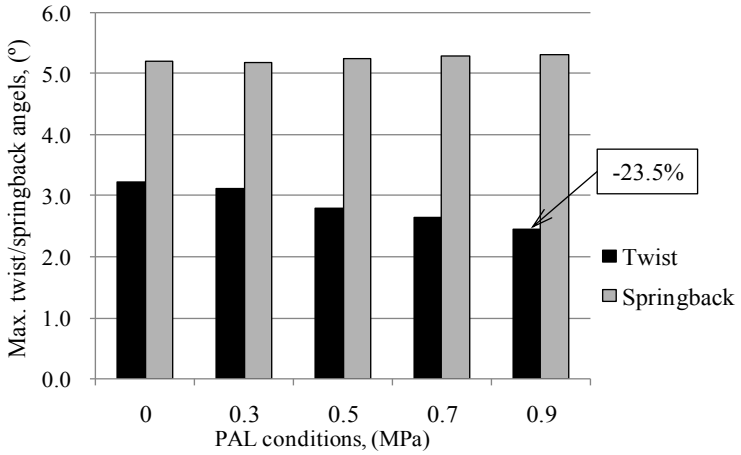

FIGURE 7. Comparison of twist springback calculated by different PAL conditions.

Four PAL conditions, 0.3MPa, 0.5MPa, 0.7MPa and 0.9MPa, were applied on the trailing end of the thin-walled tube during the MRDB. Figure 7 compares the maximum twisting and springback angles calculated by using different PAL conditions. It can be

observed that 23.5% degradation of twisting deformation can be achieved by 0.9MPa PAL condition compared to no PAL condition. However, the springback of bending angle makes almost no better and even a slight increase.

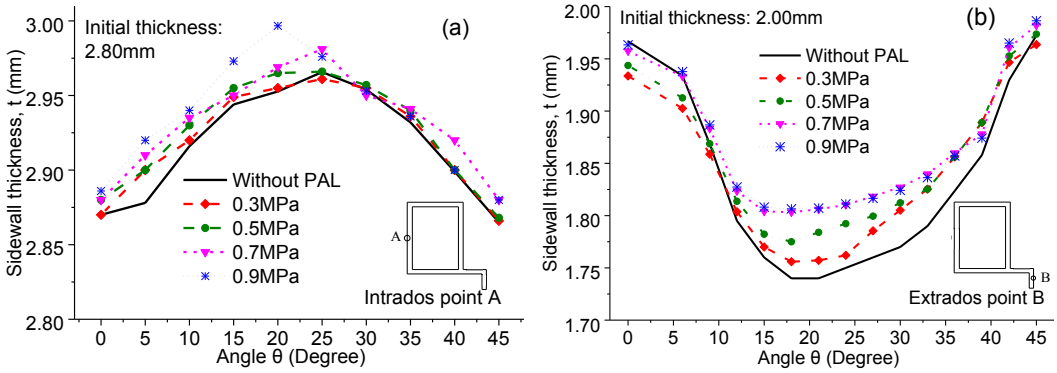

FIGURE 8. Comparison of the intrados and extrados sidewall thickness distributions calculated by using different PAL conditions.

Figure 8 shows that the selected intrados and extrados sidewall thickness distributions were calculated by using different PAL conditions. The thickness of intrados sidewall increases with the increase of push assistant pressure, while that of extrados sidewall decreases. This means that the extrados sidewall has less deformation, but the risk of the wrinkle in the intrados sidewall rises. Although the proposed PAL method seems not so high efficiency to reduce the twist deformation of the presented case, it provides an alternative method for the other possible industrial applications.

Acknowledgement: The supports from the Portugues Science Foundation (Ref. SFRH/BD/103010/2014) and the industrial project cooperated with Portuguese company CICLO-FAPRIL for optimization of forming conditions of the plastic deformation of aluminium alloyare greatly appreciated.

REFERENCES

[1] Xue X., Liao J., Vincze G., Gracio J. (2015) Modelling of mandrel rotary draw bending for accurate twist springback prediction of an asymmetric thin-walled tube. Journal of Materials Processing Technology 216:405-417.
[2] Li H., Yang H., Zhang Z.Y., Li G.J., Liu N., Welo T. (2014) Multiple instability-constrained tube bending limits. Journal of Materials Processing Technology 214: 445-455.
[3] Liao J., Xue X., Lee M. G., Barlat F., Gracio J. (2014) On twist springback prediction of asymmetric tube in rotary draw bending with different constitutive models. International Journal of Mechanical Sciences 89: 311-322.
[4] Barlat F., Brem J. C., Yoon J. W., Chung K., Dick R. E., Lege D. J., Pourboghrat F., Choi S.-H., Chu E. (2003) Plane stress yield function for aluminium alloy sheets—Part I: theory. International Journal of Plasticity 19:1297–1319.
[5] Chung K., Lee M.-G., Kim D., Kim C., Wenner M.L., Barlat F. (2005) Spring-back evaluation of automotive sheets based on isotropic–kinematic hardening laws and non-quadratic anisotropic yield functions. Part I: theory and formulation. International Journal of Plasticity 21: 861–882.

ASSESSMENT OF DIFFERENT DUCTILE DAMAGE MODELS AND EXPERIMENTAL VALIDATION

Rui Amaral[1*], Pedro Teixeira[2], Abel D. Santos[1,2], J. César de Sá[1,2]

[1]INEGI, Institute of Science and Innovation in Mechanical and Industrial Engineering, R. Dr. Roberto Frias, 400, 4200-465, Porto, Portugal
[2]FEUP, Faculty of Engineering, University of Porto, R. Dr. Roberto Frias, 4200-465, Porto, Portugal

ABSTRACT: For the constant goal in automotive industry to achieve a better fuel economy, lower costs and better properties, a new generation of materials are seeing their usage and implementation increased. However, this usage leads to difficulties in the prediction of material behaviour during the sheet metal forming processes, thus challenging the numerical simulation. This paper seeks to contribute in the prediction of fracture on sheet metal alloys. Three constitutive damage models are used, Lemaitre's, GTN and Johnson-Cook, to simulate, as realistically as possible, the mechanical behaviour of the sheet metal material. The corresponding parameters of damage models are identified using an inverse analysis procedure, based on experimental test data. Finally, to validate and verify the applicability of the studied damage models to predict the fracture, experiments are compared with FE simulations.

1. INTRODUCTION

The usage of numerical methods in sheet metal forming industry is continuously increasing, allowing the possibility to analyse larger and complex deformations that the sheet metal can be subjected during stamping or deep-drawing operations, including damage and fracture predictions.
Currently there is an emphasis on automobile industry related with weight reduction of automotive body, safety and vehicle fuel economy, due to the environmental emissions restrictions. To accomplish this goal, a new generation of materials are used. However, their lower formability in sheet forming operations, leading to premature fracture, is challenging the numerical simulation in prediction of such material behaviour [1].
In the present paper three damage models are used: Johnson-Cook model, Gurson-Tvergaard-Needleman (GTN) model and finally Lemaitre's ductile damage model. The Johnson-Cook and GTN models are already implemented in FE package Abaqus, but the corresponding damage parameters are obtained by an inverse analysis procedure using reference experimental tests. In case of Lemaitre damage model, a user material subroutine was developed and implemented in Abaqus/Explicit code [2], based on Lemaitre's local damage evolution.
Finite element simulations are presented and the corresponding results are compared with an experimental failure cylindrical cup component, in order to evaluate and validate the implemented damage models and their ability to predict damage growth and fracture initiation.

2. DAMAGE MODELS

2.1 Johnson-Cook model

The material degradation under plastic deformation can be expressed by damage indicators, due to their relative simplicity. Nevertheless, these models are often calculated using a fully uncoupled approach, meaning that the progressive degradation does not affect the yield surface of the material. The model proposed by Johnson and Cook [3] is one of these models, which, besides the postulation of a phenomenological strain rate and temperature dependent hardening law, has also defined the fracture strain ε_f as a function of stress triaxiality η, plastic strain rate $\dot{\varepsilon}_p$ and temperature θ as:

$$\varepsilon_f = (d_1 + d_2 e^{d_3 \eta}) \left[1 + d_4 ln\left(\frac{\dot{\varepsilon}_p}{\dot{\varepsilon}_0}\right)\right](1 + d_5 \theta) \tag{1}$$

where d_1, d_2, d_3, d_4 and d_5 are material parameters.

2.2 GTN Damage Model

Gurson [4] has proposed an internal variable to describe material degradation, which represents the volume fraction of micro-cavities that nucleate, grow and coalesce during loading. The original model was further extended by Tvergaard [5] and Needleman [6] replacing the original internal variable f by a modified parameter f^* in order to take into account the accelerated void coalescence process after a critical void volume fraction $f_c$is reached. The yield function of the GTN damage model is given by:

$$\phi = \left(\frac{\bar{\sigma}}{\sigma_Y}\right)^2 + 2q_1 f^* cosh\left(\frac{3}{2} q_2 \frac{\sigma_H}{\bar{\sigma}}\right) - \left(1 + q_3 f^{*2}\right) \tag{2}$$

where q_1, q_2 and q_3 are the model parameters, σ_Y the flow stress and σ_H and $\bar{\sigma}$ the hydrostatic stress and equivalent von Mises stress, respectively. The modified porosity parameter f^* is calculated by:

$$f^* = \begin{cases} f & f \le f_c \\ f_c + \dfrac{1/q_1 - f_c}{f_F - f_c}(f - f_c) & f > f_c \end{cases} \tag{3}$$

The evolution law of the void volume fraction is given by:

$$\dot{f} = \dot{f}_G + \dot{f}_N \tag{4}$$

accounting for void growth $\dot{f}_G$ and nucleation $\dot{f}_N$, both variables expressed by:

$$\begin{aligned} \dot{f}_G &= (1 - f) tr \dot{\boldsymbol{\varepsilon}}_{\boldsymbol{p}} \\ \dot{f}_N &= \frac{f_N}{S_N \sqrt{2\pi}} exp\left[-\frac{1}{2}\left(\frac{\bar{\varepsilon}_p - \varepsilon_N}{S_N}\right)^2\right] \dot{\varepsilon}_p \end{aligned} \tag{5}$$

where f_N, S_N and ε_N are material parameters and $\dot{\boldsymbol{\varepsilon}}_{\boldsymbol{p}}$ isthe plastic strain rate tensor.

2.3 Lemaitre Damage Model

Induced by large plastic flow, the internal deterioration of the material, which may lead to macroscopic collapse, accompanies the deformation process and therefore, although different in nature, the two dissipative processes influence each other and should, therefore, be coupled at the constitutive level. The model formulated by Lemaitre [7] defines the damage variable as the neat area of a unit surface cut by a given plane corrected for the presence of existing cracks and cavities. By assuming homogenous distribution of micro-voids and the hypothesis of strain equivalence, the effective stress tensor can be represented as:

$$\tilde{\boldsymbol{\sigma}} = \frac{\boldsymbol{\sigma}}{1-D} \tag{6}$$

where is $\boldsymbol{\sigma}$ the Cauchy stress tensor. The damage variable D can assume values between 0 (undamaged state) and 1 (rupture). The evolution law for the internal variables it can be written as:

$$\dot{D} = \frac{\dot{\gamma}}{1-D}\left(\frac{-Y}{S}\right)^{s} \tag{7}$$

where $\dot{\gamma}$ is the plastic consistency parameter and Y is damage energy release rate given by:

$$Y = -\frac{1}{2E(1-D)^2}[(1-\upsilon)\boldsymbol{\sigma}:\boldsymbol{\sigma} - \nu(tr\boldsymbol{\sigma})^2] \tag{8}$$

where E and υ are the Young's modulus and Poisson's ratio, respectively.

3. Material and damage parameters

3.1 Material characterization

In this paper, a mechanical characterization of the aluminium alloy AA5182-O, with 1 mm thickness, was performed [8]. Tensile tests of AA5182-O specimens were conducted for different angles according to the rolling direction. The corresponding flow curves are shown in Fig.1.

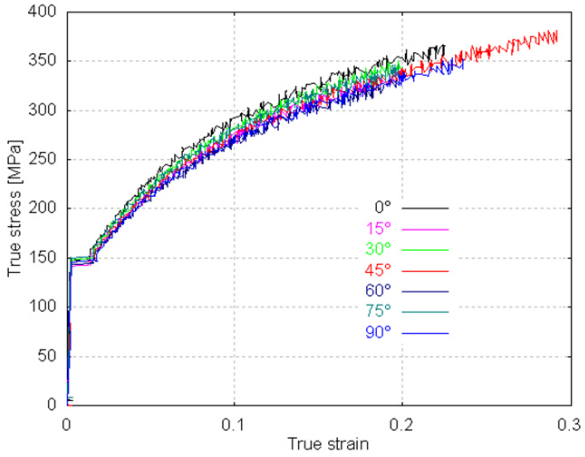

FIGURE 2. Flow stress-strain curve obtained from uniaxial tensile test for AA5182-O, according to different directions relative to the rolling direction [8].

TABLE 3 contains the mechanical properties of the studied material obtained from tensile tests, such as Young modulus (E), Poisson coefficient (v), yield stress (R_p), ultimate tensile strength (R_m) and total elongation (e_t), as well as the anisotropy coefficients (*r-value*) for different directions relative to rolling direction. In order to describe the hardening behaviour of the AA5182-O, the Voce Law was used. The corresponding parameters are presented also in TABLE 3.

TABLE 3. Mechanical properties for the aluminium alloy AA5182-O.

Property	Value	Voce Law	
Young modulus [GPa]	69	$Y = Y_0 + R_{sat}\left[1 - \exp\left(-C_r \cdot \bar{\varepsilon}^{p}\right)\right]$	
Poisson coefficient	0.3		
Yield stress [MPa]	149.5		
Ultimate tensile strength [MPa]	283.8	Y0 [MPa]	149
Total elongation [%]	24.4	Rsat [MPa]	208.7
r_0, r_{45}, r_{90}	0.79, 0.85, 0.7	Cr	12.1

3.2 Identification of damage model parameter

An inverse numerical analysis, based on optimization algorithms, was used to obtain the parameters of the studied damage models. The minimization of the mean square error (MSE) between experimental and numerical data is calculated using an optimization algorithm implemented on MATLAB. The result of the iterative procedure gives the best fit values for the presented damage models. For the Johnson-Cook damage model, strain rate and temperature effects were not considered, corresponding to parameters d_4 and d_5, respectively. Since this model accumulates failure, in which the failure strain is more dependent to stress triaxiality than the others variables, it is more important the determination of parameters d_1, d_2 and d_3 [9]. To characterize the behaviour of the material using the GTN damage model, it is necessary the determination of 7 parameters, but there is a mutual dependency that must be considered [10]. According to literature, the parameters q_1, q_2 and S_N are kept constant [11]. Lemaitre damage model parameters has been identified by Teixeira *et al* [1]. The obtained parameters for all the damage models are presented in table 4**Error! Reference source not found.**.

TABLE 4. Implemented damage models parameters for AA5182-O.

Johnson-Cook damage model									
Parameter	d_1		d_2			d_3		d_4, d_5	
Value	0.024		0.38			1.5		0	
GTN damage model									
Parameter	q_1	q_2	q_3	f_0	f_C	f_F	ε_N	S_N	f_N
Value	1.5	1	2.25	0.01	0.021	0.04	0.3	0.1	0.001
Lemaitre damage model									
Parameter	Damage exponent - s			Damage denominator –S			Damage closure effect		
Value	1.0			1.25 [MPa]			0.2		

4. Results and discussion

4.1 Deep drawing cylindrical cup tool geometry

In order to evaluate the applicability of the described damage models, an experimental deep drawing cylindrical cup test is considered. The geometries and dimensions of cylindrical cup tools are given in Fig.2. Successful stampings are obtained for a blank diameter of 119 mm with high amount of lubricant, corresponding to the drawing ratio limit. However, for poor lubrication conditions failure occurs for a cup height of 17.7 mm, as shown in Fig.2b.

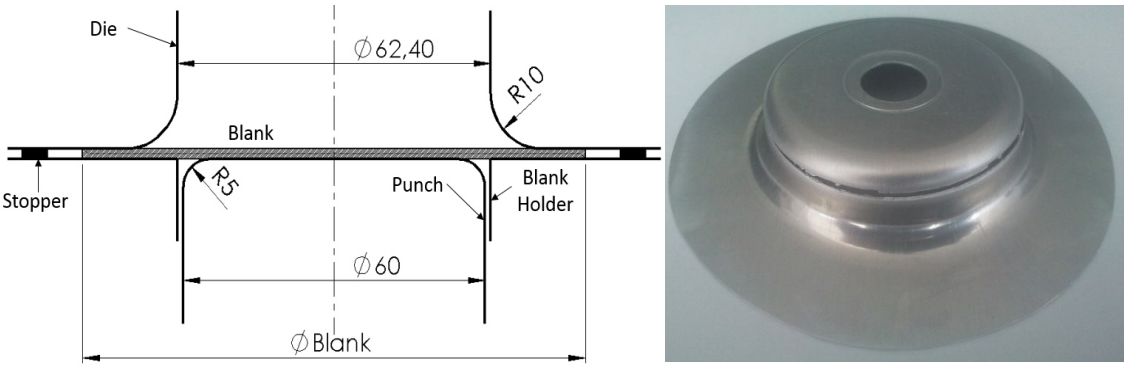

FIGURE 3. a) Tool geometry and active parts; b) Cylindrical cup component with breakage.

The blank has a hole that allows an efficient centering in tool. The punch geometry includes a drawbead in top section (Fig.2a), in order to clamp the circular sample, thus preventing the hole to increase its radius during drawing. A stopper is used to limit the blank holder movement in the end of drawing, in order to avoid some defects. The stopper is a ring produced with the same sheet material and thickness of the blank used.

4.2 Finite element model

A 3D FEM explicit analysis (Abaqus/Explicit) full model is considered with a constant friction coefficient of 0.2. The tools are modeled as fully rigid surfaces with discretization performed by three noded rigid elements. The blank discretization uses a double layer of deformable eight noded solid elements with reduced integration, making a total of 1600 elements. Regarding the material behaviour, the blank was modeled as an elasto-plastic material with hardening described by Voce Law, already presented in section 3. The GTN and Johnson-Cook models are implemented in FE package Abaqus, but in the case of Lemaitre model a user material subroutine was used.

4.3 Results

Fig.4 presents the contours of the equivalent plastic strain and the damage value for the three considered damage models, respectively, Johnson-Cook, GTN and Lemaitre.

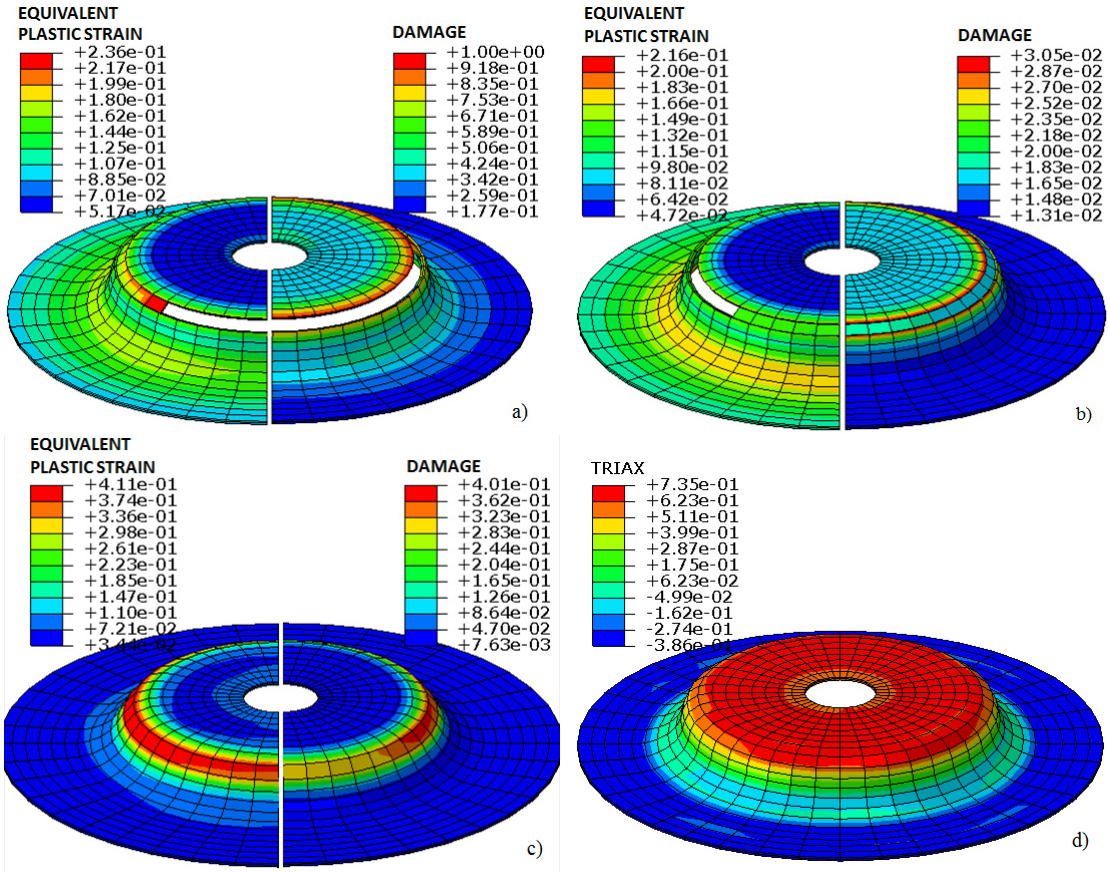

FIGURE 4.Obtained results from simulation of cylindrical cup; a) Johnson-Cook model; b) GTN model; c) Lemaitre model; d) stress triaxiality levels before failure.

Fig.4 shows the fracture initiation for the damage models presented in this study. For current proposed experimental component, both maximum strain and damage variable

have very close locations, near the punch radius. All damage models in this study show similar trend, which is in accordance with experimental evidence.
However, the punch displacement to failure and maximum strain are different. For the Johnson-Cook the obtained punch displacement was 17.71 mm and for GTN and Lemaitre model 17.47 mm and 16.48mm, respectively, meaning that the corresponding damage parameters for Johnson-Cook and GTN are more adjusted to predict failure in this component.
Although Johnson-Cook and GTN models predict fracture initiation at the similar punch displacement, Lemaitre predicts failure at lower punch displacement. This difference can be attributed to some pathological mesh dependence of the fully coupled Lemaitre implementation due to strain softening.

5 Conclusions

Three different ductile damage models, Johnson-Cook, GTN and Lemaitre were implemented and compared in this paper, to predict the damage in sheet metal forming operations. A FE analysis of a cylindrical cup component, using the parameters obtained for the aluminum alloy AA5182-O, has been taken as a basis of comparison between the damage models, in order to assess the accuracy of the results. For this particularly case, the simulations of Johnson-Cook and GTN show a good agreement with the damage location and punch displacement observed in the experimental component. Lemaitre damage model overestimate the development of damage and a mesh dependence study will be developed.

Acknowledgement: Author(s) gratefully acknowledge the funding of SciTech - Science and Technology for Competitive and Sustainable Industries, R&D project cofinanced by ProgramaOperacional Regional do Norte ("NORTE2020"), through Fundo Europeu de Desenvolvimento Regional (FEDER) and the financial support of the Portuguese Foundation for Science and Technology (FCT) under project PTDC/EMS-TEC/6400/2014.

REFERENCES

1. P. Teixeira, A.D. Santos, J.M.A. César de Sá, F.M. Andrade Pires, A. Barata da Rocha. Int. J. Mat. Form., 2, 463-466, (2009)
2. P. Teixeira, A.D. Santos, F.M. Andrade Pires, J. César de Sá. J. Mat. Proc. Tech., **177**, 278-281, (2006)
3. G. R. Johnson, W. H. Cook. Eng. Fract. Mech., **21**, 31-48, (1985)
4. L. Gurson. J. Eng. Mat. Tech., 99, 2–15, (1977)
5. V. Tvergaard V. Int. J. Fract, 18, 237-252, (1982)
6. Needleman, V. Tvergaard. Acta metall., **32**, 157-169, (1984)
7. J. Lemaitre. J. Eng. Mat. Tech, 107, 83-89, (1985)
8. 3DS report, 2001. Selection and identification of elastoplastic models for the materials used in the benchmarks. 18-Months Progress Report, Inter-regional IMS contract ‘‘Digital Die Design Systems (3DS)’’, IMS 1999 000051
9. Marzbanrad, S. Noruzi, A. Ahmado, S.K. ISME2013, (2013).
10. D.A. Wang, W.Y. Chien, K.C. Liao, S.C. Tang, Ch. J. Mech Series A **19**, 161-168, (2003)
11. Z.L. Zang, Fatig. Fract. Eng. Mat. Struct 19, 561-570, (1996)

THE ROLE OF CHROMIUM CARBIDES VOLUME FRACTION ON PLASTIC INSTABILITY UNDER THREE-POINT BENDING TEST IN MARTENSITIC STAINLESS STEEL

Alvise Miotti Bettanini[a], Laurent Delannay[a], Pascal J. Jacques[a], Thomas Pardoen[a], Guillaume Badinier[b], Jean-Denis Mithieux[b]

[a]Institute of Mechanics, Materials and Civil Engineering, Universite catholique de Louvain, B-1348 Louvain-la-Neuve, Belgium

[b]Aperam Research Center, BP 15, 62230 Isbergues, France

ABSTRACT: Martensitic stainless steels (MSS) are valid candidates for automotive applications as they present a good combination of mechanical and functional properties which improves the safety and efficiency of new vehicles. However, these steels show limited fracture strain under three-point bending conditions. The fracture strain is controlled by the evolution of ductile damage as the material is plastically deformed, which in turn is influenced by microstructural features such phase ratio and carbides distribution. In this work, a modified AISI 410 MSS is heat treated in order to change the carbides distribution by dissolving part of the Cr-rich carbides while keeping the same phase ratio of ferrite and martensite. Each sample is tested under three-point bending and uniaxial tensile loading. The importance of the carbides distribution parameters (volume fraction, interparticle distance and size) on the crack propagation mechanism is assessed in order to link the material ductility to the critical microstructure constituents.

INTRODUCTION: In the recent years, automotive industry is facing an urgent demand to meet several constrains in term of gas emission, weight and safety of car vehicles. European Union is setting challenging targets in order to reduce the impact of the transportation system on the overall greenhouse emission levels [1]. These regulations drive the continuous research effort towards more efficient engines and lighter vehicles capable to meet these standards. One effective way to produce lighter vehicles is to increase the strength of the materials used in the frame, which allows to meet safety standards with a significant decrease in the overall mass. One example of the last generation of Advanced High Strength Steel (AHSS) are martensitic stainless steels. MSS present a good combination of tensile strength, fracture toughness, corrosion resistance and high quenching ability, which simplifies the forming operations. However these steels show limited fracture strain in some cases, for instance under three-point bending loading. The ductility is controlled by the evolution of ductile damage as the material is plastically deformed, the initiation and propagation of damage being strongly influenced by the microstructure. Understanding the link between microstructures and properties is therefore one of the priorities of the current research effort. Chromium carbides ($Cr_{23}C_6$) are very common precipitate in martensitic stainless steel due to the high driving force of precipitation of these compounds [2]. This type of carbide are detrimental in two ways: they deplete Cr from the martensitic matrix which decreases the overall corrosion resistance of the steel and second, they act as source of damage during plastic deformation [3].

PROCEDURES, RESULTS AND DISCUSSION:

A modified AISI 410/EN1.4006 stainless steel was cast and hot rolled down to 3mm thick at Aperam Stainless Steel Europe facilities. The steel is then batch annealed and cold rolled to 1.5 mm thick sheets before the final annealing below A1 temperature. The chemical composition of this material is listed in table 1. Samples are taken from the 1.5 thick sheet and heat treated into the austenite region in a Nabertherm LH 216/14S furnace preheated at the desired austenisation temperature before final quenching with blowing air. In the untreated form, about 1vol% of $Cr_{23}C_6$ carbides are dispersed in a ferrite matrix. The carbides size ranges between 0.5 µm to 1.5µm and are found to be detrimental for the mechanical and functional properties of the material. Therefore the material can be heat treated in order to dissolve part of the $Cr_{23}C_6$ carbides initially present in the structure [4]. Mechanical characterisation was performed with both uniaxial tensile test according to NF EN ISO 6892 standard and 3-point bending test according to VDA 238-100 procedure.

TABLE 1 Chemical composition of the Nb-modified AISI 410 martensitic stainless steel.

	C	*Mn*	*Si*	*Ni*	*Cr*	*N*	*Nb*
Wt%	0,1	0,3	0,4	0,1	12,0	0,02	0,1

Both mechanical tests show that a reduction of carbide volume fraction corresponds to a decrease of the ductility in both uniaxial tension and bending loading conditions. These results are somewhat unexpected since the $Cr_{23}C_6$ carbides are the primary sites of void nucleation during the ductile damage accumulation due to their relative big size and low coherency with the matrix which generate void via particle decohesion [5]. This finding suggests that other damage mechanisms contribute to the failure process.

The damage mechanism is further investigated with scanning electron microscopy (SEM). Figure 1 shows one of fracture surface of the sample heat treated at 900°C for 15 minutes after failure in bending. The dimples on the surface are elongated parables, which suggests high shear stresses [6]. Figure 2 shows a crack that initiates from the outer surface of one of the bent plates. The crack is tilted about 45° from the material surface and is propagating in a visible shear band in the material, which is highlighted by the distortion of the ferrite grains (darker in the back-scattering SEM image). Similar plastic localisation regions are found in the case of uniaxial tensile test loading.

Plastic instability and formation of shear bands are promoted by heterogeneities in the microstructure [7] like mechanical contrast between phases and second population of carbides which contribute to the damage accumulation. Both these possible sources of instability are found in the material, but here we limit our explanation to the mechanical contrast between ferrite and martensite phases. Mechanical contrast is defined here as the ratio of the yield stresses of the two phases, which is controlled by the relative chemical composition, carbon being the most efficient strengthening element in the martensite phase [2]. The average carbon content in martensite for different volume fraction of $Cr_{23}C_6$ carbides was calculated with Thermo-Calc (TC) software [8]. TC calculations shows that the dissolving carbides enrich martensite phase in carbon, thus increasing the mechanical contrast between martensite and ferrite that triggers the plastic instability sooner in the deformation process as found in previous works on high strength steels [9,10]. Table 2 summarises the effect of the heat treatments on the mechanical properties of the steel. The volume fraction of carbides, the calculated carbon content in martensite, the uniaxial tensile fracture strain and the bending angle

(bending line parallel to the transverse direction) for each of the three heat treatments are reported.

TABLE 2 Influence of heat treatment on carbide volume fraction and linked mechanical properties. Thermodynamic calculations are performed with TCFE6 database on Thermo-Calc v2015b.

Heat treatment	Carbide volume fraction (%)	Carbon in austenite (wt%)	True strain at fracture (tensile)	Bending angle (°)
860°C,60min	0.46	0.080	0.65	91
900°C,15min	0.32	0.090	0.60	83
975°C,5min	0.14	0.095	0.57	70

The effect of Cr23C6 carbides volume fraction on the mechanical properties of aNb-modified AISI410 SS was investigated under two different loading conditions. The results can be summarised as follow:

- Reduction in carbides volume fraction does not improve the mechanical properties under any loading condition.
- The damage mechanism is controlled by plastic instability in shear bands, which are relatively independent of ductile damage accumulation at the Cr23C6 carbides.
- The mechanical contrast between ferrite and martensite is the major cause of plastic instability.
- Dissolution of Cr23C6 carbides enriches martensite in carbon, which enhances the mechanical contrast and promotes plastic instability.

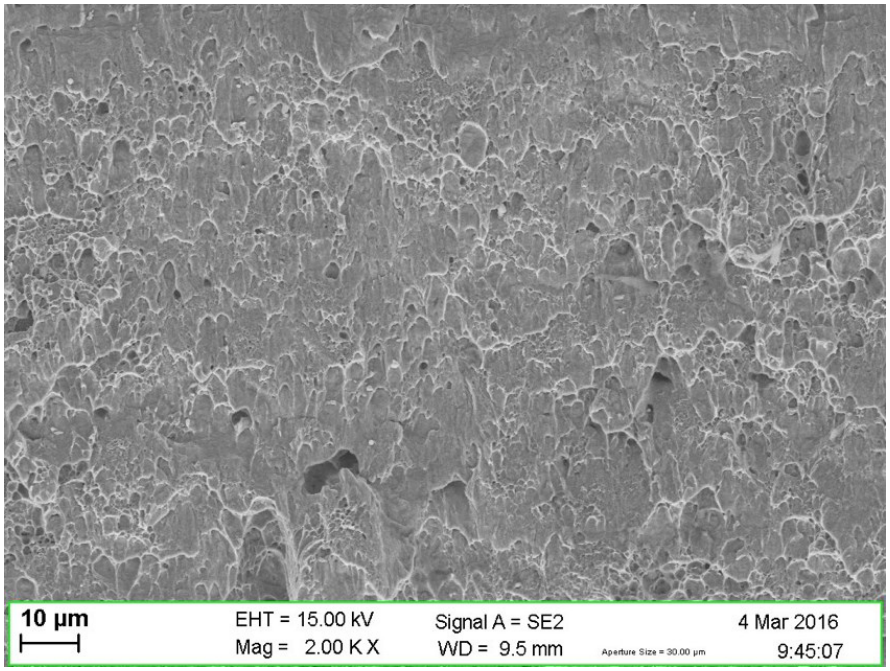

FIGURE 1. Fracture surface after failure in bending, the elongate parabolic dimples suggest a high shear component of the stress.

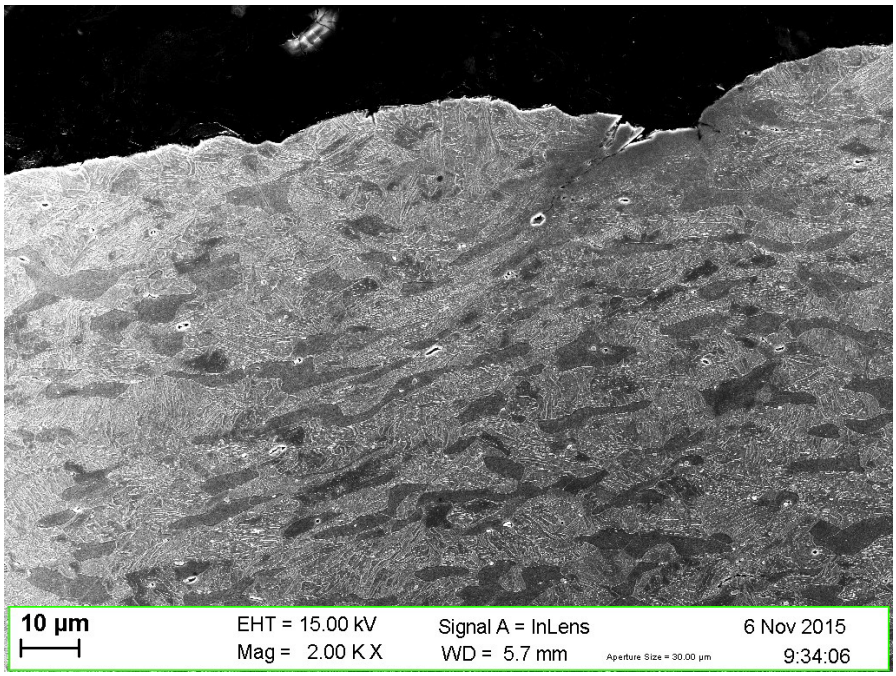

FIGURE 2. Section of one of the samples after bending which shows a shear band (in the center of the image) and a crack that initiates at the outer surface. The ferrite grains, which are darker in the image, allow to easily identify the shear band.

REFERENCES

[1] European Commision. Regulation (EU)No 333/2014 of the European Parliament and of the Council of 11 March 2014 amending Regulation (EC) No 443/2009 to define the modalities for reaching the 2020 target to reduce CO2 emissions from new passenger cars. 2014.

[2] Bhadeshia H. Steels microstructure and properties. Amsterdam. Elsevier, Butterworth-Heinemann; 2006.

[3] Kou S. Welding Metallurgy. Wiley-Interscience; 2003.

[4] de Andrés CG, Caruana G, Alvarez LF. Control of M 23 C 6 carbides in 0.45 C–13Cr martensitic stainless steel by means of three representative heat treatment parameters. Materials Science and Engineering A 1998;241:211–5.

[5] Landron C, Bouaziz O, Maire E, Adrien J. Characterization and modeling of void nucleation by interface decohesion in dual phase steels. ScriptaMaterialia 2010;63:973–6.

[6] Pineau A, Benzerga AA, Pardoen T. Failure of Metals I – Brittle and Ductile Fracture. ActaMaterialia 2016;107:424–483.

[7] Pardoen T, Pineau A. Failure of Metals. Comprehensive Structural Integrity, Volumes 1-10, vol. 2, 2003, pp. 686–783.

[8] Andersson JO, Helander T, Höglund L, Shi P, Sundman B. Thermo-Calc& DICTRA, computational tools for materials science. CALPHAD: Computer Coupling of Phase Diagrams and Thermochemistry 2002;26:273–312.

[9] Kaijalainen AJ, Suikkanen PP, Karjalainen LP, Porter DA. Influence of subsurface microstructure on the bendability of ultrahigh-strength strip steel. Materials Science & Engineering A 2016;654:151–60.

[10] Rèche D, Sturel T, Bouaziz O, Col A, Gourgues-Lorenzon AF. Damage development in low alloy TRIP-aided steels during air-bending. Materials Science & Engineering A 2011;528:5241–50.

MODELLING THE SELECTIVE LASER MELTING PROCESS AT THE SCALES OF THE POWDER AND THE PART

Pierre-Yves DURAND[1, 2*], Marion GIRARD[1], Baptiste GIRAULT[1], Bruno COURANT[1]

[1]Institut de Recherche en Génie Civil et Mécanique (UMR CNRS 6183), Université de Nantes, Saint Nazaire, France
[2]CERO, Parc d'activités des Ecobuts, Challans, France

ABSTRACT: Additive manufacturing processes have a great industrial potential through the production of high added value parts. Selective Laser Melting (SLM) is one of them in which the part is built layer by layer thanks to the melting of metallic powder beds with a laser source. A key point to control the process is a better insight of the related physical phenomena that can be achieved through modelling and simulation.

This work presents a two scales modelling. The first scale is the powder one and is used to model the melting of powder bed and its resulting track. The second scale is the part one. The part building is modeled to predict the process-induced temperature fields or/and resulting residual stress.

INTRODUCTION: Additive manufacturing consists in building a part layer by layer as opposed to the subtractive manufacturing as turning, milling or cutting. The current term gathers a family of seven processes according to the ASTM definition [1]. One of them, the Selective Laser Melting (SLM) rests on powder bed melting with a laser source. The SLM process includes a variety of physical effects (metallurgical, thermal, mechanical and fluid mechanics aspects) with important disparities in temporal and spatial scales. Two relevant modelling scales can be considered: the powder and the part scales.

At the powder scale, several models have already been proposed in literature. A 2D model has been developed by Attar and al. [2] with Lattice Boltzmann method for an Electron Beam Melting process, extended in 3D model by Ammer and al. [3] and after by Markl and al. [4] where numerical process windows were created in order to classify different areas with porous, swelling or without defect samples. In the case of SLM, the finite volume method is used by Qui and al. [5] to describe the splashing of molten material during the process. N'Dri and al. [6] used it to quantify the accuracy of the melt pool shape predictions. Khairallah and al. [7] have developed a code based on finite volume method to model the formation of pores and denudation zones during the interaction between laser and powder. With a Volume Of Fluid (VOF) model, Gürtler and al. [8] were the first to show more realism 3D simulation of melting and solidification in tracks. The powder size distribution and the effect of packing density has been investigated by Lee and Zhang [9].

At the part scale, the finite element method is generally used. An element birth and death model [10], [11] is introduced to simulate the powder melting and to determinate residual stresses, thermal cycle and final deformation of the part [12].
This paper introduces the powder scale modelling and briefly the part modelling. The main purpose is to create two models which can exchange information, feeding one another, developed with the commercial code Abaqus®, particulary suitable for mechanical properties investigations at the part scale. The first stage is to develop all the major physical effects, and implement them in each corresponding model. The main challenge lies in the implementation of multi physical phenomena in a mechanic-dedicated code. Several cases shows the opportunity to create modelling of this kind.

NUMERICAL METHOD: At the powder scale, multiple physical phenomena (thermal, metallurgical, mechanical, fluid-mechanical) are coupled and complexify the modelisation. In order to consider only the main physical effects, namely surface tension forces and the interaction between laser and material, must be simulated. On the one hand, surface tension effect is dominant to determine the shape of the resultant track, although the modelling of surface tension forces is computationally difficult since it requires the evaluation of surface curvatures. On the other hand, the interaction between laser and material greatly contributes to the temperature fields. Simulations are performed using the commercial code Abaqus® with the VOF method. The following section describes the governing equations for this model.

The advection equation for the i phase with its f_i volume fraction is solved:

$$\frac{\partial f_i}{\partial t} + \vec{V}.\nabla f_i = 0 \quad (1)$$

where $\vec{V}$ is the flow velocity. A single momentum equation is solved throughout the domain and the resulting velocity field is shared among the phases:

$$\rho\left(\frac{\partial \vec{V}}{\partial t} + \vec{V}.\nabla\vec{V}\right) = -\nabla p + \nabla\left[\mu\left(\nabla\vec{V} + \nabla\vec{V}^T\right)\right] + \rho\vec{g} + \overrightarrow{F_{sv}} \quad (2)$$

where ρ is the density and μ the dynamic viscosity of the fluid, p the pression, $\vec{g}$ the gravitational acceleration. The continuum surface force model of Brackbill [13] describes the term $\overrightarrow{F_{sv}}$ as the surface tension force per unit volume:

$$\overrightarrow{F_{sv}} = \sigma\kappa\vec{n}\delta_s \quad (3)$$

where σ is the surface tension, κ the local curvature, $\vec{n}$ the inner normal to the interface and δ_s is a function distinguishing the interface between two fluids. The inner normal is unknown and calculated with a central difference algorithm. In the 2D case, the normal $\overrightarrow{n_x}$ of the approximate interface in (i,j)th cell is given by:

$$\overrightarrow{n_x} = \frac{1}{2}\sum_{k=-1}^{1} f_{i+1,j+k} - f_{i-1,j+k} \quad (4)$$

where $f_{i+1,j+k}$ is the volume fraction in the $(i+1, j+k)$th cell. The local curvature κ of the interface is determinated with height functions method [14] : consider a uniform mesh of size Δ. In 2D, (x, y) coordinates, a 7x3 stencil around the interface cell $(i,j)$is constructed, and summing volume fractions along the x direction:

$$h_i = \sum_{m=i-3}^{m=i+3} f_{i,j}\Delta \quad (5)$$

The curvature equation comes as:

$$\kappa = \frac{h_{xx}}{(1+h_x)^{3/2}} \quad (6)$$

where h_x and h_{xx} are discretized using second-order central differences algorithm. The energy equation is also shared among the phases:

$$\frac{\partial}{\partial t}(\rho E) + \nabla\left[\vec{V}(\rho E) + \rho\right] = \nabla(k\nabla T) + S \quad (7)$$

The laser beam is generally modeled as a gaussian surface heat flux related to the TEM_{00} mode in laser [15]. Nevertheless, Gusarov and Kruth [16] assume volumetric heat source instead of surface heat flux. The multiple scattering of the laser ray supports the choice of a volume desposition of the energy in accordance with King and al. [17]. Assuming that heat radiation and convection losses are overlooked, the thermal boundary condition at the interface between powder and air is given by [18]:

$$-k\left(\frac{\partial T}{\partial t}\right) = Q = \frac{9.A.P}{\pi(1-e^{-3})(z_e-z_i)\left(r_e^2+r_e r_i+r_i^2\right)} exp\left(\frac{3r^2}{r_c^2}\right) \quad (8)$$

$$\text{where} r_c = r_i + (r_e - r_i)\frac{z-z_i}{z_e-z_i} \quad (9)$$

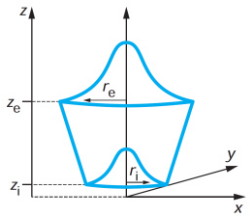

FIGURE 1. Representation of the volumetric heat source [19].

where Q is the volumetric heat source model for the laser beam, A the absorptance, P the laser power, k the thermal conductivity, z_i and z_e the top and bottom heights of the volumetric heat flux, r_i and r_e the top and bottom radius in figure 1.
In order to generate a random packing density of powder, we use a rain model with spherical particules. The particule size distribution of the experimental powder bed can be fitted with either uniform, gaussian, log-normal or Weibull distribution. Figure 2 presents two random powder beds generated with uniform or gaussian distribution.

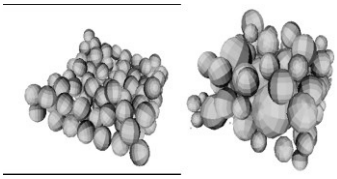

FIGURE 2. Random generated powder bed with uniform (left) or gaussian distribution (right).

RESULTS: Three case tests are presented to illustrate the reliability of our methodology.
The first assessment is performed through the coalescence between two droplets. The shape, and the behavior during the droplet formation is consistent with experimental study [20]. The merged droplet on figure 3 shows damped oscillations along two orthogonal axes due to the progressive transformation of the kinetic energy.

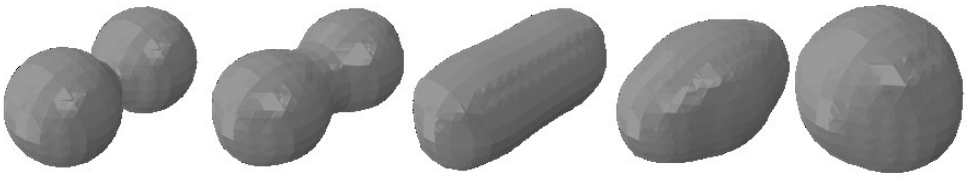

FIGURE 3. Coalescence of two droplets.

The second case test is to determine the shape for a melting powder on a substrate. Surface tension-driven flow is the major physical phenomena to explain the formation of the track during the selective laser melting. Figure 4 shows the shape of the droplet at different time steps.

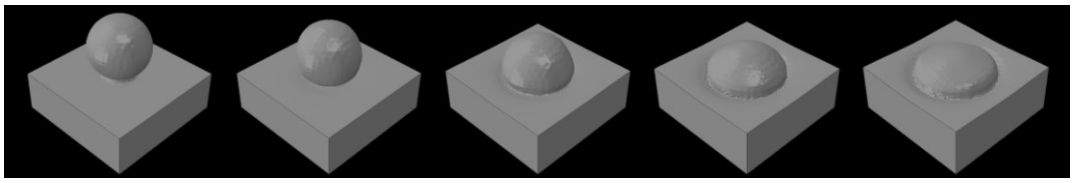

FIGURE 4.A melt powder on a substrate.

The last case test is the simulation of the powder bed coalescence in figure 5. The different particles merge together to create melted pool. These results illustrate the implementation of the surface tension forces in the commercial code Abaqus®.

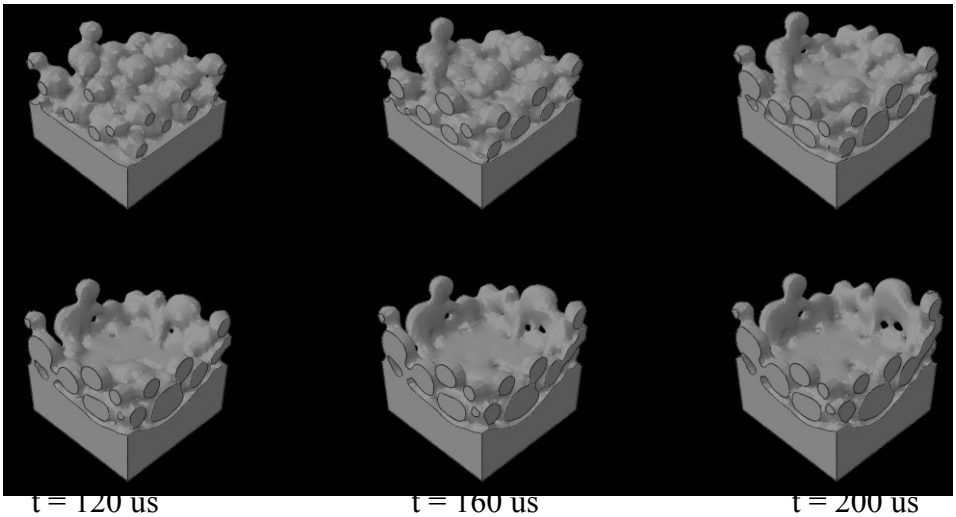

FIGURE 5.A melted powder bed at different time steps.

DISCUSSION: The powder model is useful to master the physical phenomena involved in the process and to predict the laser track geometry from the process parameters. This is a key point to build a part without porosity and a suitable surface state. It can suggest a process windows enabling bulk material in resulting track with an

appropriate geometry. The main drawback of such a complete modelling is the important need of CPU time (thousands of processor-hours), so it can not be used at the part scale.
A second model is developed at this scale using the Finit Element Method and the element birth and death technic. Its scope is to predict the temperature field induced in the building part and the residual stresses. Figure 6 presents the simulation at the part scale. Different subroutines have been developped to simulate the laser beam and the fabricated part with the element birth method.

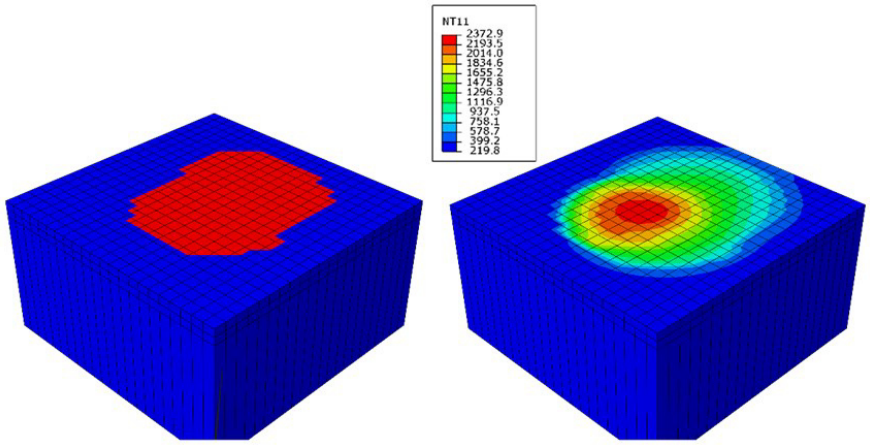

FIGURE 6. Part model: On the left figure, material properties in powder state in blue, and in bulk state in red. On the right figure, temperature fields on top surface during manufacturing.

These two models have to exchange information between each other. As a first step, the calculated temperature fields in the part model will be introduce in the powder model to take into account the underlayer temperature influence on the buiding track.

CONCLUSION: The commercial code Abaqus® has been chosen to develop a SLM process simulation because it is the software reference into mechanic field. In return, an important work has been necessary to implement the surface tension. The two scales modeling in developpement will enable to improve simulation accuracies.

Acknowledgement: The authors acknowledge the support of the MOULINNOV project and his partners.

REFERENCES

[1] Standard, A.S.T.M. F2792–12a (2012). Standard terminology for additive manufacturing technologies, vol. 10.
[2] Attar, E. (2011). Simulation of selective electron beam melting processes.Dr.-Ing., University of Erlangen, Nuremberg, Germany.
[3] Ammer, R., Rüde, U., Markl, M., Jüchter, V., and Körner, C. (2014). Validation experiments for LBM simulations of electron beam melting. International Journal of Modern Physics C, 25(12), 1441009.
[4] Markl, M., Ammer, R., Rüde, U., and Körner, C. (2015). Numerical investigations on hatching process strategies for powder-bed-based additive manufacturing using an electron beam. The International Journal of Advanced Manufacturing Technology, 78(1-4): 239-247.
[5] Qiu, C., Panwisawas, C., Ward, M., Basoalto, H. C., Brooks, J. W., and Attallah, M. M. (2015). On the role of melt flow into the surface structure and porosity development during selective laser melting.ActaMaterialia, 96: 72-79.

[6] N'Dri, N., Mindt, H. W., Shula, B., Megahed, M., Peralta, A., Kantzos, P., and Neumann, J. DMLS Process Modelling & Validation. TMS2015 Supplemental Proceedings: 389-396.
[7] Khairallah, S. A., Anderson, A. T., Rubenchik, A., and King, W. E. (2016). Laser powder-bed fusion additive manufacturing: Physics of complex melt flow and formation mechanisms of pores, spatter, and denudation zones. ActaMaterialia, 108: 36-45.
[8] Gürtler, F. J., Karg, M., Leitz, K. H., and Schmidt, M. (2013). Simulation of laser beam melting of steel powders using the three-dimensional volume of fluid method. Physics Procedia, 41: 881-886.
[9] Lee, Y. S., and Zhang, W. (2015) Mesoscopic Simulation of Heat Transfer and Fluid Flow in Laser Powder Bed Additive Manufacturing.International Solid Free Form Fabrication Symposium: 1154-1165.
[10] Longuet, A., Colin, C., Peyre, P., Quilici, S., &Cailletaud, G. (2006). Modélisation de la fabrication directe de pièces par projection laser: application au Ti-6Al-4V. In Matériaux 2006, Dijon, France, (pp. 11-p). xx.
[11] Li, C., Fu, C. H., Guo, Y. B., and Fang, F. Z. (2015). Fast Prediction and Validation of Part Distortion in Selective Laser Melting. Procedia Manufacturing (1), 355-365.
[12] Megahed, M., Mindt, H. W., N'Dri, N., Duan, H., and Desmaison, O. (2016). Metal additive-manufacturing process and residual stress modeling. Integrating Materials and Manufacturing Innovation 5 (1): 1.
[13] Brackbill, J. U., Kothe, D. B., and Zemach, C. (1992). A continuum method for modeling surface tension. Journal of computational physics 100 (2): 335-354.
[14] Afkhami, S., and Bussmann, M. (2009). Height functions for applying contact angles to 3D VOF simulations. International journal for numerical methods in fluids, 61(8): 827-847.
[15] Dai, D., and Gu, D. (2015). Tailoring surface quality through mass and momentum transfer modeling using a volume of fluid method in selective laser melting of TiC/AlSi10Mg powder. International Journal of Machine Tools and Manufacture 88: 95-107.
[16] Gusarov, A. V., and Kruth, J. P. (2005). Modelling of radiation transfer in metallic powders at laser treatment. International Journal of Heat and Mass Transfer 48 (16): 3423-3434.
[17] King, W. E., Anderson, A. T., Ferencz, R. M., Hodge, N. E., Kamath, C., Khairallah, S. A., and Rubenchik, A. M. (2015). Laser powder bed fusion additive manufacturing of metals. Applied Physics Reviews 2 (4).
[18] Zain-ul-Abdein, M., Nelias, D., Jullien, J. F., and Deloison, D. (2009). Prediction of laser beam welding-induced distortions and residual stresses by numerical simulation for aeronautic application.Journal of MaterialsProcessingTechnology 209 (6): 2907-2917.
[19] Bergheau, J. M. (2004). Modélisation numérique des procédés de soudage. Techniques de l'ingénieur. Génie mécanique, (BM7758).
[20] Accardo, A., Mecarini, F., Leoncini, M., Brandi, F., Di Cola, E., Burghammer, M., andDiFabrizio, E. (2013). Fast, active droplet interaction: coalescence and reactive mixing controlled by electrowetting on a superhydrophobic surface. Lab on a Chip, 13(3): 332-335.

NUMERICAL INVESTIGATION OF AN ARC INLET STRUCTURE EXTRUSION DIE FOR LARGE HOLLOW SECTION

Pan Jian-Yi *

School of Mechanical and Automotive Engineering, Guangzhou College of South China University of Technology, Guangzhou, China, 510800

ABSTRACT: This paper aims to improve the working life of extrusion die by optimal structure design, which plays an important role in the mass production. First, an arc shape inlet die structure for an aluminum large hollow section profile was developed. Second, three-dimensional finite element model of porthole extrusion process was established by using an Arbitrary Lagrangian-Eulerian method. Third, the comparison of the formability including the diversity of extrusion force and uniformity properties between the proposed design and two traditional design schemes under the same forming process configuration was analyzed and discussed. The results indicate that the novel structure design of the arc inlet die has a longer working life than the others.

INTRODUCTION: In order to meet the demand of lightweight construction for automotive and transport industries, aluminum extrusion which is a near-net-shape-forming technology has been widely adopted, especially for large hollow sections. However, challenges arising from the non-linear material behaviors, severe elasto-plastic deformation, and geometrical complexity are to control the forming quality and improve the tool life. Compared with the dies for regular profiles, large elastic deformation, deflection and even plastic deformation are prone to occur in the dies for heavy profiles. Therefore, heavy profile dies need further consideration and detail validation.

Heavy profile with large hollow structure is a typical extrusion benchmark, and some application cases are illustrated in Fig. 1(a). A mandrel die for a square tube are shown in Fig. 1(b).As shown in Fig. 1(c), the hatched areas A and B at the upper surface of the die contact with the billet (mostly cylindrical shapes).The billet is pressed into the portholes during the extrusion process. These surface areas directly endure the extrusion load from the billet because they are normal to the extrusion direction. Thereafter, the high pressed load of the mandrel and the resisting effect are required with the larger the area A. This means that the die working condition could be worse.

In the past two decades, several numerical modeling techniques and methods have been applied to the analysis of material flow during the extrusion process. Finite element method (FEM) is considered as one of the most widely used methods in extrusion process simulation analysis [1][2]. In recent years, finite volume method (FVM), e.g., Wu [3], and Chen et al[4], and Arbitrary Lagrangian-Eulerian method (ALE), e.g., van de Langkruis et al[5] and Lof[6], have been introduced to analyze the extrusion process.

Liu and Xie [7] presented that heavy profile could be defined by section area or overall dimension of the profile. In other words, the profile can be seen as heavy profile if one

*Corresponding author:Pan Jian-Yi
Postal address:No.1, Xuefu Road, Huadu District, Guangzhou, China
Phone: +86-13602416724 ; Fax:020-36903401; Email address: jianyi52@sohu.com

or more of three rules were satisfied as follows: (a)The width or circumcircle diameter is longer than 250mm.(b)The section area is larger than 2000mm^2.(c)The length of delivery is longer than 10m.

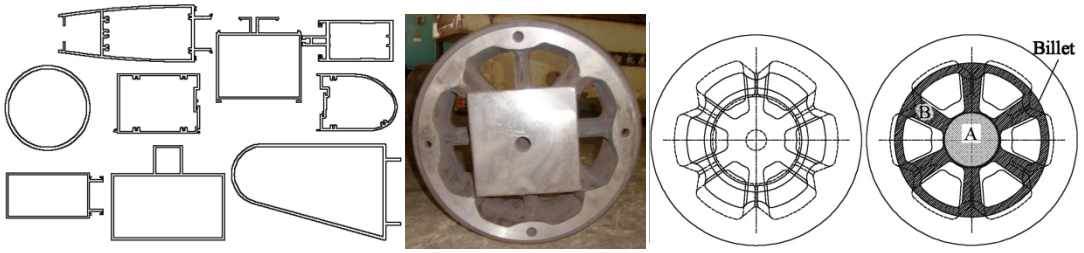

(a) (b) (c)

FIGURE 1. Heavy profiles with large hollow structure and die structure:
(a) Some samples of heavy profiles with large hollow structure (b)A mandrel die for a square tube (d) Die structure of large hollow section profile.

The objective of this study is to optimize the extrusion die design with large hollow sections by using numerical and experimental methods. An arc inlet structure for large hollow section extrusion die is developed. Compared with two other traditional design schemes by numerical analysis, the extrusion force, exit velocity and stress load are analyzed and discussed.

MODEL DESCRIPTION:

The geometry of the section is presented in Fig. 2(a). The key design structures including portholes, bridges distribution and the welding room shape of the dies are shown in Fig. 2(b). In order to avoid the welding planes occurring on major decorative surfaces, the die design with the four portholes structure has been developed as well as the four corresponding bridges, which are located at four corners of the section. Six convexities are set near the outlet of the screws places of the section respectively to increase the metal supply to fill the screw holes. Fig. 2(c) illustrates the distribution of the bearing length.

Fig. 2(d) is the regular design assembly script. To reduce the pressure for the mandrel die, scheme 2 is a common way to alleviate loads, as shown in Fig. 2(e). In this method, the most of material is split from the inlet of the mandrel to the preformed alloy, which forms a room to let aluminum pre-form before entering the portholes. This might lead to reduce the deformation resistance. However, the strength and the stiffness of the mandrel would be weakened due to the reduction of the mandrel bridge thickness.

Fig. 2(f) is a novel structure design idea for large hollow section dies. In this scheme, a sphere surface is set to guide the metal flow into die cavity. The normal direction surfaces at the die inlet which block the metal flow vertically are changed to spherical shape. Theoretically, these modifications could let the metal flow into die cavities much easier.

In order to further investigate how the arc shape inlet structure works, three different schemes, including two common die design schemes and an arc shape inlet structure design scheme, are compared in the following discussions.

In an attempt to simulate the three-dimensional extrusion process for various extrusion ratios and complicated profiles model, an ALE method finite element code, HyperXtrude, was employed for the comparison of these three design schemes. Simulating control parameters are the same as author's another literature[8].Fig. 2(d)(e)(f)(g) show the finite element model of the mandrels and the extrusion models of three different schemes.

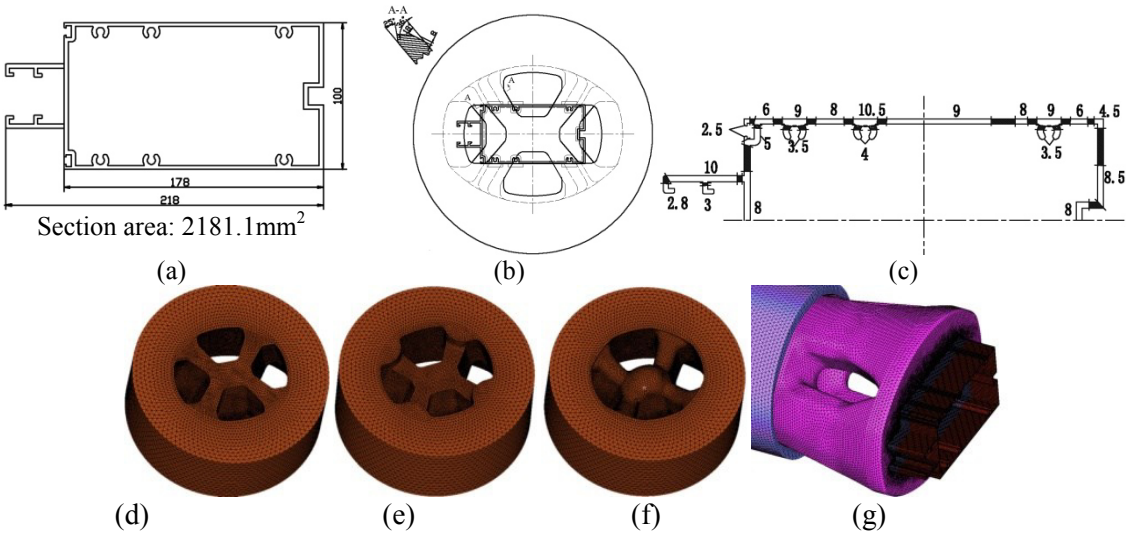

(a) (b) (c)

(d) (e) (f) (g)

FIGURE 2. The section and three different design schemes sketches(unit: mm)
(a)The section(b) Die(main view) (c) Bearing distribution(d)Scheme 1(regular design)
(e) Scheme 2(felled bridge) (f)Scheme 3(arc inlet) (g)The extrusion model of scheme 3

In this paper, 6063 aluminum alloy is used. The material constitutive model commonly used to describe deformation of hot aluminum can be expressed as[9]:

$$\sigma_s = B_0 \arcsin h\left\{\left[\frac{\bar{\dot{\varepsilon}} + \bar{\dot{\varepsilon}}_0}{A} e^{\frac{Q}{RT}}\right]^{\frac{1}{m}}\right\} \quad (1)$$

here, R is the universal gas constant, T is the absolute temperature, Q is the activation energy, B_0, A and m are temperature independent material constants. The parameters for AA6063 in detail are given by Halvorsen and Aukrust [10]. Besides, H13 steel is used for dies and tools, as shown in Table 1.

TABLE 1 Parameters for 6063 aluminum alloy and H13 steel

Parameters(6063)	Values	Parameters(H13)	Values
Mass density(ρ) (kg/m^3)	2700	Density(ρ) (kg/m^3)	7870
Stress constant (B_0) (MPa)	25	Young's modulus (GPa)	210
Activation energy(Q) （J/mol）	141550	Poisson's ratio (v)	0.35
Universal gasconstant (R)(J/mol·K)	8.314	Specific heat(C) (J/kg·°C)	460
Stress exponent (n)	5.385	Coefficient of heat conduction(k) (W/m·°C)	24.3
Initial effective strain-rate ($\bar{\dot{\varepsilon}}_0$)	0.4		
Reciprocal strain factor (A)	5.91052×10^9		

RESTULTS AND DISCUSSION:

1. Stress load results

Fig. 3 illustrates the von Mises equivalent stress distribution of these three design schemes. The cut planes arerisk sections and the circles show the locations of maximum von Mise equivalent stress places. Table 2 lists the maximum von Mises equivalent stress of the dies and the average extrusion forces of three different schemes.

In Fig. 3, it demonstrates that the von Mises equivalent stress distribution patterns are similar. The values of von Mises equivalent stress are close between scheme 1 and scheme 2. The values in scheme 1 are less than scheme 2, and those in scheme 3 are the least.

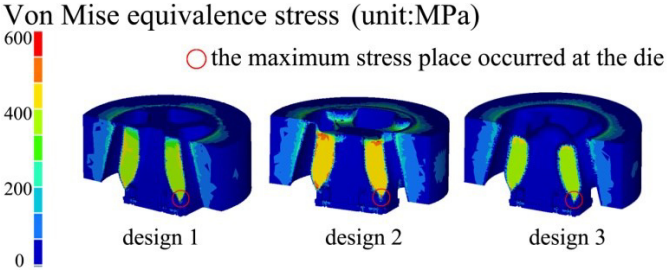

FIGURE 3. Von Mises equivalent stress distribution of the mandrel for three different design schemes

TABLE 2 Simulation load results for dies of different schemes

	Maximum von Mises equivalent stress (MPa)	Average extrusion force(MN)
1	696.4	20.46
2	723.1	22.22
3	522.5	20.63

As shown in Table 2, the maximum von Mises equivalent stresses in scheme 1 and scheme 2 are 696.4Mpa and 723.1MPa, respectively. However, the stress in scheme 3 is just 522.5MPa, only 75% of scheme 1 and 72.3% of scheme 2. The average extrusion forces in scheme 1 to scheme 3 are 20.46MN, 22.22MN and 20.63MN respectively.

In order to further investigate the effects of the arc shape inlet structure design, three typical planes are cut to plot the curve of the von Mises equivalent stress.As shown in Fig. 4, the maximum stress occurs at No. 12 location where the weakest place of the bridge section is. It can be observed that the value of scheme 3 is the least, just 416.4MPa, while scheme 1 value is 490.6MPa and scheme 2 is 561.5MPa.

The minimum stress occurs at No. 1 and No. 14 places where the places are far away from the central line. In addition, an extreme value occurs at right angle place of scheme 1 and scheme 2 dies. In scheme 3 the angle is made to circular arc. In this case, the stress load seems to be continuous.

Similar situations can be found at Fig. 4(b) and Fig. 4(c) curves. The maximum stress are disappearing at the weakest place of the section planes. The Y direction plane is the No.10 area, and the values of three schemes are 605.6MPa, 677.7MPa and 488.2MPa respectively. The Z direction plane is the No.4 and No.15 areas. The maximum stress value of scheme 3 is less than the other two schemes and the uniformity of stress distribution of scheme 3 is better.

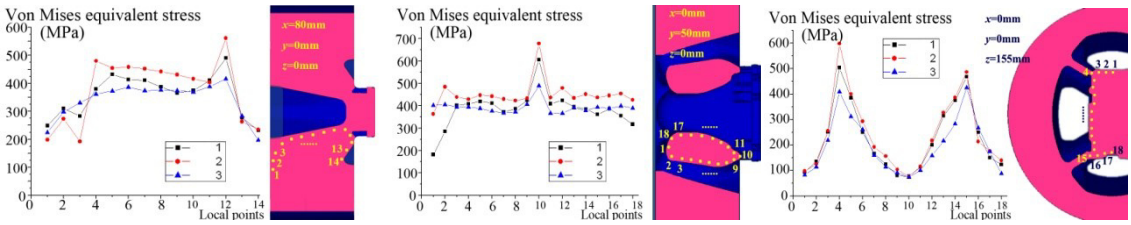

(a) (b) (c)

FIGURE 4. Curves of von Mises equivalent stress at three typical cut planes
(a) X direction (b) Y direction (c) Z direction

2. Flow velocity results

To study the flow uniformity properties in the extruding process of three different schemes, the section is divided into 36 regions, as shown in Fig. 5(a). A node in the middle place of each region represents the whole region. The section can be departed into several segments, region 1 to region 6 consist line AC segment, region 7 to region 9 consist the rib BC, and line CD,DE, EF et al, are consisted in the same way.

In this case, the node exit velocity data of 36 regions are collected and shown in Fig. 5(b). The exit velocity curves in Fig. 5(b) and the velocity data in Table 3 show the exit velocity distribution of three different schemes. Based on the velocity data results, it can be found that exit velocity of the area between point 14 and 15 and the area between 27 and 28 are much slower than the whole cross-section, where are the places of the screw holes. The velocities of these places are too slow to affect the extrusion stable forming.

Thus, the supply grooves of six screw holes are enlarged from 50mm to 65mm, so as to let more metal flow into them to balance the exit velocities.

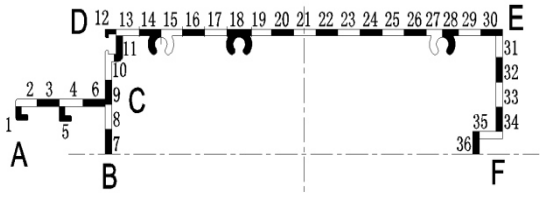

(a)

TABLE 3 Velocity field results of three schemes

	Average velocity(mm/s)		
Scheme	1	2	3
Global	71.19	71.85	71.96
AC	75.35	79.15	78.37
BC	77.80	82.05	79.90
CD	55.53	55.09	55.75
DE	59.79	59.73	61.96
EF	105.7	104.2	99.69

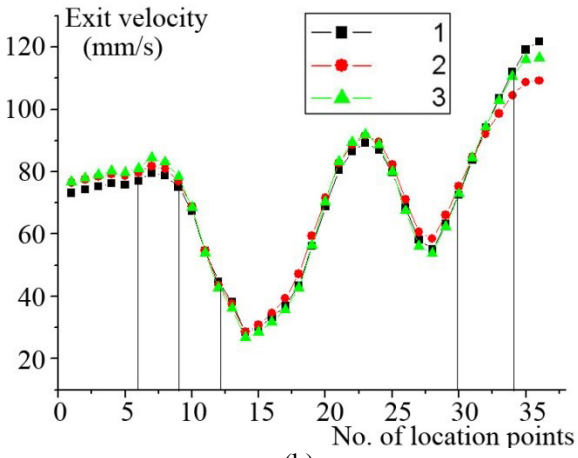

(b)

FIGURE 5. Flow velocity results:
(a)The location of the data points distribution
(b)The curve of exit velocity and the position

On the other hand, it points out that the variation trends of three curves in Fig. 5(b) are nearly the same. The average velocity of each section and the whole profile approach the same, too. It means that the die inlet structure makes few effects on the exit velocity distribution.

Combining with the stresses results, it demonstrates that the arc inlet die structure design hardly affect the stability of the extrusion forming process and the exit velocity distribution. However, the stress load situations are improved evidently, the maximum equivalent stresses of the dies are reduced to about 75% of two other die schemes and the distribution are much better than those.

3. Discussion

Based on Wu(1994)[11] extrusion theories, as far as simple right-angle forward extrusion is concerned, it is noticed that dead zone would be unavoidable at the right-angle place, such as Fig. 6(a) shown. The material near the container wall at the die face does not deform and a dead zone forms, over which the main body flows. This dead zone is subjected to shear stresses which are less than those needed to plastically deform it. Dead zones take a form that minimizes the redundant work of deformation. According to the law of least resistance, metal will choose an easy path to flow. In this case, metal remote from the layer with high stress forms in the billet near the container wall and at the boundary of the dead zone. It is directed into the orifice.

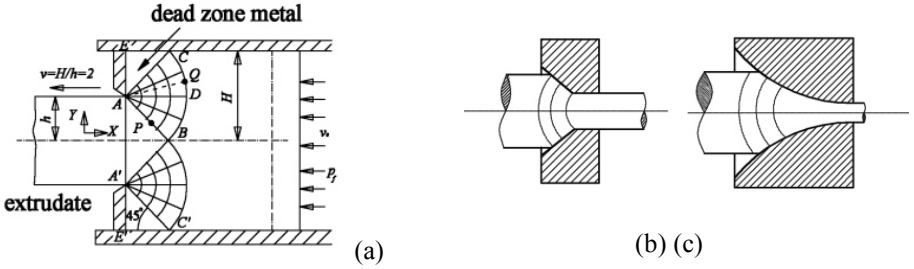

(a) (b) (c)

FIGURE 6. Dead zone theory and die structures for reducing shadow region
(a)Plot of slip-line field for right-angle forward extrusion (deformation rate is 50%)
(b) Conical structure(c) Streamline structure

In the dead zone, the metal is considered as stationary and high shearing deformation will occur at the boundary of the zone. The nonuniformity of metal flowing will be increased greatly due to the existence of the dead zone. Therefore, much

researcheshavebeen done to address this subject. Some cases to reduce the volume of dead zone are shown in Fig. 6(b)and Fig. 6 (c). Such these methods can improve the metal flow ability and drop extrusion forces evidently.

For the large hollow section dies, there is a large plane at the lateral direction which vertically blocks metal flow into the cavity like the simple right-angle forward extrusion situation. In this case, the dead zone may be formed. The arc inlet structure can cut down the area of the horizon plane to improve the flow ability of material.

CONCLUSIONS

An arc shape die inlet structure design method for large hollow section profiles is put forward to alleviate the load of the extrusion dies.

Compared with two traditional design methods without changing any other main factors, such as distribution of portholes, the shape and the depth of welding room etc, the diversity of hydrostatic stress and metal forming uniformity properties in the extruding process of the new method are not obvious, but working conditions of the die are greatly improved.

From the simulation results, the maximum stress of the arc inlet structure is only 75.0% and 72.3% respectively of those two regular design methods. The total stress is decreased by 10% to 20% respectively and the uniformity of stress load distribution is better.

REFERENCES

[1]Kleiner M., Schikorra M. (2006) Simulation of welding chamber conditions for composite profile extrusion. J MATER PROCESS TECH 177: 587–590.

[2]Fang G., Zhou J., andDuszczyk J.(2008) Effect of pocket design on metal flow through single-bearing extrusion dies to produce a thin-walled aluminium profile. J MATER PROCESS TECH 199: 91–101.

[3]Wu X.H., Zhao G.Q., Luan Y.G., et al(2006) Numerical simulation and die structure optimization of an aluminum rectangular hollow pipe extrusion process. Materials Science and Engineering A435-436:266–274.

[4]Chen Z.Z., Lou Z.L., andRuan X.Y. (2007) Finite volume simulation and mould optimization of aluminum profile extrusion. J MATER PROCESS TECH 190: 382–386.

[5]Van de Langkruis J., Lof J., Kool W. H., et al (2000) Comparison of experimental AA6063 extrusion trials to 3D numerical simulations, using a general solute-dependent constitutive model. Computational Materials Science 18: 381–392

[6]Lof J., Blokhuis Y.(2002) FEM simulations of the extrusion of complex thin walled aluminium sections. J MATER PROCESS TECH 122: 344–354.

[7]Liu J.A., Xie J.X.(2003) Large aluminum profile extrusion technology and optimization design for tools and dies. Metallurgical Industry Press, Beijing: 1–2.

[8]Pan J.Y., Zhou Z.Y., Wang Y. (2010) Design and numerical simulation analysis on extrusion die of aluminum section with complicated profile. Journal of Plasticity Engineering 17: 46–51.

[9]Lof, J., Klaseboer, G., Hue'tink, J.(2000) FEM simulations of aluminium extrusion using an elastoviscoplastic material model. In: Proceedings of the Seventh International Aluminium Extrusion Technology Seminar, ET2000, Chicago, USA, vol. II: 157–168.

[10]Halvorsen, F., Aukrust, T. (2006) Studies of the mechanisms for buckling and waving in aluminum extrusion by use of a Lagrangian FEM software. Int. J. Plast. 22:158–173

[11]Wu Shi-Dun(1994) Extrusion theory, NDI Press, Beijing: 180–183.

INTERPRETED MODELING FOR SAFETY AND EMISSIONS AT ROUNDABOUTS OR TRAFFIC SIGNALS IN CORRIDORS

Paulo Fernandes[1*], Margarida C. Coelho[1], Nagui M. Rouphail[2]

[1]Dept. Mechanical Engineering / Centre for Mechanical Technology and Automation (TEMA), University of Aveiro, Aveiro, Portugal
[2]Institute of Transportation Research and Education (ITRE), North Carolina State University, Raleigh, USA

ABSTRACT: Roundabouts have been gained increased popularity. The operational performance on a roundabout depends on its geometry, and traffic and pedestrian demand levels, which can result in a trade-off among capacity, safety and emissions. This research is focused on assessing how corridors with different intersections forms impact overall capacity, emissions and pedestrian safety. Vehicle dynamics, traffic and pedestrian demand data were collected from roundabout corridors in Portugal, Spain, and the United States (US), and turbo-roundabout corridors in the Netherlands. First, traffic performance and environmental impacts of innovative roundabout designs as turbo-roundabouts are analyzed. Second, locations along the corridors where emissions tend to be consistently high are identified followed by a comparison among roundabouts, traffic lights and stop-controlled junctions along corridors. Finally, a multi-objective approach is conducted to design optimal crosswalk locations in urban roundabout corridors and to assess the impact of spacing in closely-spaced intersections on capacity, emissions and safety.

INTRODUCTION: Some local authorities in the US and Europe have been constructed the use of a series of roundabouts on an arterial rather than the conventional solution of coordinate signalized intersections. The main advantages of this alternative are the following: *a*) possibility of U-turns on access restricted roadways that prevent some of the crashes related to the median openings (1); *b*) flexibility in maximizing intersection capacity without the need for excess turn lane storage (2); and *c*) higher likelihood to having better travel time, especially in the case of unevenly-spaced intersections (2). Roundabouts in series on an arterial have unique operational characteristics compared to their intersection counterparts. Basically, roundabouts do not allow the moving platoons of vehicles to maximize traffic performance owing to the high dispersed flows (3, 4).

While unreliable studies suggest that interdependent roundabouts on a corridor are successful in fulfill performance goals, little is known about the efficacy of this traffic calming technique as compared to a series of coordinated signalized intersections (3).A typical concern in the use of corridors with roundabouts is how traffic will perform. The main goal along a corridor with traffic lights is to coordinate lights to ensure good progression with a minimum number of stops. Roundabout corridors force all vehicles

* Corresponding author:

to slow down at every roundabout, causing several acceleration-deceleration cycles and, therefore higher emissions (4).
Roundabouts in close proximity to each other can exist along roundabout corridors. In such cases, the expected queue length at each roundabout becomes relevant. Closely-spaced roundabouts may improve safety by calming the traffic on the major roads because drivers may be reluctant to accelerate to the cruise speed at the mid-block section (5). However, overall traffic performance and emissions levels along a corridor with closely-spaced roundabouts may decrease in the conditions of intense traffic or pedestrian flows.
The available research in roundabout corridors has been centered on traffic performance (3, 6-10), but very few studies have addressed the influence of geometric characteristics of corridors on emissions (11, 12) and safety. SIDRA model includes a lane-based micro-analytical network tool that offers relevant emission analysis for roundabout corridors. However, it lacks for a proper evaluation in real-world roundabout corridors and comparison with other analytical and simulation tools (12). In summary, the following gaps were identified in the current literature:

- Qualitative and quantitative information on the environmental performance of a set of functionally interdependent roundabouts on arterials is lacking;
- There is a lack of understanding in assessing the operational and environmental differences between roundabouts in isolation and along corridors;
- There is not a proper comparison between corridors with roundabouts (both traditional layouts and turbo-roundabouts) and other forms of intersections such as traffic lights and stop-controlled junctions under different traffic conditions;
- Safety impacts of roundabout corridors on pedestrians have not fully explored, and do not include hypothetic trade-offs among capacity, emissions, and safety.

This doctoral thesis aims assessing the impact of the different segments of each pair of roundabouts along corridors on traffic performance, emissions and safety. The development of a methodology that incorporates geometric characteristics of the corridor and traffic stream on an integrated way is also a contribution of this work. The research herein will allow for solid knowledge in this topic by including a more extensive analysis, different case studies, intersection layouts, and traffic demand scenarios.
Thus, the novelty ideas of this doctoral thesis are as follows:

- Assessment of the impact of roundabout corridors on traffic performance and emissions. The design features that impact these fields along roundabouts corridors are hypothesized to be different from roundabouts in isolation;
- Development of a microscopic simulation platform of traffic, emissions and safety paired with a multi-objective analysis to compare the environmental and capacity performance of corridors with different traffic controls (conventional roundabouts, turbo-roundabouts, traffic lights and stop-controlled junctions);
- Identification of trade-off among traffic performance (delay), global (carbon dioxide-CO_2) and local (carbon monoxide-CO, nitrogen oxides-NO_X and hydrocarbons-HC) pollutant emissions and pedestrian safety (relative difference between pedestrian and vehicle speed) variables;
- Establishment of a relationship between above-mentioned variables and the design features of corridors (spacing) or pedestrian facilities (crosswalk location).

This doctoral thesis focuses on increasing the understanding on the following issues:

- How do design features of roundabout corridors affect vehicle dynamic patterns, traffic performance, pollutant emissions, and safety?
- What are the main differences between spatial distribution of emissions between roundabouts in isolation and along corridors?
- How do vehicular traffic performance and emissions vary under different traffic demands for corridors with roundabouts and other forms of intersections?
- What are the optimal design features to improve the efficiency of roundabout corridors in terms of traffic performance, emissions and safety?

PROCEDURES:FIGURE 1 shows an overview of the developed research. The duration of this work is four years (1st of June 2013-31st of May 2017). The major tasks in the first years were the revision of the technical literature, and the field data collection in several roundabout corridors. Next, the environmental and operational assessment of roundabout and turbo-roundabout corridors were conducted using empirical data. After that, a well-calibrated and validated microsimulation platform of traffic, emissions and safety was developed. This modelling platform was supported by VISSIM traffic model paired to an emission methodology (Vehicle Specific Power-VSP) and a safety (Surrogate Safety Assessment Model-SSAM) model. Finally, different alternative scenarios were implemented and evaluated, then the multi-objective analysis was performed using the Fast Non-Dominated Sorting Genetic Algorithm (NSGA-II).

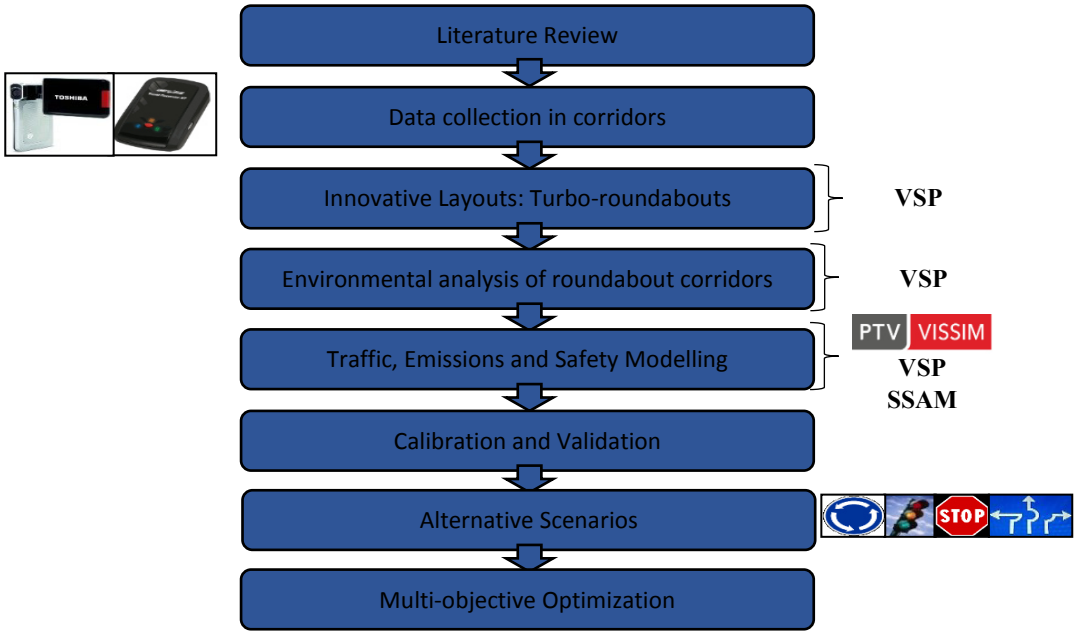

FIGURE 1. Overview of the developed research.

Data were collected at the candidate sites during local morning and evening peak on typical weekdays (Tuesday to Thursday), and under dry weather conditions:

- Traffic (Passenger Vehicles, Heavy Duty and Transit Buses) and pedestrian flows;
- Vehicle dynamic (speed, acceleration-deceleration on a second-by-second basis);
- Queue lengths;

- Time-gap distributions data;
- Posted speed limits.

Traffic and pedestrian flows, and time-gap distributions data were collected from overhead videos installed at strategic points along the study sites and recorded in 15-min time intervals. GPS Technology, in the form of an in-vehicle data logger, recorded the speed, latitude and longitude coordinates, and topographic conditions of the vehicles as they traveled along the corridors (in 1-second time intervals).

Eleven roundabout corridors in Portugal, Spain and in the US, and four turbo-roundabout corridors in the Netherlands were selected. The sites included the following range of attributes: *1*) number of roundabouts per corridor between 2 and 5; *2*) spacing ranged from 58 m to 350 m; *3*) similar corridor lengths; and *4*) relatively constant traffic flow along the main arterials. Approximately 1,300 GPS travel runs (100 at each site) were extracted for this research (≈800 km of road coverage).

RESULTS AND DISCUSSION: This section presents some main findings obtained in this thesis.

FIGURE 2 plots CO_2 and CO emissions amounts against the spacing and the entry deflection angle based on data collected from four roundabout corridors in Portugal and the US. For values lower than 150 m for the spacing, vehicles generated the highest values of CO_2 and CO emissions per unit distance. After, the values were relatively constant between 150 and 350 m. The R^2 values of CO_2 and CO emissions for spacing were 0.53 and 0.41, respectively. This is explained by sharper acceleration-deceleration rates within adjacent roundabouts, which have more impact on CO emissions. In contrast, the R^2 values for the entry deflection were lower than 0.20. These findings suggest that the impact of entry deflection angle on emissions decreases for low spacing, which is not verified on isolated roundabouts (4).

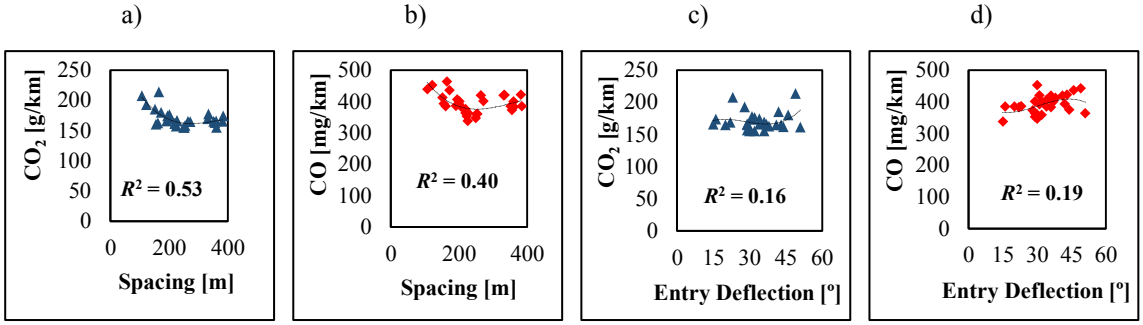

FIGURE 2. Emissions per unit distance for corridor design features: a) CO_2 versus spacing; b) CO versus spacing; c) CO_2 versus entry deflection angle; d) CO versus entry deflection angle.

The comparison of CO_2 and CO emissions per vehicle at turbo-roundabouts and multi-lane roundabouts are given in **FIGURE 3.** Six traffic demand scenarios were established where total traffic increased from 200 vph (Scenario 1) to 1,200 vph (Scenario 6) in 200 vph increments. The results showed that in both low and medium congestion levels (Scenarios 1-4) the emissions generated by vehicles at the turbo-roundabout were higher than the multi-lane layout (13%-CO_2;16%-CO). For high flow rates (Scenarios 5-6), turbo-roundabouts yield even more emissions than the multi-lane layout (19%-CO_2; 23%-CO). This was possible due to the longer stop-and-go cycles that vehicles experienced at turbo-roundabout. Also, the time spent by vehicles was found to be more impact on emissions at turbo-roundabouts than the deceleration-acceleration rates.

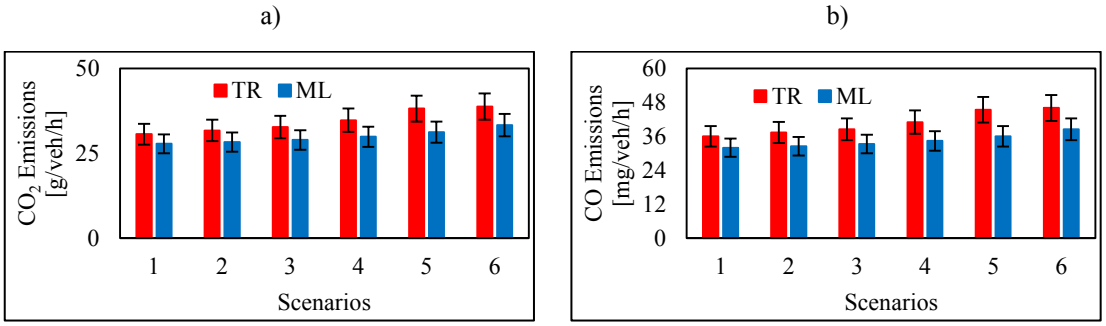

Legend: TR – Turbo-Roundabout; ML – Multi-lane Roundabout

FIGURE 3. Variation of the emissions per vehicle for different traffic scenarios: a) CO_2; b) CO.

TABLE 1 compares emissions and traffic performance parameters of a corridor with four roundabouts in Mealhada and equivalent signalized and stop-controlled arterials for the same location. Some observations can be drawn: *i*) roundabouts led to the lowest number of vehicle stops and were environmentally better than the traffic lights solution (4% to 5%, depending on the pollutant); *ii*) traffic lights were the worst solution for both time periods: emissions increased about 7% and 2% compared with roundabout layout in the morning and evening peak periods, respectively while the number of stops increased more than 50%; *iii*) stop-controlled was the best solution in both time periods for emissions and some mobility measures: 12% less vehicle emissions and nearly 16% less travel time. The unbalanced traffic flows between main roads and minor roads justified the advantages of the implementation of the stop-controlled solution in this case.

TABLE 1. Variation of emissions and traffic performance parameters per location in relation to the roundabout corridor, during the morning peak hour (8:00-9:00 a.m.), evening peak hour (5:00-6:00 p.m.) and two time periods.

Period	Corridor	Emissions				Traffic Performance	
		CO_2 (kg)	CO (g)	NO_X (g)	HC (g)	Travel Time (s/veh)	Total stops
Morning peak	**Roundabouts**	1,648	51,333	9,317	756	58.8	851
	Signalized	8%	8%	7%	6%	3%	50%
	Stop-controlled	-12%	-12%	-11%	-13%	-15%	7%
Evening peak	**Roundabouts**	1,778	54,819	9,847	794	61.8	692
	Signalized	2%	3%	3%	2%	-1%	54%
	Stop-controlled	-13%	-12%	-10%	-12%	-16%	13%
Two time periods	**Roundabouts**	3,426	106,152	19,164	1,550	60.2	1543
	Signalized	5%	5%	5%	4%	1%	52%
	Stop-controlled	-12%	-12%	-11%	-13%	-16%	10%

Multi-objective optimization of the crosswalk at different locations between closely-spaced roundabouts was conducted for eight different locations in Portugal, Spain and the US. **FIGURE 4** plots the normalized crosswalk locations which minimize CO and CO_2 against spacing for these corridors. Specifically, 0 is the location at the yield lane of roundabout while 1 is at the yield lane of the upstream roundabout. There was a good regression between relative optimized locations for CO_2 and CO and spacing between roundabouts ($R^2 > 0.72$) using exponential models (see **FIGURE 4**). The scattered graphs showed that for values lower than 100 m for the spacing, the relative location of the optimal crosswalk was approximately in 20%-30% of the spacing length. After that,

the crosswalks were located near the midway position, between 140 and 200 m of spacing.

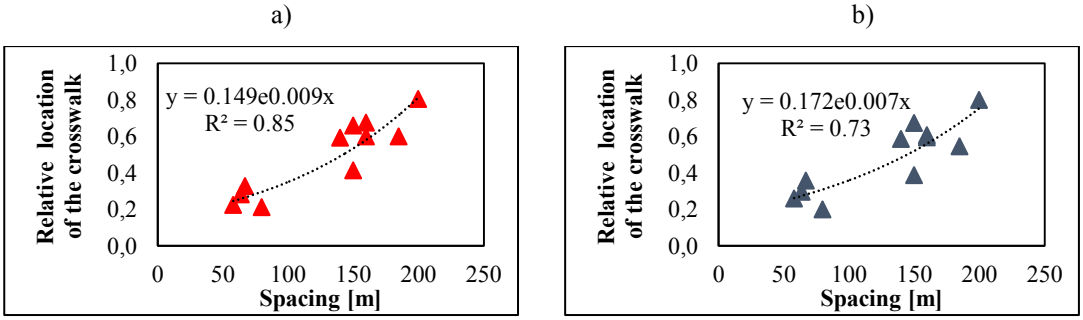

FIGURE 4. Relative location of the optimal crosswalk: (a) CO_2 vs. spacing; (b) CO vs. spacing.

Acknowledgement: P. Fernandes acknowledges the support of the Portuguese Science and Technology Foundation (FCT) – Scholarship SFRH/BD/87402/2012.

REFERENCES

[1] Alluri P, Gan A, Diaz A, Steiner R. (2015) Safety Impacts of Access Management Features near Roundabouts. Transportation Research Record: Journal of the Transportation Research Board. 2517:28-36.
[2] Rodegerdts L, Jenior PM, Bugg ZH, Ray BL, et al. (2014) Evaluating the Performance of Corridors with Roundabouts. Washington, DC: National Cooperative Highway Research Program, Report No.: NCHRP 772.
[3] Bugg Z, Schroeder B, Jenior P, Brewer M, Rodegerdts L. (2015) A Methodology to Compute Roundabout Corridor Travel Time. Paper presented at: Transportation Research Board 94th Annual Meeting, Washington, DC, United States.
[4] Coelho MC, Farias, TL, Rouphail NM. (2006) Effect of roundabout operations on pollutant emissions. Transportation Research Part D: Transport and Environment.11(5): 333-343.
[5]Rodegerdts L, Bansen J, Tiesler C, Knudsen J, Myers E, Johnson M, et al. (2010) Roundabouts: An Informational Guide (Second Edition). Washington, DC: National Cooperative Highway Research Program, Report No.: NCHRP 672.
[6]Thieken SL, editor. Implementing Multi-Lane Roundabouts in Urban Areas. (2008) Proceedings of the Transportation Land Use, Planning, and Air Quality ed., American Society of Civil Engineers, Reston, VA:41-51.
[7] Isebrands H, Hallmark, S., Fitzsimmons, E., Stroda, J. (2008) Toolbox to Evaluate the Impacts of Roundabouts on a Corridor or Roadway Network. St. Paul, MN: Minnesota Department of Transportation, Research Services Section, Report No.: MN/RC 2008-24.
[8] Ariniello, A.J. Are Roundabouts Good for Business? [Internet]. 2004 [updated 2014 Set 20; cited 2014 Set 20]. Available from: www.cityofgolden.net/media/roundaboutpaper.pdf.
[9] Krogscheepers J, Watters, M. Roundabouts along Rural Arterials in South Africa. (2014) Paper Presented at: Transportation Research Board 93nd Annual Meeting, Washington, DC, United States.
[10] Woodmansey A. (2014) Montana's Roundabout Corridor: Convincing the Stakeholders and Ourselves. Paper Presented at: Transportation Research Board 4th International Roundabout Conference, Seattle, WA, United States.
[11] Silva AB, Mariano P, Silva JP. (2015) Performance Assessment of Turbo-roundabouts in Corridors. Transportation Research Procedia.10:124-33.
[12] Akçelik R. (2014) Modeling Queue Spillback and Nearby Signal Effects in a Roundabout Corridor. Paper Presented at: 4th International Roundabout Conference, Transportation Research Board, Seattle, WA, United States.

ON THE MAIN SIMILARITIES AND DIFFERENCES BETWEEN NUMERICAL HEAT TRANSFER AND FLUID FLOW, AND THE GOOGLE PAGE RANK FORMULATION

V. A. F. Costa

TEMA - Centro de Tecnologia Mecânica e Automação, Departamento de Engenharia Mecânica, Universidade de Aveiro, Campus Universitário de Santiago, 3810 - 193 Aveiro, Portugal

ABSTRACT: Interesting similarities and subtle differences exist between numerical heat transfer and fluid flow and the Google Page Rank formulation. Similarities and subtle differences exist on the continuum and discrete nature of the base problems, on the main principles behind the governing equations, on the main principles and steps leading to the *discretization* equations, on the relationships between coefficients of the *discretization* equations, on the matrices of the systems of *discretization* equations, on the relaxation of the *discretization* equations, and on the used methods to solve the *discretization* equations. A parallel analysis of both situations is a challenging exercise, thrice from the physical, algebraic and numerical viewpoints. It is also a motivating exercise for students of algebra and of numerical methods, as so different situations are based on similar analysis, and on similar scientific basis and knowledge.

INTRODUCTION: A similar (parallel) structure exists on the main issues involved in numerical heat transfer and fluid flow and the Google Page Rank formulation. Even if such parallel analysis does not add useful contributes for those working on numerical heat transfer and fluid flow or on the Google Page Rank formulation, it is an interesting exercise as similar analysis, principles and algebra are involved. The main motivation of this work is to expose and explore this parallel analysis, proposed as a motivating and challenging exercise from the pedagogical point of view, and especially for those interested in numerical heat transfer and fluid flow.

NUMERICAL HEAT TRANSFER AND FLUID FLOW: Heat transfer and fluid flow are of continuum nature, governed by partial differential equations, which for steady 2D situations with no source terms can be cast in the general common form [1]

$$\frac{\partial}{\partial x}\left(\rho u\phi\right)+\frac{\partial}{\partial y}\left(\rho v\phi\right)=\frac{\partial}{\partial x}\left(\Gamma_\phi\frac{\partial\phi}{\partial x}\right)+\frac{\partial}{\partial y}\left(\Gamma_\phi\frac{\partial\phi}{\partial y}\right) \tag{1}$$

Obtaining the numerical solution of Eq. (1) starts accepting only to know the solution at a set of selected points (nodes) $\left(x_i,y_i\right)$ of the domain, $i=1,...,N$, N being the total number of nodes. Placement of the nodes on the domain defines the numerical mesh (grid), and the originally continuum problem is converted on a discrete problem.

Eq. (1) sets a relationship between derivatives, whose discrete analogue sets a relationship between values of ϕ_i at different nodes $\left(x_i,y_i\right)$, which are stronger as the nodes are closer. Only ϕ at the direct neighbors of node *i* is related with ϕ_i. Nodes that

are non-direct neighbors exchange information indirectly, through the intermediate nodes separating them.

The discrete version of Eq. (1) sets the relationship between ϕ at node *i* and at its direct nodes, which can be expressed in the form [1]

$$\phi_i = \sum_{j=1(j\neq i)}^{N} a_{i,j}\phi_j \Leftrightarrow [\mathbf{I}]_{N\times N}[\phi]_{N\times 1} = [\mathbf{A}]_{N\times N}[\phi]_{N\times 1} \quad (2)$$

where [**I**] is the identity matrix, and [**A**] is the *modified adjacency system matrix*. Similarity exists between Eq. (2) and the equation expressing the eigenvalues of matrix [**A**], $[\mathbf{A}]_{N\times N}[\phi]_{N\times 1} = \lambda[\phi]_{N\times 1}$, and once the discretization equations written in the matrix form the solution is the dominant eigenvector of [**A**].

From the diffusive viewpoint ϕ_A is related with ϕ_B in the same way as ϕ_B is related with ϕ_A, and $a_{i,j}^d = a_{j,i}^d$. Convection has an upwind nature, and ϕ_A is related with ϕ_B in a different way as ϕ_B is related with ϕ_A, ϕ_i being conditioned essentially by ϕ at the upstream nodes of node *i*, and $a_{i,j}^c \neq a_{j,i}^c$. For simultaneous convection and diffusion, $a_{i,j} \neq a_{j,i}$, a situation illustrated in Fig. 1. Coefficients $a_{i,j}$ relating the direct neighbor nodes of node *i* are generally nonzero, and they are null otherwise. From physical reasons it is always $a_{i,j} \geq 0,\ \forall i,j = 1,...,N$ [1], and both geometry and topology are important issues.

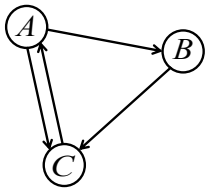

FIGURE 1.A network of nodes over the domain.

Once the discretization equation (2) obtained in the right way, the sum of coefficients $a_{i,j}$ over a line of matrix [**A**] is equal to 1, $\left(\sum_{j=1}^{N} a_{i,j}\right)_i = 1$, and as $a_{i,j} \geq 0,\ \forall i,j = 1,...,N$, [**A**] is a *right stochastic matrix*.

Additional information is usually available from boundary conditions This can be considered through an independent term b_i in the discretization equation (2), and coefficients b_i and $a_{i,j}$ are manipulated to accommodate any kind of boundary condition for the boundary node *i*. Eq. (2) comes thus written for the bundary nodes as

$$\phi_i = \sum_{j=1}^{N} a_{i,j}\phi_j + b_i \quad (3)$$

Different values of ϕ at different bundary nodes lead to different values of ϕ over the domain. If no boundary conditions are specified, a possible solution of Eq. (2) is

$\phi_c = \left(\sum_{j=1}^{N} a_{i,j} \right) \phi_c$, and thus $\sum_{j=1}^{N} a_{i,j} = 1$. This is a consistent result, as if no boundary conditions are specified solution reaches an equilibrium situation for which $\phi = \phi_c$ over the whole domain. This could be anticipated from Eq. (2), and if $[\mathbf{I}]_{N\times N}\left(M[\phi]_{N\times 1}\right) = [\mathbf{A}]_{N\times N}\left(M[\phi]_{N\times 1}\right)$ it is also $[\mathbf{I}]_{N\times N}[\phi]_{N\times 1} = [\mathbf{A}]_{N\times N}[\phi]_{N\times 1}$, for $M \neq 0$. Thus, any solution for ϕ is possible, and different solutions are related through different multiplying factors *M*.

Solution of Eq. (3) is obtained using iterative methods, and the changes of ϕ_i from one iteration k to the next, $k+1$, are under-relaxed (damped) ($0 \leq \alpha \leq 1$) writing Eq. (3) as

$$\phi_i^{k+1} = \phi_i^k + \alpha \left(\sum_{j=1}^{N} a_{i,j}\phi_j^{k+1} + b_i - \phi_i^k \right) \Leftrightarrow \phi_i^{k+1} = \left(\alpha \sum_{j=1}^{N} a_{i,j}\phi_j^{k+1} + \alpha b_i \right) + (1-\alpha)\phi_i^k \quad (4)$$

From Eq. (3) it is seen that the term within parenthesis on the left-hand side is the change induced on ϕ_i from iteration *k* to the next, $k+1$. Once convergence reached, $\phi_i^{k+1} \approx \phi_i^k$, Eq. (4) is the same as the original discretization equation (3), and the solution is not affected by the relaxation factor. Relaxation factor conducts variables' values towards the solution, but it does not affect the solution.

Boundary conditions can be conveniently considered to have the coefficient of ϕ_i higher than the sum $\sum_{j=1}^{N} a_{i,j}$, to satisfy the Scarborough criterion at the boundary nodes, and ensuring convergence of iterative methods of solution [1]. Under-relaxation also contributes to the verification of this criterion, as $\alpha \sum_{j=1}^{N} a_{i,j} \leq 1$ if $0 < \alpha \leq 1$.

GOOGLE PAGE RANK FORMULATION: There are *N* web pages referring to each other, and the problem itself has a discrete nature. The main question is to obtain, in an ordered way, how each page is referred by the other pages, and in this sense how is it relevant. To the user is important to have the most relevant pages ordered when searching the web. The problem was worked firstly in a consistent and systematic way by Brin and Page [2], setting the scientific basis of the Google search engine.

Considering Fig. 1, *A* is *seen* by *B* and by *C*, *B* is *seen* by *C*, and *C* is *seen* by *A*. As *A* is *seen* by more than one node, it is assumed that its page rank is due *equally* to all the other pages seeing it. For the situation illustrated in Fig. 1, the same as presented by Page [3], it is $\phi_A = \phi_C$, $\phi_B = (1/2)\phi_A$, $\phi_C = (1/2)\phi_A + \phi_B$. In this way, if page *j* is seen by n_j pages, its page rank ϕ_j contributes *uniformly* as ϕ_j / n_j for each of these n_j pages. There is thus an uniform and full repartition of the page rank of a given page *j* by all the n_j pages seeing it. Thus page with a high page rank contributes to increase the page ranks of the pages seeing it, and vice-versa. Following this principle, for each node *i* is obtained a *discretization* equation in the form

$$\phi_i = \sum_{j=1(j\neq i)}^{N} a_{i,j}\phi_j \Leftrightarrow [\mathbf{I}]_{N\times N}[\phi]_{N\times 1} = [\mathbf{A}]_{N\times N}[\phi]_{N\times 1} \quad (5)$$

where [**I**] is the identity matrix, and [**A**] is the modified adjacency system matrix. Also in this case, it is to be noted the similarity of Eq. (5) and that expressing the eigenvalues of [**A**], $[\mathbf{A}]_{N\times N}[\phi]_{N\times 1}=\lambda[\phi]_{N\times 1}$, and once the discretization equations written in the matrix form the solution is the dominant eigenvector of [**A**]. It is clear the existing similarity between Eqs. (2) and (5).

In this case the neighbor concept does not apply, but only the topological relationship setting which pages are seen by a given page, and the uniform repartition principle. If page *j* is not seen by page *i* it is $a_{i,j}=0$, and if page *j* is seen by n_j pages, including the *i* page, it is $a_{i,j}=1/n_j$. It is thus $a_{i,j}=1/n_j\geq 0,\ \forall i,j=1,...,N$, and Eq. (5) can be rewritten as $\phi_i=\sum_{j=1}^{N}\frac{1}{n_j}\phi_j$, noting that $\left(\sum_{i=1}^{N}a_{i,j}\right)_j=\left(\sum_{i=1}^{N}\frac{1}{n_j}\right)_j=1$ as when summing along all the lines *i* of any column *j* of [**A**] $a_{i,j}=1/n_j$ appears n_j times, and the sum of coefficients $a_{i,j}$ over a column of [**A**] is equal to 1. Due to that, and to the fact that $a_{i,j}\geq 0,\ \forall i,j=1,...,N$, [**A**] is a *left stochastic matrix*.

In this case: (*i*) There are no boundary conditions to be considered; (*ii*) The principle of uniform repartition ensures that no uniform values of ϕ are obtained in the whole domain (unless $a_{i,j}$ coefficients are uniform for all the nodes); and (*iii*) There is no analogous to the foregoing result setting that $\phi_c=\left(\sum_{j=1}^{N}a_{i,j}\right)\phi_c$. It is to be retained that if $[\mathbf{I}]_{N\times N}\left(M[\phi]_{N\times 1}\right)=[\mathbf{A}]_{N\times N}\left(M[\phi]_{N\times 1}\right)$ it is also $[\mathbf{I}]_{N\times N}[\phi]_{N\times 1}=[\mathbf{A}]_{N\times N}[\phi]_{N\times 1}$, for $M\neq 0$. Any solution for ϕ is possible, different solutions being related through different multiplying factors *M*.

Solution of Eq. (5) is obtained using iterative methods, and the changes of ϕ_i from iteration k to the next, $k+1$, are under-relaxed (damped) ($0\leq\alpha\leq 1$) writing Eq. (5) as

$$\phi_i^{k+1}=\phi_i^k+\alpha\left(\sum_{j=1}^{N}\frac{1}{n_j}\phi_j^k-\phi_i^k\right)\Leftrightarrow\phi_i^{k+1}=\alpha\sum_{j=1}^{N}\frac{1}{n_j}\phi_j^k+(1-\alpha)\phi_i^k \tag{6}$$

From the foregoing relationships it is seen that the term within parenthesis on the left-hand side is the change induced on ϕ_i from iteration *k* to the next, $k+1$. It is clear that Eq. (6) is the similar equation to Eq. (4). It is to be noted that in this case the relationship between values of ϕ at the different nodes is not maintained at the same iteration level; Eq. (6) gives $\phi_i^{k+1}=f\left(\phi_j^k\right)$, which has an *explicit* character, and at each level of iteration solution is obtained individually for each node and not for all the nodes as a whole (implicit character) as for the numerical heat transfer an fluid flow case. Once convergence reached $\phi_i^{k+1}\approx\phi_j^k$, and it is indifferent to consider $\phi_i^{k+1}=f\left(\phi_j^k\right)$ or $\phi_i^{k+1}=f\left(\phi_j^{k+1}\right)$.

Additionally, it is set $\phi_i^k=1/N$ in the last term on the right-hand side of Eq. (6), not only as the first value for iteration but *for any stage of iteration*. This procedure affects

the final distribution of ϕ_i, which is thus dependent of the relaxation factor α. This is not critical in this case, as there are no strict physical principles to be obeyed. Multiplication of first term (summation term) on the right-hand side of Eq. (6) by α induces a reduction of ϕ_i, and second term on the right-hand side of Eq. (6), $(1-\alpha)/N$, induces an increase of ϕ_i. This induces a decrease of the highest page ranks and an increase of the lowest page ranks, the minimum admissible page rank being $(1-\alpha)/N$.

It was referred above that any solution for ϕ is possible, different solutions being related through different multiplying factors *M*. Once things are made on the right way, page ranks can be seen as probabilities. Solution of Eq. (6) is obtained iteratively, and the first approximation is taken as $\phi_i^1 = 1/N$, $\forall i = 1,...,N$, and it is $\sum_{i=1}^{N} \phi_i^1 = 1$. Having the solution for any level of iteration $k(k \geq 1)$, satisfying $\sum_{i=1}^{N} \phi_i^k = 1$, it can be obtained from Eq. (6) that it is also $\sum_{i=1}^{N} \phi_i^{k+1} = 1$. In fact, taking the summation, and using Eq. (6) in the iterative sense it is

$$\sum_{i=1}^{N} \phi_i^{k+1} = \sum_{i=1}^{N} \left[\alpha \sum_{j=1}^{N} \frac{1}{n_j} \phi_j^k + (1-\alpha) \frac{1}{N} \right] \Leftrightarrow \sum_{i=1}^{N} \phi_i^{k+1} = \sum_{j=1}^{N} \left[\left(\alpha \sum_{i=1}^{N} \frac{1}{n_j} \phi_j^k \right)_j + (1-\alpha) \frac{1}{N} \right] \quad (7)$$

In the first equation two summations exist, the first (in *j*) along the columns of [**A**], and the second along the lines of [**A**]. This order can be inverted for convenience, summing firstly along the lines of [**A**] and after along its columns, and the righ-hand side form of Eq. (7) is obtained.

Taking into consideration Eq. (6), $\left(\alpha \sum_{i=1}^{N} \frac{1}{n_j} \phi_j^k \right)_j = \alpha \phi_j^k$, and Eq. (7) gives

$$\sum_{i=1}^{N} \phi_i^{k+1} = \sum_{j=1}^{N} \left[\alpha \phi_j^k + (1-\alpha) \frac{1}{N} \right] = \alpha + (1-\alpha) = 1, \ \forall \alpha \ (0 < \alpha \leq 1), \ \forall k \geq 1 \quad (8)$$

In general, it is thus $\sum_{i=1}^{N} \phi_i = 1$ for any level of iteration, and the page ranks have the meaning of probabilities. Original work by Brin and Page [2] considers only $(1-\alpha)$ as the last term on the right-hand side of Eq. (7), thus not ensuring result given by Eq. (8), what was corrected on the Page Rank patent [3]. Relaxation factor α needs to be the same for all the nodes, in order to have $\sum_{i=1}^{N} \phi_i = 1$ at any level of iteration, even if it can take different values at different levels of iteration.

Google has a collection of web pages, and knows how each page is seen by the other pages (the $a_{i,j}$ coefficients). Web search is a dynamic process, and coefficients $a_{i,j}$ are permanently changing. Google obtains the page rank from time to time, based on the best values of coefficients $a_{i,j}$, a process usually referred to as the *Google dance*.

CONCLUSIONS: Both geometry and topology are important in numerical heat transfer and fluid flow, and only topology is relevant for the Google Page Rank formulation. Heat transfer and fluid flow are continuum processes, its numerical counterparts being discrete approaches for them, but the Google Page Rank is of discrete nature itself. Discretization equations, indeed discretization equations for the continuum problems but not for the Google Page Rank formulation, have the same form in both cases. The modified adjacency matrix for numerical heat transfer and fluid flow is a right stochastic matrix and a left stochastic matrix for the Google Page Rank formulation. For the Google Page Rank problem it is set a total and uniform division of the page rank of a given page by all the pages seeing it. In both cases the solution is the dominant eigenvector of the modified adjacency matrix.
Boundary conditions need to be considered in numerical heat transfer and fluid flow, and if this is not the case a uniform distribution of the involved variable is obtained. No boundary conditions are needed nor prescribed in the Google Page Rank formulation, and no uniform distribution of the page rank is obtained in the general case. Values of the page ranks are not well defined, as infinite solutions exist, one solution being obtained from another solution by multiplication. Imposing that the summation of all the page ranks is equal to 1 gives to the page ranks the meaning of probabilities, in this case *probabilities of relevance*.
Discretization equations are solved using iterative methods, and under-relaxation is used to damp the changes on the variables from one iteration to the next. In numerical heat transfer and fluid flow solution is independent of the relaxation factor, and the solution is usually obtained in an implicit way. Relaxation is introduced on a similar way for the Google Page Rank formulation, but making the solution dependent on the relaxation factor. This results on a decrease of the highest page ranks and on an increase of the lowest page ranks, and limits the lowest possible page rank to a fixed value higher than zero. Another subtle difference is that in this case at each iteration level the solution is obtained in an explicit way.

REFERENCES

[1] Patankar, S. V., *Numerical Heat Transfer and Fluid Flow*, Hemisphere/McGraw-Hill, Washington D.C., 1980.
[2] Brin, S., Page, L., The anatomy of a large-scale hypertextual web search engine, *Proceedings of the 7th international conference on World Wide Web (WWW)*. Brisbane, Australia. pp. 107–117. http://dbpubs.stanford.edu:8090/pub/1998-8.
[3] Page, L., Method for node ranking in a linked database. US Patent 6,285,999 B1, September 2001.

DEVELOPMENT OF A LOW-ENERGY GAS SOLENOID VALVE FOR USE IN DOMESTIC WATER HEATERS

Hélder Giesteira[1*], Jorge Ferreira[1,2], Vítor Costa[1,2], Ricardo Carranca[3]

[1]Department of Mechanical Engineering, University of Aveiro
[2]Centre for Mechanical Technology & Automation, TEMA, University of Aveiro
[3]Department of Research and Development, Bosch Thermotechnology S.A.
[1,2]Campus Universitário de Santiago, 3810-193 Aveiro, Portugal
[3]Estrada Nacional 16, km 3,7, Cacia, 3800-533 Aveiro, Portugal

ABSTRACT: Currently, the actuators of the valves responsible for the gas flow assay in domestic water heating appliances have security measures, usually ensured by a spring. Given the nature of the actuation, high energy consumption is a characteristic of these actuators. In this sense, the present work aims to develop an alternative actuator with greater energy efficiency and a lower response time in order to regulate the gas flow more accurately.
The developed solution consists of a conventional solenoid with a permanent magnet plunger, allowing a bi-stable actuator with bi-directional movement. The developed concept is modeled and simulated using Matlab – Simulink software. In order to prove the validity of the simulation results, experimental tests with a prototype are also developed.

INTRODUCTION: In recent years there has been a significant increase in the level of demand on the quality in the home comfort. Part of the inevitable search for human comfort is related to the need of hot water for domestic use. The water heating process is done mainly by gas equipment.
In most modern equipment, the gas flow is regulated by electrovalves. Among these, stand out the solenoids, that model the gas passage hole in proportion to an electrical signal and others acting on a on/off way. They can also be classified according to the type of actuation, which can be: electromagnetic, piezoelectric, thermal and other types of unconventional actuation.
This study aims to develop a solenoid valve with reduced size, low response time and low energy consumption. For this, a study of the characteristic gas flow in existing equipment was made, in order to select the actuation capable of providing a displacement to the passage of the required gas flow. This search resulted in two possibilities: electromagnetic and piezoelectric actuation. In general, electromagnetic actuators have many advantages such as fast response, and low manufacturing cost when compared with the others actuators [1]. This actuation normally uses solenoids to switch the position of the plunger opposing the force of a spring, being an mono-stable actuation, where movement in one direction is given by the magnetic force, and another, in the opposite direction, is due to the force of the spring. With this, to keep the plunger in the position it is necessary to continuously feed the solenoid, resulting in an energy consumption which can sometimes be considerable given some limitations.
For conventional solenoids, the magnetic flux is easily reversed, by reversing the direction of the current intensity through the coil turns, but since it is a ferromagnetic

* Corresponding author: gaspargiesteira@ua.pt

plunger, it generates an electromagnetic force in one direction only [2]. In this study, the ferromagnetic plunger is replaced by a permanent magnet plunger, in order to obtain a bi-stable actuator movement in both directions.

CONCEPT DESCRIPTION: Figure 1 shows the schematics of the cross section of a limited travel solenoid valve with a permanent magnet plunger. Around the solenoid, there is an iron frame, wich serves as a magnetic circuit of the solenoid and is a factor that has a major influence on the magnetic efficiency of the system. The frame for this appliance that contributes to better efficiency, it is the tubular frame as it provides a magnetic flux of toroidal shape.

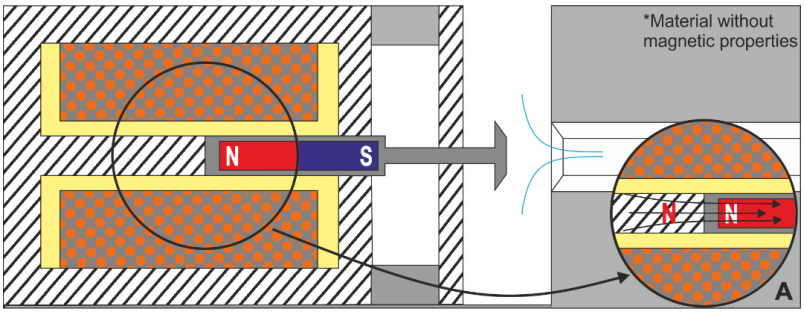

FIGURE 1 - Model illustration with tubular frame and permanent magnet

When the solenoid is not energized, the plunger (assuming that the north pole is closest to the ferromagnetic core) generates an attraction force to the ferromagnetic material due to the magnetic field of the permanent magnet. When a current passes through the coil with a direction such that the magnetic field due to the coil exits the ferromagnetic core, it generates a north pole at the core, section A of Fig. 1. Given that equal poles repeal each other, a repulsive force exists between the core and the permanent magnet, which results in a movement of the plunger. When the south pole of the permanent magnet is close enough to the ferromagnetic material at its right, generates an atraction force, thus reaching the second stable position. From this moment it is possible to stop the power release to the solenoid and keep the plunger in the forward position.
Note that between the permanent magnet and the ferromagnetic material is required the presence of a non-metallic material (nylon, or PTFE) in order to impose a minimum distance between them. If this is not the case, the lack of spacing between them generates a considerable force of attraction, and it is possible that the solenoid force is unable to overcome this force.
At the time when the current direction is changed, the magnetic flux is in the opposite direction and the ferromagnetic core becomes a south pole, originating a force which causes the plunger retreats to the initial position.

MODELLING THE SOLENOID VALVE: A model is a tool used to answer questions in relation to the system without having to resort to the construction and experimental testing. The mathematical model in this document consists of a set of relationships that can be used to describe the system behavior through simulations.
The mathematical model consists of several sub-models, wich are: electric model, magnetic model and mechanical model, all analyzed in detail separately. The starting point is the power driver of the solenoid valve, which must be able to reverse the current direction in the solenoid, aiming to achieve the gas mass flow rate provided by the solenoid valve.

Electric model:
By applying Kirchoff's Voltage Law to Fig. 1 we get [3],

$$V = IR + L_{sol}(I,x)\frac{dI}{dt} + N\frac{\partial \emptyset(I,x)}{\partial x}\frac{dx}{dt} \quad (1)$$

where V is the input voltage, I is the current, R is the coil resistance, $L_{sol}(I,x)$ is the reluctance of the solenoid, $\emptyset(I,x)$ is the total magnetic flux and N is the number of coil turns. Equation 1 is composed by three terms: the first is related to the voltage drop due to the coil resistance, the second is the induced voltage due to power variations, and the last is the electromotive force due to the movement of the plunger.

Magnetic model:
In order to determine $L_{sol}(I,x)$ and $\emptyset(I,x)$ present in Equation 1, it must be analyzed the total magnetic field present in the solenoid. Due to their dipoles, the permanent magnet has a magnetic field always present, and the second magnetic field arises when the coil is energized. Both sources of magnetic field present in the actuator can be analyzed separately. Thus, the total magnetic flux can be expressed by [3]:

$$\emptyset(I,x) = \emptyset_{sol}(I,x) + \emptyset_{pm}(I,x) \quad (2)$$

where $\emptyset_{sol}(I,x)$ is the magnetic flux due to solenoid coil and $\emptyset_{pm}(I,x)$ is the magnetic flux due to permanent magnet.
The purpose of the following analysis is to determine the paths of the flow due to the permanent magnet and the solenoid in different arrangements. For that the FEMM software (Finite Element Method Magnetics) was used.

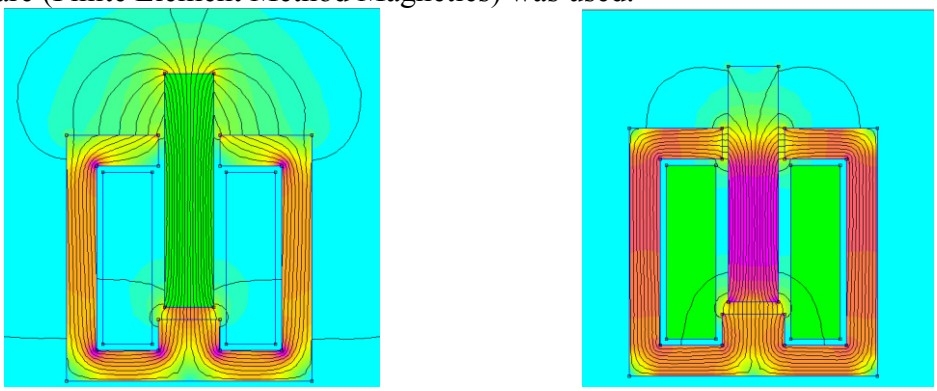

(a) Source**:** permanent magnet **(b)** Source: solenoid coil

FIGURE 2 – Magnetic flux path

In a first analysis it was assigned a null value to the solenoid current, to analyze only the flux due to the permanent magnet as shown in Fig. 2(a). Then, the material property of the plunger has been changed, becaming a ferromagnetic material, and applied a current of 1 [A] to the solenoid coil terminals to study only the magnetic field generated by the solenoid, Fig. 2(b).
When there is no current in the solenoid coil, the single magnetic source is the permanent magnet, as illustrated in Fig. 2(a). Fig. 3(a) represents the corresponding equivalent magnetic circuit, where R_x is the magnetic reluctance between the ferromagnetic core and the plunger, R_a is the magnetic reluctance between the top of the plunger and the solenoid frame, R_{pm} is the magnetic reluctance in the permanent magnet, and F_m is the magneto-motive force of the permanent magnet. Note that the reluctance of the ferromagnetic material of solenoid frame has been discarded, since the iron permeability is quite higher than the permeability of vacuum.

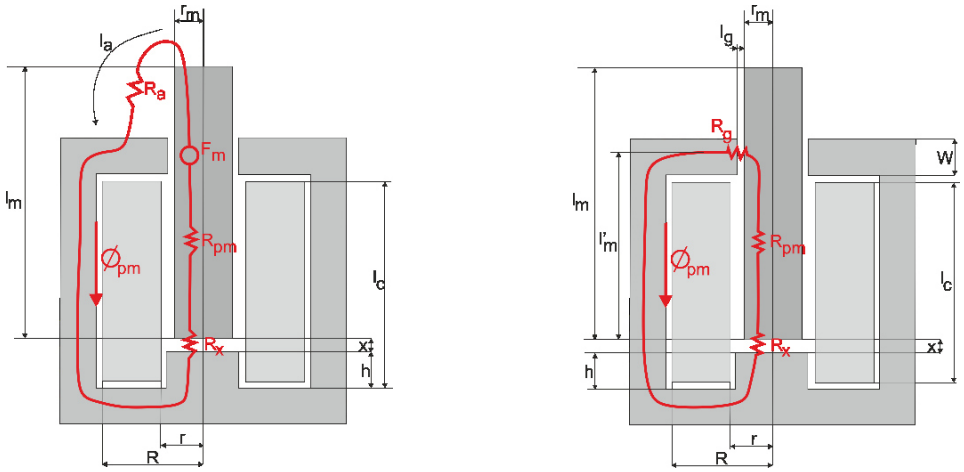

(a) Permanent magnet **(b)** Solenoid coil

FIGURE 3 – Equivalent magnetic circuit

From the equivalent circuit of Fig. 3(a) [3]:

$$F_m = \emptyset_{pm}(I,x)(R_{pm} + R_x + R_a) \tag{3}$$

It is known that for a permanent magnet of cylindical geometry with a leght l_m, and a constant axial magnetization direction along its axis,

$$F_m = \frac{B_r}{\mu_0} l_m \tag{4}$$

where B_r is the residual magnetism. The reluctances R_x, R_{pm} and R_a are expressed by:

$$R_x = \frac{x}{\mu_0 A} \qquad R_{pm} = \frac{l_m}{\mu_m A} \qquad R_a = \frac{l_a}{\mu_0 A} \tag{5}$$

Similarly, Fig. 3(b) is the equivalent circuit of Fig. 2(b), where only the magnetic field from de coil energization is present. R_g is the distance between the solenoid plunger and the frame. Reluctance by solenoid frame can be disregarded for the same reasons as already given.
Equation (6) is the resulting magneto-motive force of the previous equivalent circuit [3], Fig. 3(b).

$$NI = \emptyset_{sol}(I,x)(R_x R_g R_{pm}) \tag{6}$$

where R_x is given by Eq. (5), and R_{pm} and R_g are given by the following expressions:

$$R_g = \frac{l_g}{\mu_0 A_g} \qquad R_{pm} = \frac{l'_m - x}{\mu_0 A} \tag{7}$$

From Eq. (6) it is possible to determine $\emptyset_{sol}(I,x)$, and the inductance of the coil can be determined by the derivative of the magnetic flux of the solenoid, as can be concluded from the following equation [3]:

$$L_{sol} = N \frac{d\emptyset_{sol}(I,x)}{di} \tag{8}$$

Both magnetic fields create a force applied to the plunger: a force due to the permanent magnet and a force from the solenoid coil.

Knowing that the intensity of the magnetic field is maximum at the center of solenoid, one of the permanent magnet poles must be placed at this position. Thus, the force due to the coil is given by [3]:

$$F_{sol}(I,x) = M_{mag}\emptyset_{sol}(I,x) = \frac{B_r}{\mu_0}\emptyset_{sol}(I,x) \quad (9)$$

where M_{mag} is the magnetization of permanent magnet.
The attraction force of permanent magnet could be determined analytically. For the sake of simplification, the curves force – distance characteristics of permanent magnet with certain geometric dimensions and material are used.

Mechanical model:
As discussed previously, the magnetic force is present in the system dynamics. However, other forces influence the behavior of the solenoid valve.
The free body diagram illustred in Fig. 4 shows the presence of inertia of the plunger $M\ddot{x}$, frictional force F_a, the forces of attraction of the permanent magnet F_{pm} and, as already mentioned, the solenoid force $F_{sol}(I,x)$.

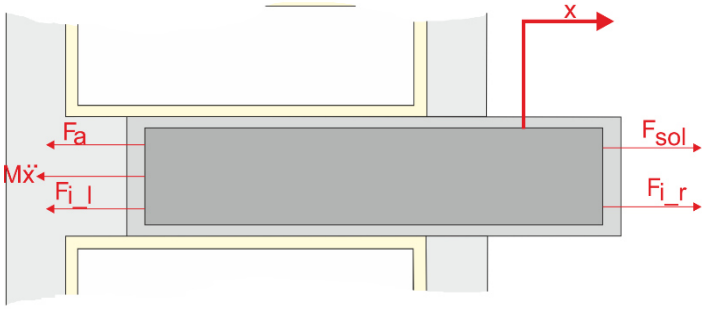

FIGURE 4 – Free body diagram

The attraction force from de permanent magnet can be decomposed in two forces in opposite directions: F_{i_l} is the force of attraction between the magnet and the ferromagnetic material left, and F_{i_r} is the force of attaction to the ferromagnetic material to the right of permanent magnet.
With the contribution of Newton's Second Law, the previous free body diagram can be translated into:

$$\ddot{x} = \frac{1}{M}\left(F_{sol}(I,x) + F_{i\_r} - F_{i_l} - F_a\right) \quad (10)$$

where M is the mass of plunger.
With the mathematical model completed, we resort to Matlab&Simulink to model each of the systems previously studied using block diagrams, for later simulate and analyze the dynamic behavior of the proposed concept.
RESTULTS: After analyzing the results obtained from the simulation, it is possible to prove the bistability and bidirectional movement of the plunger. By applying a voltage of $15\ V$, during $20\ ms$ it is possible to move the plunger between stable positions, Fig. 5.

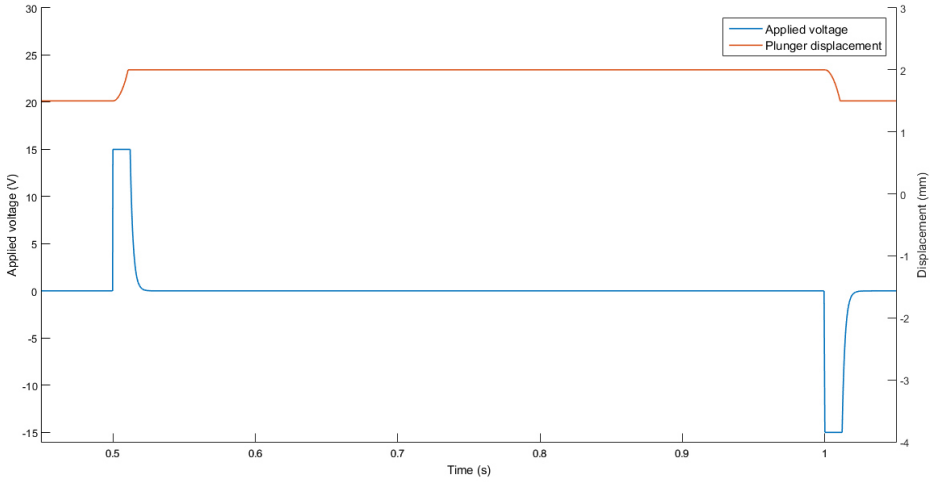

FIGURE 5 – Simulation results

To prove the validity of the developed model, the prototype of the actuator was constructed, Fig. 6.

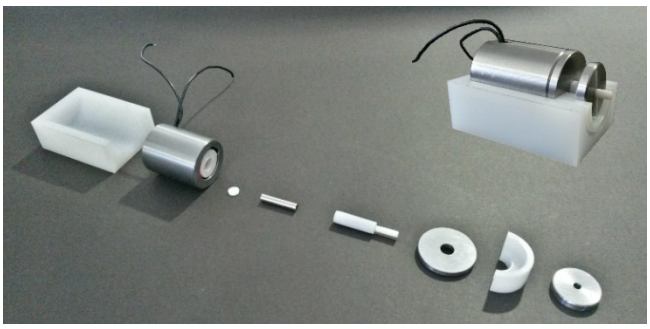

FIGURE 6 – Prototype of the developed actuator.

DISCUSSION: We developed a solenoid with a permanent magnet plunger, to operate in a gas vale with two stable positions and with low energy consumption.
With this study we conclude that a solenoid with ferromagnetic plunger, in the moment that reverses the direction of current flowing through the coil turns, reverses the magnetic flux, but does not reverse the direction of the magnetic force. Therefore, we used a permanent magnet plunger. It can be also concluded that the geometry of the solenoid frame and the air gap in the magnetic circuit are very important for the efficiency of the solenoid.
This work presents a contribution to the development of actuators of low energy consumption for use to control the gas flow rate of water heating equipment, representing an added value for these devices.

REFERENCES

[1] C.-W. Song and S.-Y. Lee, "Design of a Solenoid Actuator with a Magnetic Plunger for Miniaturized Segment Robots," *Appl. Sci.*, vol. 5, no. 3, pp. 595–607, Sep. 2015.
[2] E. P. Furlani, "Permanent Magnet Applications," in *Permanent Magnet and Electromechanical Devices*, Elsevier, 2001, pp. 207–333.
[3] D.-G. He, "Bi-directional Solenoid Actuator for Direct Alternative Fuel Injector," Concordia University, 2005.

DEVELOPMENT OF A LOW ENERGY CONSUMPTION PROPORTIONAL VALVE FOR WATER FLOW REGULATION

Paulo Soares[1], Jorge Ferreira[1,2], Vítor Costa[1,2], Raquel Vaz[3]

[1] Department of Mechanical Engineering, University of Aveiro, Campus Universitário de S.Tiago, 3810-193 Aveiro Portugal
[2] Centre for Mechanical Technology & Automation, TEMA, University of Aveiro, Campus Universitário de S.Tiago, 3810-193 Aveiro Portugal
[3] Department of Research and Development, Bosch Termotecnologia S.A., Estrada Nacional 109 km 3.7, Cacia, 3800-533 Aveiro Portugal

ABSTRACT: The water flow regulation is a key factor in domestic water heating. In this regard, components like the water valves are crucial, ensuring that the correct amount of water is delivered to the heater. This work presents the process of development of a proportional water valve. The main objectives are to develop and test a prototype of a high performance proportional valve for the regulation of the water flow rate while presenting a low energy consumption. The development was made using modelling and simulation tools such as MatLab/Simulink™. Besides the conceptual modelling, a prototype was built to test and validate the simulation results.

INTRODUCTION: Water is an essential part of our daily life. We use it in our kitchen activities, in our washing machines, in our gardens and in particular in our bath room. In many of these applications we use hot water. There are many types of water heating devices, that can have different operating principles, but they all have a common need, which is water flow regulation. In this sense, they all need a proportional water valve to regulate the inlet water flow rate. Typically, water proportional valves should be able to deliver the required amount of water while requiring a low energy consumption.

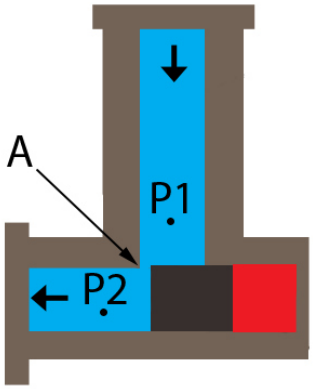

FIGURE 5. Proportional valve schematic.

The simplest way to regulate the water flow is to use an orifice and vary its cross section area. Figure 1 shows a simple schematics of a proportional valve. As can be seen, the orifice area changes with the movement of the body A. Also it is important to note that pressure P_2 exerts a longitudinal force on body A, which the actuator (in red, in Fig.1) needs to overcome. To move this body is necessary to have an electrical actuator like a solenoid or a stepper motor.

The solenoid actuators present a very good time response but they present a high energy consumption, since they need energy to hold one stable position. On the contrary, stepper motors don't need energy to maintain a position, thus presenting a lower energy consumption. The main disadvantages of the stepper motors are that they are dynamically slower when compared to the solenoid actuators, and also bigger in size. An alternative type of actuation is the use of hydraulic energy of the fluid to exert a force on the valve spool. This principle is used on high pressure oil hydraulic systems, like the ones that can be found on industrial and heavy machinery. In these systems the actuator only needs to regulate a small amount of hydraulic fluid to a chamber, where it will exert a force on the main spool, thus regulating the valve flow. As said the actuator only regulates a small flow, therefore it presents a lower energy consumption. This work tried to adapt these principles to a low pressure water valve, to be used in domestic equipment.

CONCEPT DESCRIPTION: As a small introductory note, it should be noted that the valve concept that is here presented, results from an extensive research work made throughout the development process. Figure 2 shows a simplified schematics of the proposed concept. The main components of this concept are the first stage spool, E_1, and the second stage spool E_2. The first stage spool is solenoid actuated, and regulates the inlet flow to a chamber where pressure is P_A. The second stage spool is hydraulically actuated by the pressure differential between P_A and P_B. This concept operates in the following way: Initially, both spools E_1 and E_2, are in closed position, not letting any water flow to pass from E to S. Then, E_1 is actuated, opening its orifice area and letting a small water flow into chamber with pressure P_A. Since chamber A and chamber B are connected by a small passage area, water starts to flow to chamber B. Chamber B is connected with the valve outlet to ensure that the system does not become static. The differential between pressures P_A and pressure P_B increases with the opening of the first stage orifice. This pressure differential is responsible for moving the E_2 spool. When E_2 moves, it opens the valve orifice, letting the main flow of water to pass. This makes it possible to overcome the flow forces acting at the second stage, and to achieve an amplification power. Aditionally, there is a spring assembled against the second stage spool to ensure that the valve is watertight when closed.

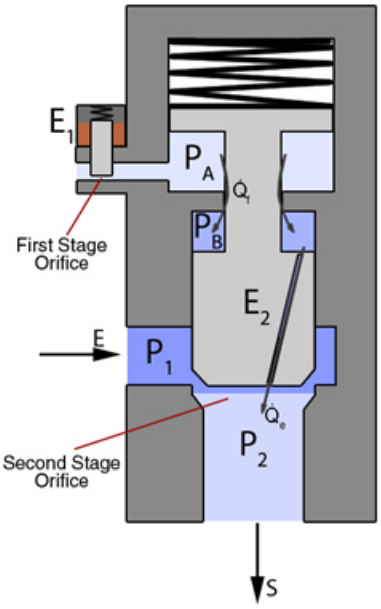

FIGURE 6. Proposed concept schematic.

MODELLING AND SIMULATION: It was necessary to evaluate if the described concept works, before fabricating any prototype. This evaluation was made using modelling and simulation tools such as Mathworks Simulink R2015a. To study the presented concept, a model was created. This model has three main components, based on the physical phenomena present in a water valve. These are, a component related with the water flow across the valve, a component related with the mechanical movement of the spools and at last, a component related with the eletrical model of the solenoid. To model the water flow across the valve, control volumes were considered. A control volume defines a valve chamber or zone that has a pressure, a volume and, inlet and outlet flows. Applying the mass conservation principle to a control volume and assuming that the water is slightly compressible it is possible to write Equation 1 [1], where **V** is the volume, **P** is the pressure inside the control volume, **t** is the time, **β** is the fluid compressbility factor and, **$\dot{Q}$** is the water flow rate that goes into or out of the control volume.

$$\frac{dV}{dt} + \frac{V}{\beta}\frac{dP}{dt} = \sum \dot{Q}_{in} + \sum \dot{Q}_{out} \tag{1}$$

The above equation is not enough to define a control volume. The inlet and outlet flow have to be determined for each control volume. Typically, in a water valve, the flow across an orifice occurs in turbulent regime. Under these conditions the water flow rate can be described by Equation 2 [1,2].

$$\dot{Q} = AC_d\sqrt{\frac{2\Delta P}{\rho}} \tag{2}$$

where **$\dot{Q}$** is the water flow rate across the respective orifice, **A** it is the orifice area, **ΔP** is the pressure differential across the orifice, and **ρ** is the fluid's density. The orifice geometry dictates its area. The most regular orifice geometries are of ring and circular format. In the model created, the first and second stage orifices use a ring format in which, the outter diameter depends on the spool position. As said earlier, another important component of the model is the mechanical behavior of the spools. Each spool was treated as a moving body, at which was applied the Newton's Second Law. The friction forces acting upon the spool were modeled by Equation 3, where $\mathbf{F_{static}}$ is the static friction force, **B** is the dynamic friction coefficient, and $\dot{x}$ the spools velocity.

$$F_f = F_{static} + B\dot{x} \tag{3}$$

To simulate the solenoid's behavior, a dynamic model was created. A solenoid has a resistive and inductive structure [3]. Applying Kirchoff's Second Law, it is possible to write Equation 4.

$$E = RI + L(x)\frac{dI}{dt} + I\frac{dL(x)}{dx}\frac{dx}{dt} \tag{4}$$

In this equation, E is the voltage supply, **R** the solenoids winding resistance, **I** the current and, **L(x)** the inductance, which varies with the solenoid plunger position. Based on Equation 4 [3], it is possible to determine the current that flows in the solenoid eletric circuit. The force produced by the solenoid's magnetic field can be defined by the Equation 5 [3], where **I** is the solenoid electrical current, **a** is the solenoid's length, **x**

the solenoid's position and, $\mathbf{L_0}$ a constant which depends on some of the solenoid's characteristics such as number of turns, diameter and magnetic permeability.

$$F = \frac{I^2}{2}\frac{aL_0}{(a+x)^2} \tag{5}$$

Up to here, all the model components have been explained. It remains only to explain how the above components were integrated to create a valve model. Figure 3 shows an overall diagram of how the model was implemented. An analogy between Figure 2 and Figure 3 can be made. Clearly there are as many control volumes as chambers or pressure zones, as indicated in Figure 2. First and second stage orifices, indicated as O_A and O_1, were considered to have a ring format, and also, to have its area varying with its spool position. The orifice between control volumes **A** and **B**, was modelled as a ring, since its passage area results from a shaft-hole fitting. Finally, orifice O_C was modelled as a circular orifice. It should be noted that through orifices O_B and O_C pass, respectively water flow rates, $\dot{\boldsymbol{Q}}_{\boldsymbol{f}}$ and $\dot{\boldsymbol{Q}}_{\boldsymbol{e}}$, as indicated in Figure 2. The solenoid model was implemented as described earlier, and its magnetic force acts upon the first stage spool. It is evident that this model has a large number of parameters, such as the spring stiffness, the spools contact areas, orifices passage areas and also the solenoid characteristics.

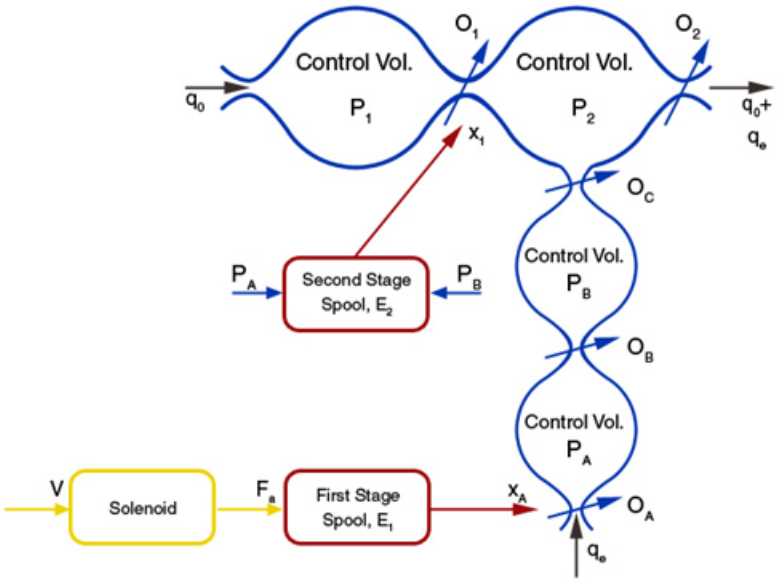

FIGURE 7. Schematics of the created model.

The best parameter configuration can be found by running simulations and comparing the results to what is the desired behavior. This was the first method employed to find a set of parameters that was adequate to the expected results. Then, with this set of parameters found, an optimization was made, to ensure that the designed valve has the best possible performance. This optimization consisted in using a global search algorithm from Matlab R2015a ('GlobalSearch' solver; 'fmincon' to find the minimum of the constrained squared error function), in order to find the spring stiffness and spring pre load which are better suited to the desired valve's response. The simulations were carried out using Simulink fixed-step solver ode14x (fixed-step size: 0.1 ms; solver Jacobian; method:'full perturbation'; extrapolation order: 4) so that high solution

accuracy and computational efficiency could be achieved. After defining all the model parameters, it was possible to obtain reasonable simulation results.
Figure 4 shows the flow in the valve for a ramp signal applied on the solenoid from 0 V to 5 V and then from 5 V to 0 V. The same simulation was runned for different inlet pressures, from 0.5 bar up to 6 bar. This shows that the proposed concept is capable of deliver a reasonable performance under different conditions.

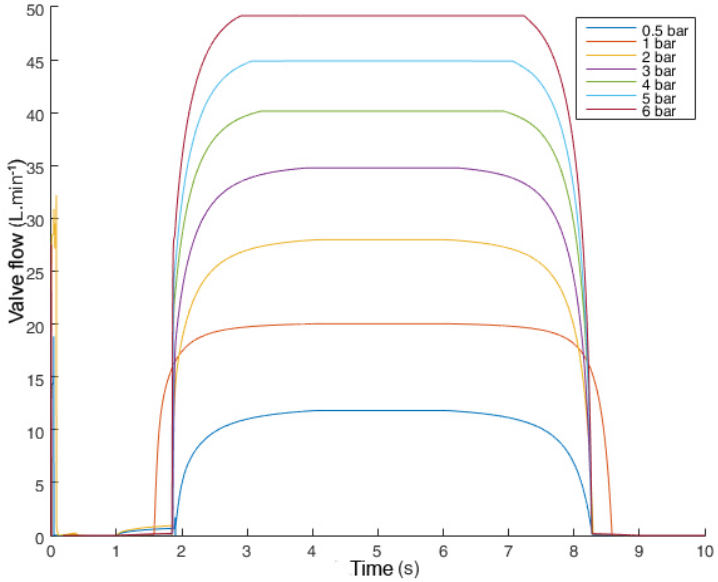

FIGURE 8. Flow evolution over time, for different inlet pressures.

PROTOTYPE FABRICATION: Having fully developed the model with reasonable simulation results, the next step was to build a prototype. The main purpose of building this prototype is to validate the results obtained from the simulations. The concept developed presents some complexity. Having this in mind, it was decided that the first tests to the prototype would not include the solenoid. This means that the first stage spool was actuated manually, with the purpose of verifying if the hydraulic principle of operation works. The prototype was built mainly with machining processes, such as turning and milling. All the components were made in aluminium, since it was the only material available at the time being. The prototype was designed to be representative of the schematics from Figure 2, however, it was necessary to pay attention to the machining process limitations. In Figure 5 (a) it is shown an exploded view of the prototype and, in Figure 5 (b) it is shown a photo of the prototype components.

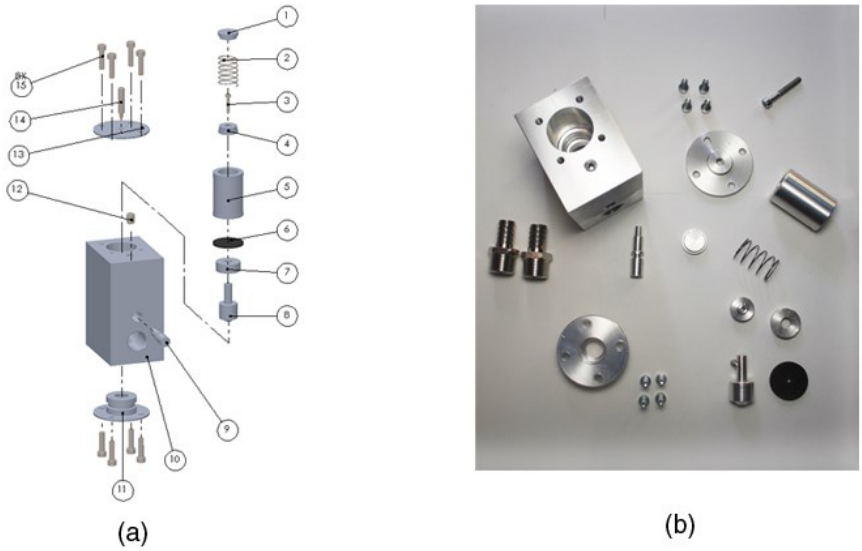

FIGURE 9. (a) Prototype exploded view. **(b)** Prototype machined components.

EXPERIMENTS AND DISCUSSION: The prototype was assembled and tested. The prototype testing was very simple, consisting basically in connecting the water inlet source to the valve body, and manually moving the first stage spool. Unfortenately, the prototype did not work as expected. The valve did not open, yet there was a small leakage water flow rate. When assembling the prototype, it could be observed that the second stage spool had a bigger static friction than expected, thus not moving properly. As a matter of fact, sometimes the second stage spool got stuck. It should be noted that the valve works with a low inlet water pressure (<10 bar), meaning that if the friction forces are too much high, the hydraulic actuation will not work properly, as is believed that happened. Analysing the prototype assembly it could be observed that there are two disaligned holes, resulting on an increased friction, since the first stage spool has to pass between these two holes. Despite the fact that the prototype did not work, it is possible to conclude that the mechanical complexity associated compromises the proper functioning of the valve. This leds to the need to explore a simpler concept amd prototype, that yet delivers the same results as the one that is presented on this work.

Acknowledgement: The authors would like to thank Eng. António Festas for its contribution, in fabricating the prototype that was built. They would like to thank Prof. António Ramos for its contribution, in defining the tolerances and fittings of the components.

REFERENCES

[1] J. A. F. Ferreira, "Modelação de Sistemas Hidráulicos para Simulação com Hardware-in-the-loop," Ph.D. Dissertation, DEM, UA, Aveiro, PT, 2003.
[2] H. E. Merrit, *Hydraulic Control Systems*. Cincinnati, USA: John Wiley & Sons, Inc., 1967.
[3] N. C. Cheung, K. W. Lim, and M. F. Rahman, "Modelling a linear and limited travel solenoid," *Proc. IECON '93 - 19th Annu. Conf. IEEE Ind. Electron.*, vol. 3, no. 2, pp. 1567–1572, 1993.

Notes

Notes

Notes

Notes

Notes

Notes

Notes

Notes

Notes

Notes

Notes

Notes

Aveiro, 2016

A.M. Oliveira, AB da Rocha, Abuain T, A. Frederic, Aguiar, P,
Aiping Zeng, Akihisa Ma A. tsuno, Alejandro Heredia, Alexander Tselev, R.

Alves De Sousa, G. Andrade-Campos, Andreas Ochsner, A. Hussnain, A.J.S.

Andrei L. Kholkin,António Bastos,Antonio C. M. Sousa,Antonio Ferreira,Antonio Luis Ferreira, Araujo, JP,

Augusto B. Lopes,Avinash Balakrishnan,Ayouchi R,Babu P,Bahadur, D,Bahlouli Nadia,Baniassadi M.,

Bardhan, NK , Razavi, Z, Markus J. Buehler, A.L.Kholkin, A.M., Balbashov, Vieira LG, Abe I, I. Bdikin,

Gil Gonçalves, Guerra, L, H Sein, H. Khyrandish, H. Youssef, H.M. Vieira, Hawaldar, R, Heredia, A, I. Antunes, Idrissa A.

K. Mossi, Ivonne Delgadillo, J. Lou, J. Read, Budhendra Singh, Bystrov Vladimir, Carlos Tomé, Barros-Timmons, Ana,

C. Picu, Chandra, S,Chi Zhou, Chun-Teh Chen, Claudia Buchheim, Costa Luis C, D. Corte-Real, D. Dixon, David Ruch, Del

Frari D, Dias, C,DS Misra, Duarte, P, Duncan Fagg,E, Okpalugo, E. Ahmed, E. Pereira, Edgar Rauch, Elby Titus, F. Teixeira-

Dias, F.X. Lu, Ferreira, AL, Fiedler T, Fréderic Barlat, C. Butuc, G Mishuris, G. Cabral, G.M. Tshursin, G. Vincze, George D.,

Juan Liao, JV Fernandes, K. Kitayama, Kamiya S, Kiselev D. A, Kousar, Y, Kulkarni Paresh P, Kulkarni, PP, Kumari S, L Pereira, M. A.

Khaleel, M. Jackson, M. Coelho, M.-G. Lee, M.P.F. Graça, Manoj K. Sing, Maranhao C, Marc Michel, Maria Alexandra Fonseca, Marie-

Hélène Metz-Boutigue, M. Borodachenkova, Markus J. Buehler, Martin-Gago, J, Mather G. C, Mendez, J, Mercedes Vila, Merino, P,

José Augusto Santos, Joana Mendes, João P. Correia, J.P. Almeida, Jackson, M.J., Jérôme Bour, JH Schmitt, Jin Jin Ha, JMC Rodrigues, J.

Suresh Kumar, J. Unsiobi, Polini, Ricardo, Portolés, M, Pratul K. Agarwal, PT Jones, Qi Hua Fan, R. Babu P, Chibante, F

R. Beja, R. McCann, R. Rai, R.W. Davies, RAF Valente, Rahul Krishna, Rai, R, Ramalho A, Ramírez-Santillán, C, Ranjbar, S, Reis P, Remond Yves,

Ricardo G Dias, RMN Jorge, RPR Cardoso, S Ping, S. M'Guil, S. Sharma, S.A. Ivlev, Saeed Tamimi, Safdari M, Said Ahzi, Sandra Cruz, Santos,

JA, Santos, S, SB Petersen, Sen Mei, Sena, J.I.V., Sergei V. Kalinin, Serro, A.P, Shangchao Lin, Silva Virgilia S, Nasar Ali, Nayak Manasa K.,

Nibennanoune, Zhor, Nina Balke, Nithin, Mathew,Nuno Almeida, Ogwu, AA, Okpalugo, TI, Olena Okhay, Ozturk F, PAF Martins, Paula A. A. P.

Marques, Paulo Davim, Paulo M.M. Vila Real, Pesetskaya E., Pinto, S, PK Tyagi, Michel M, Myoung-Gyu Lee, Nazanin Emami, Bobby G. Sumpter,

Boumbimba Rodrigue Matadi, Brandao A. D, Bernsmann Falk, LeDuc, P, Y. Kousar, Xin Xue, A. Boyd, Ghazavizadeh A, Campos HB, C. Rego,

Simões, F.J.P., Singh Sunil K., Smritikana Dutta, Soares M.J. Sonkar, VK Sousa, JM Stasiek M, Stephen Jesse, Svitlana Kopyl, T. Shokuhfar T,.B. Huang,

Tang, Chunjiu, Tatiana Zhiltsova, TB Huang, Teixeira, JM, Teodosiu C, Thomas Schubert, Toniazzo V, U. Krupp, Valente, MA, Valérie Toniazzo, Vallet-

Regí, M, Ventura, J, Victor Neto, Vincent Ball, Vincent Meunier, W. Milne, Waqar Ahmed, Wei Wen Willinger MG, Yang, Y.Y, A.G. Sviajin …

Co-authors of proof. Grácio

Centre for Mechanical Technology and Automation